Single-Molecule Magnet and Luminescence Properties of Lanthanide and Transition Metal Complexes Using Tetrazine and Naphthalimide Based Ligands

Kimia Jahandar Kojouri

Thesis Submitted to the faculty of Graduate and Postdoctoral Studies in partial fulfillment of the requirements for the Master of Science degree in Chemistry

Department of Chemistry and Biomolecular Sciences

Faculty of Science

University of Ottawa

Abstract

This thesis examined two distinct characteristics of lanthanide and transition metal complexes: Magnetism and Luminescence. In chapter two, synthesis, characterization, magnetic and luminescence investigations of mononuclear lanthanide complexes using Schiff-base tetrazine based ligand were performed. Six novel lanthanide complexes, $[La^{III}Cl_3(Htzpy)_2]$, $[Tb^{III}Cl_2(Htzpy)_2(MeOH)]Cl$, $[Ho^{III}Cl_2(Htzpy)_2(MeOH)]Cl$, $[Dy^{III}Cl_2(Htzpy)_2(MeOH)]Cl$, $[Er^{III}Cl_2(Htzpy)_2(MeOH)]Cl$ and $[Yb^{III}Cl_2(Htzpy)_2]Cl$ have been synthesized successfully and the studies were performed with the application of single crystal X-ray diffractometry, SQUID magnetometry, UV-Vis-NIR spectrometry and custom-built hyperspectral microscope (for luminescence spectroscopy). Chapter three is mainly about the luminescence properties of Co^{II} and Cu^{II} complexes using a naphthalimide based ligand. Two complexes, $[Co^{II}Cl_2(Pynap)_2]$ and $[Cu^{II}Br_2(Pynap)_2]$ were synthesized successfully and characterized using single crystal X-ray diffractometry, UV-Vis spectrometry and hyperspectral microscope (for luminescence spectroscopy). In order to have information about the electrochemical properties of Co^{II} and Cu^{II} complexes, their redox activity was monitored by cyclic voltammetry (CV) and compared with the parent ligand. In addition, a rational design to synthesize a new ligand (dipicnap) which consists of both naphthalimide and dipicolinic acid moieties is presented.

Acknowledgements

First and foremost, I would like to thank my supervisor Prof. Darrin Richeson for accepting me as one of his graduate students and giving me this opportunity to learn and gain skills in a peaceful environment, I could not have gotten through my master's degree without him. I would like to thank Prof. Eva Hemmer for performing luminescence measurement and giving me useful advice, Bulat Gabidullin for his crystallographic expertise, Gabriel Brunet for performing SQUID measurements, Yasmeen Hameed for her precious help in doing cyclic voltammetry and UV-Vis spectroscopy and thank all members of both Richeson and Murugesu groups for their support and the time they have spent to teach me numerous things from instrumentations to theoretical issues. The experience I have gained during these two years is priceless. Over the period of these two years I have made a lot of friends all around the chemistry department and I had the chance of having international friends and being familiarized with different cultures. Last but certainly not least, I would like to thank my family who always support me and motivate me to fight difficulties and resist against the storm of living alone in a foreign country.

Table of Contents

List of Tables

List of Figures

List of Schemes

List of Abbreviations

Ln…………………………….	Lanthanide
SMM………………………..	Single-molecule magnet
SIM…………………………..	Single-ion magnet
U_{eff}…………………………	Effective energy barrier
ϕ………………………………	Quantum yield
Q………………………………	Quantum yield
ε………………………………	Molar absorption coefficient
τ………………………………	Life time
τ_0…………………………	Pre-exponential factor
τ_{obs}……………………………	Observed life time
τ_r………………………………	Radiative life time
τ_{nr}…………………………	Non-radiative life time

χ_v	Volume magnetic susceptibility
χ_M	Molar magnetic susceptibility
χ_g	Mass magnetic susceptibility
M	Magnetization
H	Applied magnetic field
N	Avogadro number
g	Landé g factor
β	Bohr magneton
k	Boltzmann constant
T	Temparature
K	Kelvin
C	Curie constant
S	Spin ground state
L	Total orbital angular momentum quantum number
J	Total angular momentum
θ	Weis constant
m_j	Energy state for mixed spin and orbital angular momentum
D	Axial zero-field splitting parameter
E	Rhombic zero-field splitting parameter

QTM……………………………	Quantum tunnelling of magnetization
SQUID…………………………	Superconducting Quantum Interference Device
DC………………………………..	Direct current
AC………………………………..	Alternating current
χ'……………………………….	In-phase magnetic susceptibility
χ''……………………………….	Out-of-phase magnetic susceptibility
ν……………………………….	Frequency
T_B……………………………….	Blocking temperature
A……………………………….	Absorption
F…………………………………	Fluorescence
P…………………………………	Phosphorescence
IC……………………………….	Internal conversion
ISC………………………………	Intersystem crossing
η……………………………….	Sensitization efficiency
OLED……………………………	Organic light emitting diode
LMCT……………………………	Ligand to metal charge transfer
MLCT……………………………	Metal to ligand charge transfer
ILCT………………………………	Intra ligand charge transfer
MMLC…………………………..	Metal-metal to ligand charge transfer

LMMCT……………………………	Ligand to metal-metal charge transfer
MLLCT……………………………..	Metal to ligand-ligand charge transfer
IEDDA……………………………..	Inverse electron demand Dields Alder
FTIR…………………………………	Fourier transform infrared spectroscopy
ATR…………………………………..	Attenuated total reflectance
NMR…………………………………	Nuclear magnetic resonance
δ………………………………………	Chemical shift
XRD…………………………………..	X-ray diffraction
MeCN………………………………	Acetonitrile
MeOH………………………………	Methanol
EtOH…………………………………	Ethanol
DMF…………………………………	Dimethylformamide
TEA……………………………………	Triethylamine
DMSO……………………………….	Dimethylsulfoxide
DCM…………………………………	Dichloromethane
RT…………………………………….	Room temperature
br………………………………………	Broad
w………………………………………	Weak
m………………………………………	Medium

s	Strong
DPA	9,10 Diphenylanthracene
$\lambda_{excitation}$	Excitation wavelength
CV	Cyclic voltammetry
HOMO	Highest occupied molecular orbital
LUMO	Lowest occupied molecular orbital
TD-DFT	Time dependent density functional theory

Chapter 1: Introduction

Over the past few decades, lanthanide and transition metal complexes have attracted significant attention due to their potential applications in such varied applications as molecular magnetism, luminescence sensing, and catalysis.[1,2,3]In terms of magnetic properties, lanthanide complexes are famous candidates to show single molecule magnet behaviour according to their strong single-ion anisotropy and large magnetic moment.[4] Since the SMM behavior of $[Tb(Pc)_2]^-$ reported by Ishikawa, paramagnetic lanthanide ions, specifically Dy^{III} and Tb^{III} have become the most attractive candidates for constructing novel single molecule magnets. Significant research efforts are underway to increase the energy barriers (U_{eff}) of the SMMs with the goal of using these species in applications such as high-density information storage.[5] In terms of luminescence properties, Ln^{III} cations are attractive due to their narrow line-like emission in the visible to near IR region of the optical spectroscopic spectrum a feature arising from internal 4f-4f transitions. Furthermore, the high luminescence quantum yield and long phosphorescence life time of transition metal complexes allow the emission to be distinguished from a fluorescent background, and their large Stokes shift allows for easy determination of absorption and emission maxima. The emission from transition metal complexes displays sensitivity to their environment and their ability to tune their chemical and photophysical properties make them good candidates for luminescence sensing applications [6,2]. In order to more clearly provide a context for the thesis efforts and results, the principles of magnetism and luminescence as well as the relationship of lanthanide and transition metal ions with these two properties will be described.

1.1.1 Principle of magnetism:

The definitions and principles of magnetism have been studied extensively by John Hasbrouck Van Vleck and Olivier Kahn[7].The magnetic behavior of molecular species arises from its electronic structure, more specifically, electrons possess an intrinsic spin magnetic moment and their orbital motion can also contribute to magnetic features. In the broadest sense, there are two basic types of magnetism: paramagnetism and diamagnetism. Any atom or molecule which contains at least one unpaired electron is paramagnetic and it is attracted by the external magnetic field while diamagnetism is a property of all material that arises from interactions of paired electrons with the applied magnetic field. Diamagnetic materials are repelled from the external magnetic field. Paramagnetism and diamagnetism can also be described in terms of magnetic susceptibility (χ) which is the measure of the degree of magnetization of a material in response to an applied magnetic field. If the magnetic susceptibility is negative the substance is diamagnetic and if the magnetic susceptibility is positive the substance is paramagnetic. The relationship between magnetization and magnetic susceptibility can be described as:

$$\chi_{\mathrm{v}} = \frac{\mathrm{M}}{\mathrm{H}} \qquad \textit{Eq. 1.1}$$

Which χ_v is volume magnetic susceptibility, M is magnetization and H is the applied magnetic field. For convenience sometimes, mass or molar magnetic susceptibility are used rather than volume magnetic susceptibility (cm^3):

$$\chi_{\mathrm{g}} = \frac{\chi_{\mathrm{v}}}{\mathrm{density}(\rho)} \qquad \textit{Eq. 1.2} \qquad\qquad \chi_{\mathrm{M}} = \chi_{\mathrm{g}}(\mathrm{mol.wt}) \qquad \textit{Eq. 1.3}$$

1.1.2 Magnetic interactions:

Below a certain temperature, there are three general types of interactions within a paramagnetic material: ferromagnetism, antiferromagnetism and ferrimagnetism. These features arise from the nature of the interactions between the individual magnetic moments within the bulk material. The Magnetic moment or magnetic dipole moment of an object can be defined in terms of the torque that object experience in a given magnetic field. Ferromagnetic materials exhibit an alignment of individual magnetic moments induced by external magnetic field that remain aligned even after removal of the field. Antiferromagnetism occurs when the individual magnetic moments align in an antiparallel and equal magnitude and the sum of the magnetic moments is zero. Ferrimagnetism is similar to antiferromagnetism in that the individual magnetic moments align in an antiparallel fashion. However, in this case the individual magnetic moments have different magnitiudes and the antiparallel interactions leads to the formation of a residual net magnetic moment. As the temperature on the material is increased, the energy of the interaction between the individual magnetic moments can be overcome and the magnetic moments become free to randomly orient. The temperature at which ferromagnetic and ferrimagentic materials lose their energy of alignment is called the Curie temperature and the temperature at which antiferromagnetic materials lose their antiferromagnetic behavior is called Neél temperature.

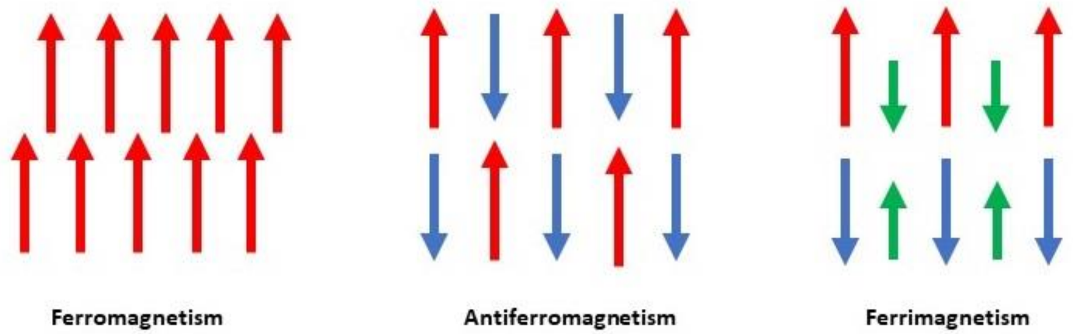

Figure 1.1. Three possible types of magnetic interactions.

1.1.3 Curie-Weiss law:

There is a relationship between magnetic susceptibility and temperature which is described using the Curie law:

$$\chi = \frac{Ng^2\beta^2}{3kT} S(S+1) = \frac{C}{T} \qquad \textit{Eq. 1.4}$$

The Curie law considers only the spin contribution of the electron to the magnetic susceptibility. In equation 1.4, χ is the molar magnetic susceptibility, N is Avogadro's number, g is the Landé g factor, β is the Bohr magneton, k is Boltzmann constant, T is the absolute temperature, S is the spin ground state of the magnetic species and C is the Curie constant. The Curie law treats the individual magnetic centers (i.e molecules) of the material as independent of each other. To have information about the magnetic interactions discussed in equation 1.4 parameter θ is introduced to the equation:

$$\chi = \frac{\mathrm{Ng^2\beta^2}}{\mathrm{3kT}}\ \mathrm{S(S+1)}\ \frac{1}{\mathrm{T}-\theta} = \frac{\mathrm{C}}{\mathrm{T}-\theta} \qquad \textit{Eq. 1.5}$$

When antiferromagnetic interaction is present, θ is negative and when ferromagnetic interactions exist, θ is positive.

As χ_M and M are macroscopic properties referring to the bulk sample, i.e. per mole of substance, for convenience, effective magnetic moment μ_{eff} which is a parameter that gives us a measure of S (total spin) per molecule is used:

$$\mu_{\mathrm{eff}} = \sqrt{\frac{3\mathrm{k}}{\mathrm{N}\mu_{\mathrm{B}}^2}}\ (\chi_{\mathrm{M}}\mathrm{T})^{1/2} = 2.828\,(\chi_{\mathrm{M}}\mathrm{T})^{1/2} = \sqrt{8\chi_{\mathrm{M}}\mathrm{T}} \qquad \textit{Eq. 1.6}$$

By substitution of equation 1.4 in eq 1.6:

$$\mu_{\mathrm{eff}}{}^2 = \mathrm{g}^2\ \mathrm{S(S+1)} \qquad \textit{Eq. 1.7}$$

If there is no orbital contribution, g = 2 (gyromagnetic ratio for a free electron):

$$\mu_{\mathrm{eff}} = 2\sqrt{\mathrm{S(S+1)}} \qquad \textit{Eq. 1.8}$$

And if there are spin and orbital contributions which exist effectively in heavy atoms such as lanthanides and second and third row transition metals:

$$\mu_{\mathrm{eff}} = [\mathrm{g^2S(S+1) + L(L+1)}]^{1/2} \qquad \textit{Eq. 1.9}$$

Where S = n/2 (n = number of unpaired electrons and L is $\sum m_l$, (m_l = orbital angular momentum).

In some cases with unpaired electrons, there are two or more states that the electrons can occupy that are the same energy. These states are termed ''degenerate''. The degeneracy of these states can be removed (lifted), thorough application of an external magnetic field and in cases of more than one electron, by the interaction between the electrons:

1.1.4 Zero-Field Splitting

This phenomenon originates from the interactions of unpaired electrons (spin-spin coupling) and mixing of ground and excited spin states via spin orbit coupling. Zero- field splitting happens in the systems with S ≥1 and in the presence of no external magnetic field which causes the splitting of the spin states. The corresponding Hamiltonian can be written as[8]:

$$\hat{H} = D\left\{\hat{S}_z^2 - \frac{1}{3}S(S+1)\right\} + E\,(\hat{S}_x^2 - \hat{S}_y^2) \qquad \textit{Eq. 1.10}$$

Where D is the axial and E is the rhombic zero-field splitting parameter. D is responsible for lifting the degeneracy of the 2S+1 micro states in the absence of applied field and it is particularly important in the case of single-molecule magnet. A positive D value indicates that the lowest $\pm M_S$ states are stabilized which inhibits the observation of an energy barrier and single-molecule magnet behaviour and when D is negative the highest $\pm M_S$ states are stabilized which gives a higher energy barrier and single-molecule magnet behaviour.

1.1.5 The Zeeman Effect

In the presence of magnetic field, the m_s states split. The m_s states that are aligned with the external magnetic field are lowered in energy and the m_s states aligned against the magnetic field gain higher energy by an equal proportion. The energy for each spin state can be described as:

$$E = -m_s g \beta H_0 \qquad \textit{Eq. 1.11}$$

Where E is the energy of the states, g is the landé g factor and beta is the Bohr magneton and H_0 is the applied magnetic field. The Zeeman diagram including Zero-field splitting with D < 0 and E > 0 for spin state S = 1 is depicted in figure 1.2.

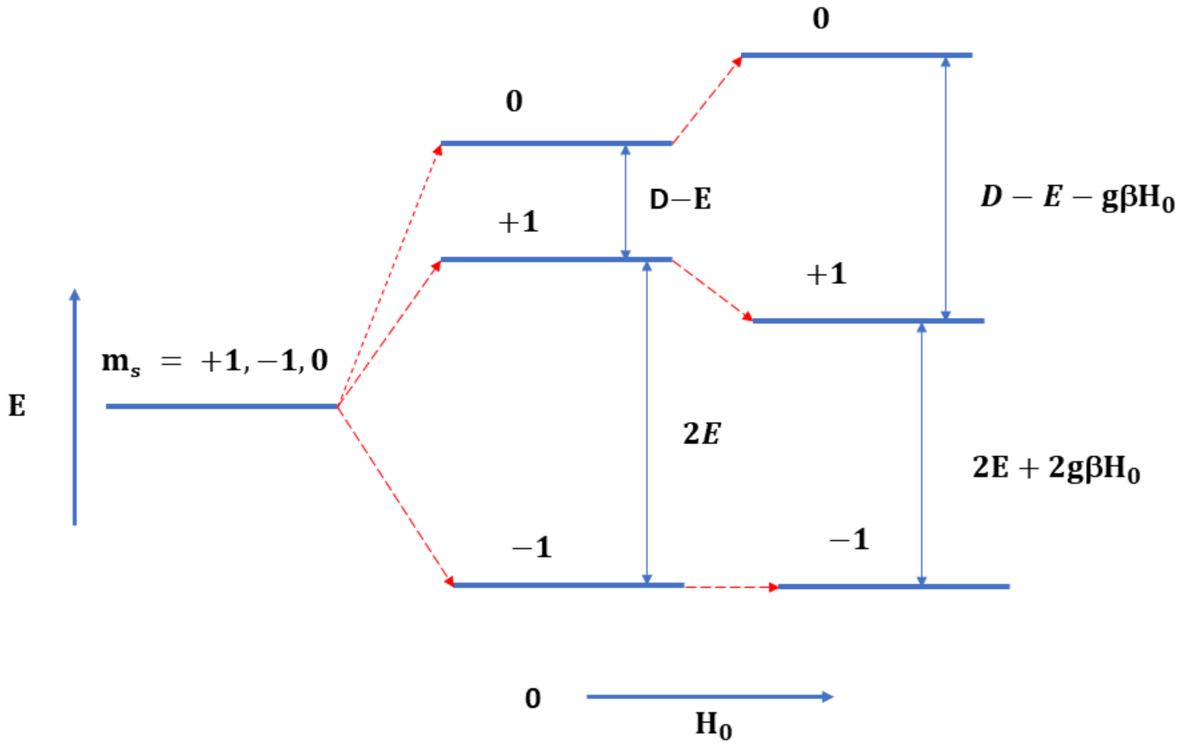

Figure 1.2. Zeeman diagram including Zero field splitting (ZFS) for S = 1, D < 0 and E > 0.

1.1.6 The Energy Barrier for Relaxation of Magnetization

When an external magnetic field is applied the $-M_S$ (aligned with the applied filed) and $+M_S$ (aligned against the applied field) states form. After removal of the external magnetic field, there are more spins in the more stable $-M_S$ state than in the $+M_S$ state and the spins need to reach equilibrium by equally populating these two states. Relaxation requires overcoming the energy barrier between two states. If the energy barrier is large enough the relaxation cannot happen, and the magnetization will remain. Therefore, the energy barriers will determine the retention of magnetization and are directly correlated to the magnetic blocking temperature. Below this temperature, the system behaves as a magnet and above this temperature it becomes paramagnetic.[9] The energy barrier can be described as[10]:

$$\mathrm{E} = |\mathrm{D}|\mathrm{S}^2 \text{ (integer spin system), } \mathrm{E} = \mathrm{D}(\mathrm{S}^2 - \frac{1}{4}) \text{ (half-integer system system)} \qquad \textit{Eq. 1.12}$$

Where D is the axial zero-field splitting (ZFS) parameter or axial anisotropy which is the preferential alignment of magnetic moment in a certain direction and S is the spin ground state. However, several single molecule magnets (SMMs) with hundreds of kelvin energy barriers show a blocking temperature less than 2 K. This incompatibility has been attributed to the quantum tunnelling of magnetization.

1.1.7 Quantum Tunnelling of the magnetization (QTM)

Quantum tunnelling of the magneitizaion has been a matter of active research for many years and it occurs between two levels that have same energy when mixing of electron spin wavefunctions occurs. During this phenomena spins ignore the energy barrier and flipping between spin states causes fast relaxation of magnetization. The transverse interactions which mix the states and let the spins flip can be due to the low symmetry component of the crystal field or the magnetic field produced by the nuclei or neighboring molecules. As the total spin quantum number S becomes bigger the possibility for mixing of two wavefunctions becomes lower. There are two different kinds of quantum tunnelling: direct quantum tunnelling and thermally assisted quantum tunnelling relaxation. The latter happens when spins reach thermally populated state and then pass through the barrier. Figure 1.3 indicates different kinds of quantum tunnelling as well as energy barrier for relaxation of magnetization. [11,12]

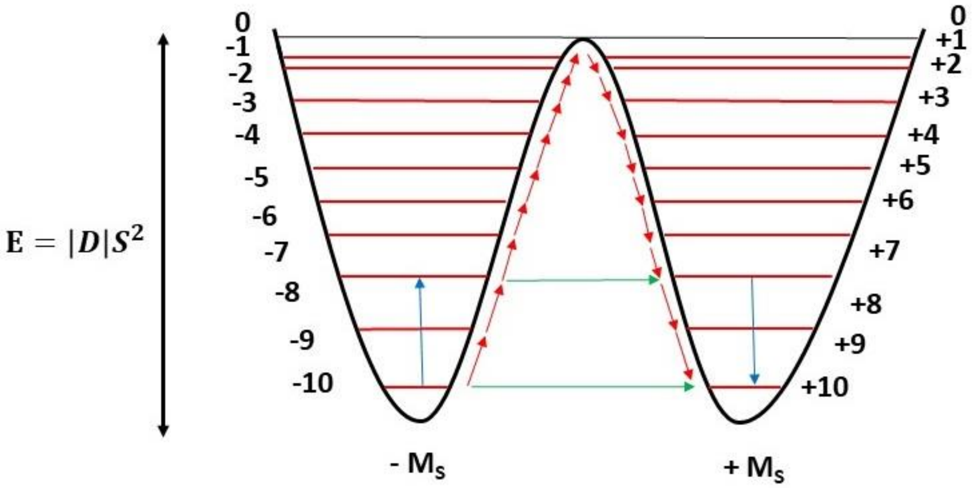

Figure 1.3. Double-well energy barrier diagram, red arrows: thermal relaxation, blue arrows: thermally assisted quantum tunnelling of magnetization, green: direct quantum tunnelling of magnetization.

1.1.8 Magnetic Measurements

The superconducting Quantum Interference Device (SQUID) is an instrument used to measure the magnetic properties of the materials. A SQUID is a very sensitive magnetometer used to measure changes in the magnetic field. This change in the magnetic field is observed by the change of current in the superconducting coil when a sample is passed through it. A SQUID magnetometer can measure magnetic susceptibility at various temperature from 1.8-500 K through either direct current (DC) or altering current (AC) methods. These currents produce static and oscillating magnetic fields in the coil, respectively. DC measurements provide information about magnetic saturation of the sample and the bulk susceptibility while AC measurements indicate the magnetization relaxation dynamics of the sample and give values for in-phase and out-phase magnetic susceptibility. One of the useful plots that can be accessed from DC measurements is χT *vs* T which removes the dependence of χ on T and gives us information about intermolecular or intramolecular interactions (ferromagnetic and antiferromagnetic) due to the deviation of the material from paramagnetism behavior. As shown in Figure 1.4 the decrease in χT with decreasing temperature is observed for antiferromagnetic behaviour and the increase in χT with decreasing temperature indicates ferromagnetic behaviour. The magnetization (M) *vs* applied field (H) as well as the magnetization (M) *vs* H/T (reduced magnetization) indicates the magnetic saturation and magnetic anisotropy respectively and can be obtained from DC measurements. The DC magnetic properties of 4 mononuclear lanthanide complexes (Tb^{III}, Dy^{III}, Ho^{III}, Er^{III}) will be discussed in the next chapter.

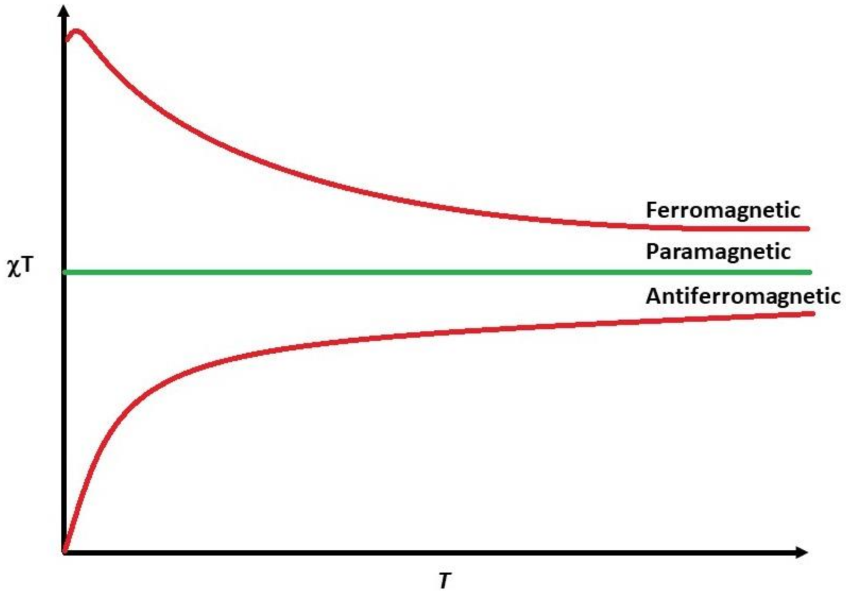

Figure 1.4. χT *vs.*T plot, indicating ferromagnetic and antiferromagnetic interactions.

In-phase (χ') and out-of-phase (χ'') magnetic susceptibilities can be derived from AC measurements which include alternating current or dynamic magnetic field and the frequencies can range from 0.1-1500 Hz for AC measurement in the presence or absence of applied static magnetic field. The in-phase magnetic susceptibility (χ') indicates the magnetic moments within the material which are aligned with the oscillating magnetic field and the frequency dependent out of phase magnetic susceptibility (χ'') is used to characterize the single molecule magnet behaviour of the sample. Additionally, the frequency dependent isotherm out-phase magnetic susceptibility can be used to measure the average relaxation time (the AC frequencies at which the out-of-phase magnetic susceptibility is maximum can be used to determine the relaxation time) and using the well-known Arrhenius type relationship, the effective energy barrier U_{eff} can be calculated by plotting τ vs $\exp(T^{-1})$.[10]

$$\tau = \tau_0 \exp(U_{eff}/kT) \qquad \textit{Eq. 1.13}$$

where τ is the relaxation time, U_{eff} is the effective energy barrier, k is Boltzmann's constant and T is temperature. In order to get a linear plot, $\ln\tau$ vs T^{-1} is usually plotted instead. Possessing a thermally linear behavior is the key factor to calculate the effective energy barrier. However, in many cases the Arrhenius plot is only linear across a limited temperature range and is usually temperature independent in lower temperatures. This non-linearity can be due to other types of relaxation mechanisms such as quantum tunnelling of the magnetization or Raman relaxation.

Another very useful piece of information that can be derived from AC measurements, is magnetic hysteresis. When the sample is magnetized due to the application of an external magnetic field, the magnetic field will reverse and if the sample retains its magnetization, a magnetic hysteresis loop forms. When the applied field goes back to zero the magnetization observed, is called remnant magnetization and the magnetic field required to make the magnetization zero is called the coercive field as shown in figure 1.5.

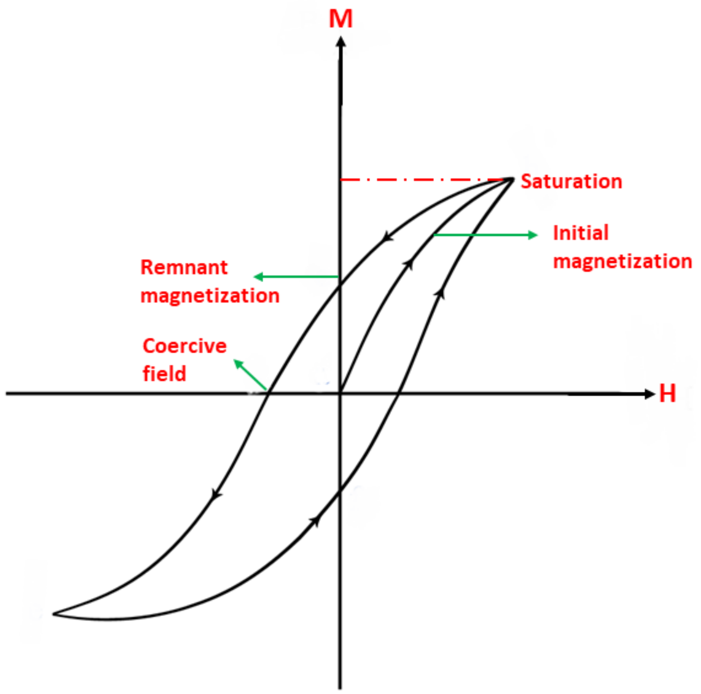

Figure 1.5. Schematic representation of magnetic hysteresis.

1.1.9 Single-Molecule Magnets and Lanthanides

Single-molecule magnets (SMMs) have attracted considerable attention during the last few years. A major reason for this originates from the concept of using SMMs for higher capacity data information recording which would allow data storage several orders of magnitude greater than at present. A traditional magnet contains a large number of magnetic domains and the data storage capacity depends on the size of these domains while single-molecule magnets enable access to the magnetism in molecular scale. Ritter reported that the maximum amount of information that can be stored in cobalt-based magnetic material within an area of 1 cm^2 is about three billion bits. This dimension would contain thousands of atoms and 30 trillion of SMM can fit in this area which means 10000 times greater data storage capacity.[11]

The first generation of SMMs were based on polymetallic clusters of transition metal complexes to obtain large spin states and high magnetic anisotropies. In 1993 the first single-molecule magnet $[Mn_{12}O_{12}(O_2CCH_3)_{16}(H_2O)_4]\cdot 4H_2O\cdot 2CH_3CO_2H$ was discovered which showed antiferromagnetic coupling of Mn^{III} and Mn^{IV} to each other. This antiferromagnetic interaction leads to the formation of large ground state spin (S = 10). An axial zero field splitting exists which causes the splitting of S = 10 states into 21 levels and when the external magnetic field is removed the Mn_{12} acetate cluster retained its magnetization. The energy barrier was determined to be 70 K *at 2 K.[12,13] A Number of efforts have been directed at increasing the energy barriers at higher blocking temperatures. However, there is a contradiction between having high spin states and high magnetic anisotropy. The increase of total spins, by adding metal ions, usually results in more symmetrical geometries, which generally do not give high magnetic anisotropies. More recently, the introduction of lanthanide complexes specifically (Tb^{III}, Dy^{III}, Ho^{III} and Er^{III}) to this area opens a new door by taking advantage of their intrinsic high spin states and large magnetic anisotropy achieved from strong spin-orbit coupling and crystal field (less than spin-orbit coupling but still effective) effects caused by ligand environment.

1.1.10 Electronic Properties of Lanthanides

Lanthanide ions behave very differently from transition metal complexes due to their 4f electrons which are shielded with 5s and 5p shells and make them relatively undisturbed from ligand field effects in comparison to transition metal complexes. As a result, the seven f orbitals are almost degenerate, and this degeneracy results in unquenched orbital angular momentum that leads to the formation of strong single-ion magnetic anisotropy for most lanthanides except La^{III}, Lu^{III}, Gd^{III} and Eu^{III}. Because of the large contribution of orbital angular momentum in lanthanides, the total spin angular momentum, S, is not as good a parameter to describe the magnetic properties of the lanthanides. In these cases, the total angular momentum, which is the sum of the total spin angular momentum and total orbital angular momentum is a better parameter. The total angular momentum can be derived as $J = |L - S|$ (in the case of orbitals that are less than half filled) and $J = |L + S|$ (in the case of orbitals that are more than half filled). For an ion with total angular momentum J, there is 2J+1 microstates.[14] The angular momentum parameters for trivalent lanthanides are summarized in table 1.1.

Table 1.1. Electronic configurations, Spin and orbital angular momentum, total angular momentum, ground state, g values and RT values for χT.

Lanthanide ion^{III}	**Electronic configuration**	**Spin angular momentum**	**Orbital angular momentum**	**Total angular momentum**	**Ground state symbol $^{2s+1}L_J$**	**g_J values**	**RT χT values**
La^{III}	[Xe]4f^0	0	0	0	$^1S_0$	-	-
Ce^{III}	[Xe]4f^1	1/2	3	5/2	$^2F_{5/2}$	6/7	0.8
Pr^{III}	[Xe]4f^2	1	5	4	$^3H_4$	4/5	1.6
Nd^{III}	[Xe]4f^3	3/2	6	9/2	$^4I_{9/2}$	8/11	1.64
Pm^{III}	[Xe]4f^4	2	6	4	$^5I_4$	3/5	0.9
Sm^{III}	[Xe]4f^5	5/2	5	5/2	$^6H_{5/2}$	2/7	0.09
Eu^{III}	[Xe]4f^6	3	3	0	$^7F_0$	5	-
Gd^{III}	[Xe]4f^7	7/2	0	7/2	$^8S_{7/2}$	2	7.88
Tb^{III}	[Xe]4f^8	3	3	6	$^7F_6$	3/2	11.82
Dy^{III}	[Xe]4f^9	5/2	5	15/2	$^6H_{15/2}$	4/3	14.17
Ho^{III}	[Xe]4f^{10}	2	6	8	$^5I_8$	5/4	14.07
Er^{III}	[Xe]4f^{11}	3/2	6	15/2	$^4I_{15/2}$	6/5	11.48
Tm^{III}	[Xe]4f^{12}	1	5	6	$^3H_6$	7/6	7.15
Yb^{III}	[Xe]4f^{13}	½	3	7/2	$^2F_{7/2}$	8/7	2.57
Lu^{III}	[Xe]4f^{14}	0	0	0	$^1S_{10}$	-	-

1.1.11 Lanthanide Contraction

Another special characteristic of the lanthanide series is their large radii contraction across the period. This is the result of the poor shielding of nuclear charge by the 4f electrons. Across the lanthanide series the ionic radii of the lanthanides decrease smoothly from 103 pm (La^{III}) to 86 pm (Lu^{III}) as shown in figure 1.6. Based on the lowest energy principle as the atomic number increases the electrons distribute in the inner shells (4f) and not in outer-shells. Therefore, the increased nuclear charge which is not shielded from the added electrons attracts the outer-shell electrons effectively and causes the lower ionic radii and lanthanide contraction. In the next chapter a series of mononuclear lanthanide complexes will be presented where this contraction is observed.

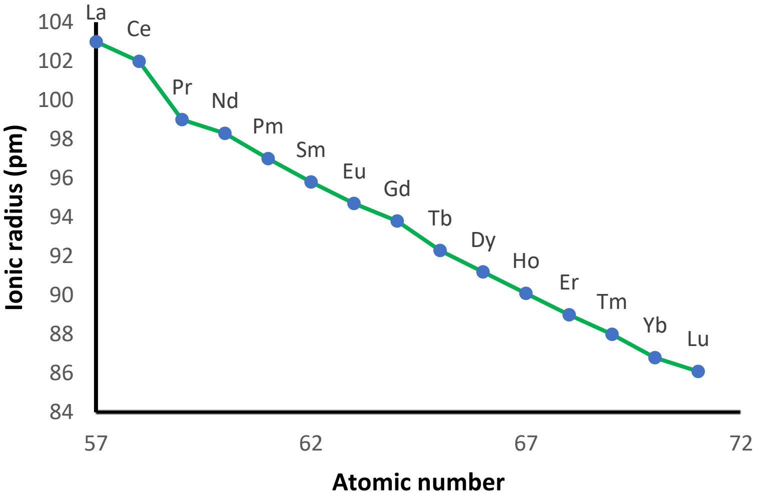

Figure 1.6. The relationship between the ionic radius and atomic number of lanthanide series (6-coordinate), indication of lanthanide contraction.

1.1.12 Mono-nuclear Lanthanide Single-Molecule Magnet Complexes

In 2003, Ishikawa et. al, reported a new class of lanthanide complexes, $[Pc_2Tb]^-.TBA^+$ and $[Pc_2Dy]^-.TBA^+$ ($TBA^+ = N(C_4H_9)_4^+$ and Pc = phthalocyanine) exhibiting single-molecule magnet behaviour by a mechanism different from the category of transition-metal-cluster SMMs. These two eight coordinates complexes with D_{4d} symmetry for which the $[Pc_2Tb]^-.TBA^+$ crystal structure is represented in figure 1.7, produced magnetization relaxation with blocking temperatures higher than previously reported transition metal complexes. The peak position for out-of-phase magnetic susceptibility (χ'') *vs* T shows single-molecule magnet behaviour at 40 K and 10 K for $[Pc_2Tb]^-.TBA^+$ and $[Pc_2Dy]^-.TBA^+$ respectively using a 1 kHz frequency and the calculated energy barrier was 331 K and 40 K respectively.5 Later magnetic hysteresis measurements in the sub-kelvin temperature range revealed that quantum tunnelling of magnetization is present (the stair-case like structure of the hysteresis loop supports the occurrence of the quantum tunnelling of the magnetization (QTM)) which originates from the interactions between the unpaired electrons and the spin of the lanthanide nucleus (hyperfine interactions).[15] Subsequent to this report, several examples of mono-nuclear lanthanide complexes with a variety of ligand types and different coordination geometries have been synthesized which display single-molecule magnet behavior. For instance, a number of single-molecule magnets were synthesized using a plethora of organic ligand such as 1,4,7,10-tetraazacyclododecane-N, N′, N″, N‴-tetraacetate, organo metallic sandwich ligands or phtalocyanine. In all these systems, coordinated ligands derive the desired axial magnetic anisotropy due to an adequate charge distribution around the lanthanide ion.[16] Based on these results, a general rationale for designing high performance single-molecule magnets is to have large J values to get high M_J ground state. This suggests that the focus should be on the second half of the lanthanide series., and on coordination environments with high order symmetry because these conditions would lead to the M_J wave functions that do not mix well with each other (i.e limit the quantum tunnelling phenomena).[17] With this strategy in mind, complexes of Tb^{III}, Dy^{III}, Ho^{III,} and Er^{III} with novel Schiff-base tetrazine based ligand have been synthesized and their magnetic behaviour has been characterized in order to get higher energy barriers at higher blocking temperatures.

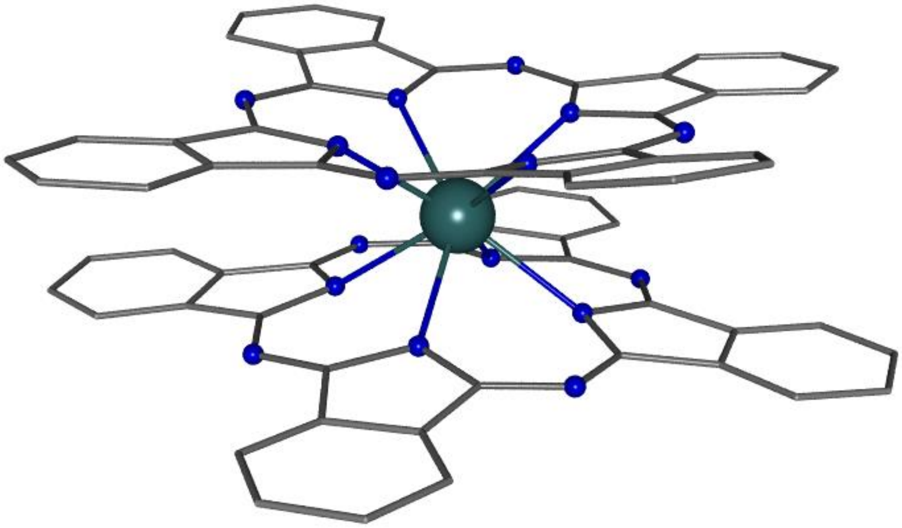

Figure 1.7. $[Pc_2Tb]^-$ complex as the first lanthanide-containing single-molecule magnet (Ref. 5). Color code: light blue: Tb, dark blue Nitrogen. All unfilled vertices are carbon atoms. Hydrogen atoms are not

1.2.1 Principles of Luminescence

The principles of luminescence that are described below were extracted from a text by Lakowicz.[18] A molecule after electronic excitation to a higher state of energy, returns to the ground state via both radiative and non-radiative pathways. The radiative pathway is called luminescence. Fluorescence and phosphorescence are two categories of luminescence dependant on the nature of the excited states. For example, when molecules relax from the zero-vibrational level of the first excited singlet state (S_1) to the ground state (S_0), the luminescence is called fluorescence. When the transition occurs from the excited triplet state (T_1) to the S_0 ground state, this emission is known as phosphorescence. Fluorescence is spin-allowed since the spin of the electron in the excited singlet state is paired with the electron in the ground state orbital and is a rapid radiative relaxation process that occurs about 10^{-8} s. In contrast, phosphorescence is a spin-forbidden ($T_1 \rightarrow S_0$) and results in a delayed radiative decay process that occur in about 10^{-3} s. Phosphorescence is more common at low temperatures.

1.2.2 Jablonski Diagram

The process that occurs between the absorption and emission of light is usually represented by a Jablonski diagram. Jablonski diagrams are used as the starting point for discussing light absorption and emission. These diagrams are named after Professor Alexander Jablonski who is known as the father of fluorescence spectroscopy. A typical Jablonski diagram is depicted in Figure 1.8. The singlet ground, and the first and second singlet excited and triplet excited states are indicated by S_0, S_1, S_2 and T_1 respectively. Each of these electronic energy levels contains vibrational sub-levels which are depicted by 0, 1, 2, etc…. According to the Frank-Codon principle, electronic transitions occur in about in about 10^{-15} s which is too short for significant displacement of nuclei. Irradiation of a compound can result in excitation to some higher vibrational level of either S_1 or S_2. With a short time line of about 10^{-12}s, the excited electrons will relax to the lowest vibrational level of S_1 in a process called internal conversion. While fluorescence emission generally happens from a thermally equilibrated excited state, which is the lowest energy vibrational state of S_1, relaxation to the ground state usually occurs to a higher excited vibrational ground state and then quickly reaches thermal equilibrium. Molecules in the S_1 excited state may undergo spin conversion called intersystem crossing to the first triplet state T_1. Once in the T_1 state, these compounds can relax to the S_0 ground state through phosphorescence. Molecules with a heavy atom such as bromine and iodine facilitate intersystem crossing and enhance phosphorescence quantum yield. Spin-orbit coupling is one of the important reasons for inter-system crossing and that is why metal complexes often display phosphorescence emission rather than fluorescence.

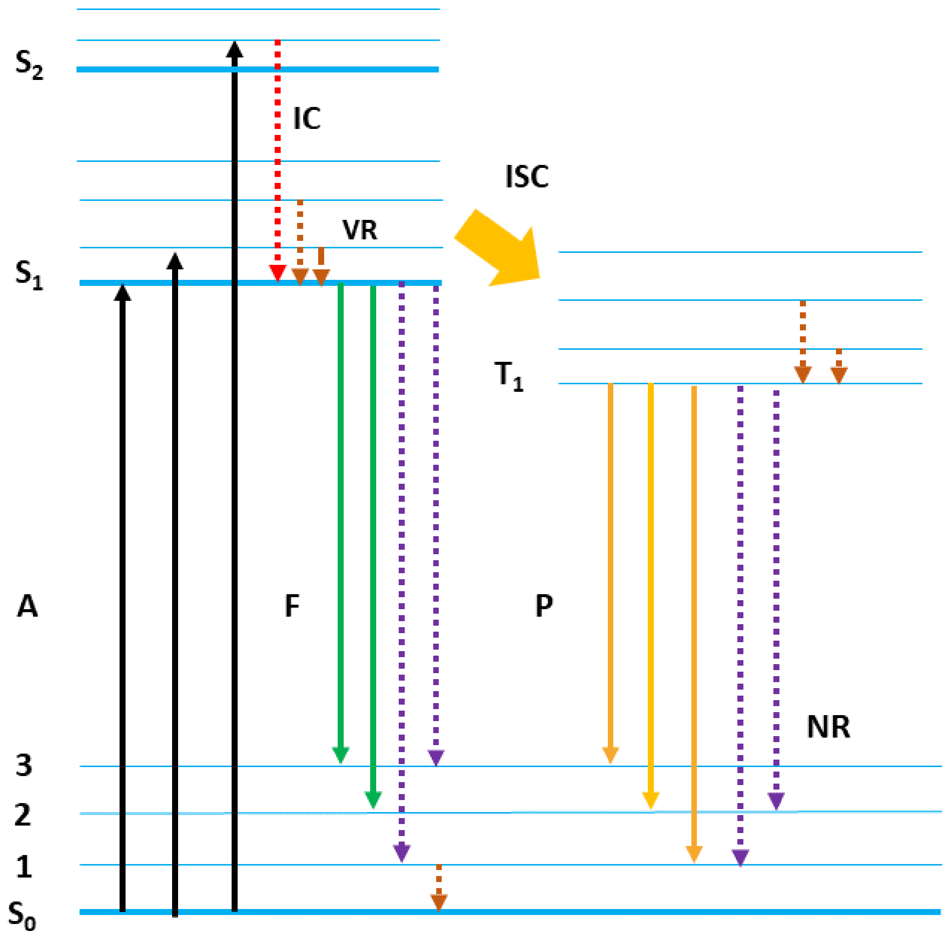

Figure 1.8. Schematic representation of Jablonski diagram. A: Absorption, F: Fluorescence, P: Phosphorescence, IC: Internal conversion, ISC: Inter system Crossing, VR: Vibrational relaxation, NR: Non-radiative relaxation

1.2.3 The Stokes Shift

Studying the Jablonski diagram indicates that most of the time emission energy is less than the absorption energy. Energy losses between excitation and emission are usually observed in the luminophores in solutions and one possible reason could be the rapid relaxation to the lowest vibrational level of S_1. In addition, luminophores usually relax to the higher vibration of S_0 states, causing thermal relaxation to the lower states. Excited state reactions, complex formation and interactions with solvent are other possible reasons.

1.2.4 Luminescence Quantum Yield and Lifetime

Luminescence quantum yield is the number of emitted photons relative to the number of absorbed photons and lifetime determines the time available for the compound to interact with its environment. The luminescence quantum yield can be described as:

$$Q = \frac{\Gamma}{\Gamma + K_{nr}} \qquad \textit{Eq. 1.14}$$

In which Γ is the radiative rate and K_{nr} is the rate of non-radiative decay. The lifetime is defined as the average time that the molecule spends in the excited state before relaxation to the ground state and can be described as:

$$t = \frac{1}{\Gamma + K_{nr}} \qquad \textit{Eq. 1.15}$$

The radiative decay rate Γcan be derived as:

$$\Gamma \cong 2.88 \times 10^{9} \mathrm{n}^{2} \frac{\int \mathrm{f}(\overline{\mathrm{v}})\mathrm{d}\overline{\mathrm{v}}}{\int \frac{\mathrm{f}(\overline{\mathrm{v}})\mathrm{d}\overline{\mathrm{v}}}{\overline{\mathrm{v}}^{3}}} \int \frac{\varepsilon(\overline{\mathrm{v}})}{\overline{\mathrm{v}}} \mathrm{dv} = 2.88 \times 10^{9} \mathrm{n}^{2} < \overline{\mathrm{v}}^{-3} >^{-1} \int \frac{\varepsilon(\overline{\mathrm{v}})\mathrm{dv}}{\overline{\mathrm{v}}}$$

$$\textit{Eq. 1.16}$$

Where f(ν) is the emission spectrum plotted on the wavenumber scale (cm^{-1}), ε(ν) is the absorption spectrum and n is the refractive index of the medium. Although this equation works well for several compounds, there are some defects to it: it does not account for solvent interactions, does not consider the change in the refractive index between the absorption and emission wavelength and does not consider changes in the excited state geometry. The complete form of the equation includes $G = g_l/g_u$ where g_l and g_u are the degeneracies of the lower and upper states respectively. For fluorescence transitions G = 1 and for phosphorescence transitions G = 1/3. K_{nr} which corresponds to non-radiative decay is approximately 10^{9} s^{-1}. As mentioned the overall quantum yield can be experimentally measured;

however, achieving a reliable value is not easy. The measurement of absolute quantum yield is critical and requires special equipment because it is important to know both the amount of light received by the sample and the amount of light emitted from the sample. Proper measurements require the use of scattering agents and an integrating sphere to calibrate the system. One of the most common methods for routine work is to determine the relative quantum yield. In this case, the quantum yield of the unknown is compared with a reference sample[19]:

$$\mathrm{Q_X} = \left(\frac{\mathrm{A_R}}{\mathrm{A_X}}\right)\left(\frac{\mathrm{E_X}}{\mathrm{E_R}}\right)\left(\frac{\eta_\mathrm{X}}{\eta_\mathrm{R}}\right)^2 \mathrm{Q_R} \qquad \textit{Eq. 1.17}$$

Where Q is the luminescence quantum yield, A is the absorbance at the excitation wavenumber, E is the area under the corrected emission curve, and η is the refractive index of the solvent. The subscripts R and X refers to the reference and unknown sample.

There is an alternative and more accurate method which is an extended form of the previous method. This approach is based on the slope of the graph of integrated emission intensities *vs* absorbance intensities with different concentrations of both samples and references separately. The plots give a linear behaviour with a specific slope:

$$\mathrm{Q_X} = \mathrm{Q_R}\left(\frac{\mathrm{Grad_X}}{\mathrm{Grad_R}}\right)\left(\frac{\eta_\mathrm{X}}{\eta_\mathrm{R}}\right)^2 \qquad \textit{Eq. 1.18}$$

Where Q is the quantum yield, the subscripts R and X indicate reference and sample respectively, Grad is the gradient from the plot of the integrated fluorescence intensity vs absorbance and η is the refractive index of the solvent.

However, several factors should be taken into consideration:

1. Concentration range: In order to minimize the reabsorption effect, absorbance should not exceed 0.1 at the excitation wavelength.

2. Sample preparation: It is important that all the glassware is kept very clean and all the solvents should be spectroscopic grade and checked for background fluorescence.
3. Cuvettes: Standard 10 mm path length fluorescence cuvettes are sufficient for fluorescence measurements.
4. Standard sample: The standard sample should be chosen to ensure that it absorbs at the excitation wavelength of the sample and emits at region that the sample has emission.[20,21,22]

1.2.5 Luminescence Quenching

The decrease in intensity of the emission is called luminescence quenching and can occur due to different mechanisms. Collisional quenching happens when the excited state of the luminophores returns to its ground state upon contact with the quencher (some other molecules in the environment). There are a number of potential quencher molecules such as oxygen, halogen, amine and electron deficient molecules. Another possible mechanism is that the luminophores can form non-luminescent complexes with quenchers, this process is called static quenching. A third possibility is the attenuation of the incident light by the luminophores or other molecules in the solution. The limitations caused by quenching factors are a key reason for the usage of metal luminescence complexes rather than organic molecules. As d orbitals for transition metal complexes and f orbitals for lanthanide complexes are more shielded from their environment, they are less affected by external factors such as solvent molecules or other molecules present in the solution.

1.2.6 Luminescent Metal Complexes

Over the past few decades luminescent metal complexes have attracted significant attention due to their applications in photochemistry, organic optoelectronics and luminescent sensors. These luminescent metal complexes contain both transition and lanthanide metal complexes. Here, each of these categories will be discussed.[2,6]

1.2.7 Lanthanide Luminescence

Several lanthanide ions exhibit visible to near-IR emission upon excitation by ultraviolet light. The color of their emission depends on the lanthanide ions; for example Eu^{+3}, Tb^{+3}, Sm^{+3} and Tm^{+3} emit red, green, orange and blue respectively. In addition, Yb^{+3}, Nd^{+3} and Er^{+3} are best known for their near-IR emission. Since electrons in the 4f orbitals are shielded by the electrons in the $5s^2$ and $5p^6$ shells, there is a minimal ability of ligands and external molecules to affect the electronic configuration of trivalent lanthanide ions. This leads to the observation of narrow line-like-emission from the lanthanide ions and higher life-time of the excited states. However, although the photoluminescence of lanthanides is an efficient process, due to the Laporte law, f-f transitions are forbidden and the molar absorption coefficient of lanthanide ions (ε) is significantly low (< 10 L mol^{-1} cm^{-1}) which means only a limited amount of UV irradiation will be absorbed by the trivalent lanthanide ions. Therefore, in order to have emission from f orbitals, there should be an alternative solution instead of direct absorption.

1.2.8 Antenna Effect or Sensitization

In 1942 Weissman observed that a very strong metal-centered luminescence could be observed in lanthanide complexes with organic ligands. Some portion of the energy absorbed by the organic receptor (chromophore) was transferred to lanthanide excited states and a sharp emission band was detected after internal conversion to the emitting level of the lanthanide ion. This phenomenon is called sensitization of the metal-center or referred to as the antenna effect.[23,24] The commonly accepted energy mechanism for the energy transfer from chromophore to the lanthanide ion was proposed by Crosby and Wan.[25,26] Upon excitation of the organic molecule to S_1 via ultraviolet radiation, the molecules undergo fast internal conversion to lower vibrational levels of S_1 through interaction with solvents for example. The excited singlet state may be deactivated radiatively to the ground state (fluorescence) or may undergo non-radiative intersystem crossing from singlet to triplet state and then deactivated radiatively from T_1 (phosphorescence). Alternatively, the complex can undergo a non-radiative transition from the lowest level of T_1 to a lower 4f state followed by characteristic line-like photoluminescence or can be deactivated by non-radiative processes which are mostly caused by vibrionic coupling with the ligand and solvent molecules.

Luminescence of the lanthanide ions will occur only from determined energy levels which are termed resonance levels. For example, the main resonance levels are $^4G_{5/2}$ for Sm^{+3} (17800 cm^{-1}), $^5D_0$ for Eu^{+3} (17250 cm^{-1}),$^5D_4$ for Tb^{3+} (20430 cm^{-1}) and $^4F_{9/2}$ for Dy^{+3} (20960 cm^{-1}). Importantly in order to populate a resonance level of a lanthanide ion, the lowest triplet state of the ligand must be located at an energy equal to or above the resonance level of the lanthanide ion. This ligand energy level cannot be below the lanthanide resonance level. Since the position of the triplet level of the ligand depends on the ligand, ligand design should be considered in order to achieve high luminescence intensity.[27] The location of the triplet state is also temperature dependent and therefore, the luminescence caused by the excitation of the organic chromophore is more sensitive to the temperature than luminescence caused by excitation of 4f levels individually. Another way to sensitize lanthanide luminescence is via charge-transfer states and this usually occurs in trivalent lanthanides which can be reduced to the divalent state. Light can be absorbed by ligand-to-metal charge transfer (LMCT) state from which the excitation energy can be transferred to the 4f levels of lanthanides. This process can happen only if the LMCT energy state is high enough.[28] Not to mention that, sometimes, sensitization can be done via absorbing chromophores which contain d-block metals.[29,30]

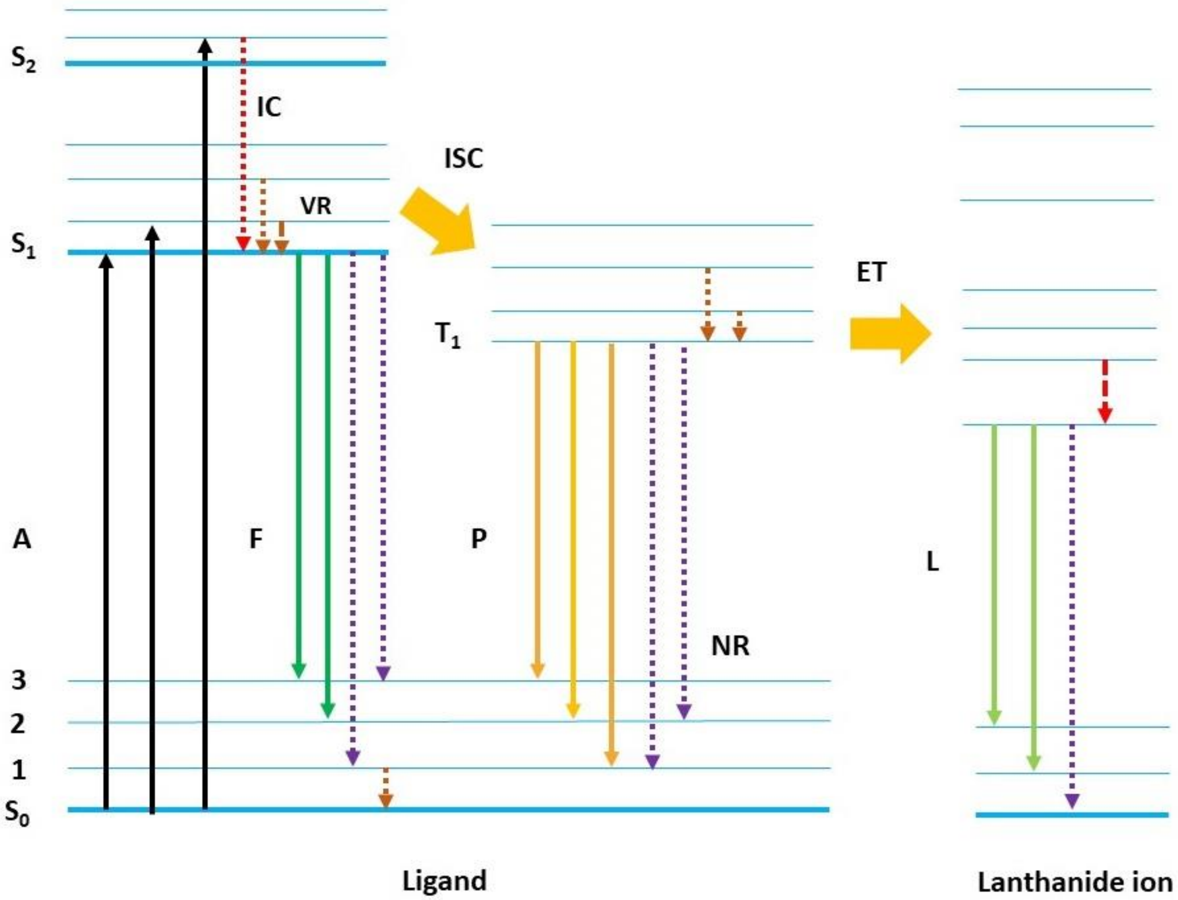

Figure 1.9. Schematic representation of photophysical process in Ln^{III} ions (sensitization). A: Absorption, F: Fluorescence, P: Phosphorescence, L: Luminescence, IC: Internal Conversion, ISC: Intersystem Crossing, ET: Energy Transfer, VR: Vibrational relaxation, NR: Non-radiative relaxation

1.2.9 Lanthanide Luminescence Quantum Yield

As mentioned above, the luminescence quantum yield is defined as the ratio of the number of emitted photons to the number of absorbed photons. For luminescent lanthanide complexes, the total luminescence quantum yield ϕ_{tot} upon excitation of the ligand is determined by the efficiency of sensitization of energy transfer η_{sens} and by the quantum yield of the lanthanide luminescence ϕ_{Ln}.

$$\Phi_{\mathrm{tot}} = \eta_{\mathrm{sens}} \Phi_{\mathrm{Ln}} \qquad \textit{Eq. 1.19}$$

Where ϕ_{Ln} is intrinsic luminescence quantum yield and refers to the direct excitation in 4f levels of the Ln^{+3}. The intrinsic quantum yield is directly related to the rate constants for radiative Γ and non-radiative k_{nr} deactivation which is described in Eq 1.12. ϕ_{Ln} indicates how well the radiative process competes with non-radiative processes., Non-radiative processes include energy back transfer to the ligand, energy transfer quenching and matrix vibrations, specially OH and NH vibrations. Non-radiative processes affect the observed luminescence life-time ($\tau_{obs} = \tau_r + \tau_{nr})^{-1}$, therefore if the radiative life-time is known ϕ_{Ln} can be calculated using the observed luminescence life-time:

$$\Phi = \tau_{\mathrm{obs}/\tau_{\mathrm{r}}} \qquad \textit{Eq. 1.20}$$

The observed life-time can be derived from intensity decay curves, however, the radiative life-time is not easy to obtain experimentally and many scientists assume a constant value for a given lanthanide ion which is incorrect.[31] The best way to calculate the radiative life-time is the application of Jud-Oflet intensity parameters. These parameters can be derived from optical absorption spectra of the lanthanide complex. [32]

1.2.10 Transition Metal Complex Luminescence

In contrast to organic luminophores which are mostly singlet emitters, transition metal complexes, in keeping with their strong spin-orbit coupling, are triplet emitters and they are famous for their phosphorescence properties which are widely used for making organic light emitting diodes (OLEDs) for display and lighting applications.[33] In addition, due to their high luminescence quantum yield, long phosphorescence lifetime, large Stokes shift, sensitivity of the emission to the change of environment and the ability to tune their chemical and photophysical properties, transition metal complexes are an appropriate choice for chemosensing and biosensing.[2] The excited states of transition metal complexes are more complicated than organic luminophores and can include various types of transitions such as ligand to metal charge transfer (LMCT), metal to ligand charge transfer (MLCT), intra ligand charge transfer (ILCT), metal-metal to ligand charge transfer (MMLCT), ligand to metal-metal charge transfer (LMMCT) and metal to ligand-ligand charge transfer (MLLCT).[34] The identity of the metal, the ligand and local environment determine the nature of the excited states. The application of luminescent transition metal complexes for chemosensing has been recently described by Li et. al., Chemosensors have at least two different units: a receptor unit and a signaling unit. The receptor unit selectively binds to the analyte and the signaling units which are the transition metal complexes such as Cu(I) and Cu(II) complexes, report the interactions between receptors and analyte through the change in their optical activities.[35]

In chapter 3, the synthesis and characterization of Cu(II) and Co(II) complexes as well as the rationalization for the ligand choice are reported.

Chapter 2: Magnetic and Luminescent Properties of a Series of Lanthanide Complexes with tetrazine-based Shiff-base ligands.

2.1 Schiff-Base Ligands

Schiff-base ligands are synthesized from the condensation of an amine with a compound containing a carbonyl group and they have a variety of applications in chemical industry such as catalytic activity in several reactions like polymerization, reduction of thionyl chloride, oxidation of organic compounds, reduction of ketones, aldol reactions. Also, Schiff-base ligands have applications in biology including antimicrobial, antifungal, anticancer and anti-oxidant activities. A Schiff-base which is also known as imine or azomethine is a nitrogen form of an aldehyde or ketone in which the carbonyl group is replaced by an imine or azomethine group. One of the most important reasons for broad application of Schiff-base ligands refers to the ease of their synthesis and their complexation with most transition and lanthanide metal ions. A general route for synthesis of Schiff-base ligand is shown in Scheme 2.1. The synthesis proceeds through a nucleophilic attack from primary amine to carbonyl group, formation of carbinolamine, protonation of OH moiety, loss of one water molecule and deprotonation of resulting iminium cation by base. By substitution of different groups in R_2 position of the primary amine, the desired structure can be achieved.[36,37]

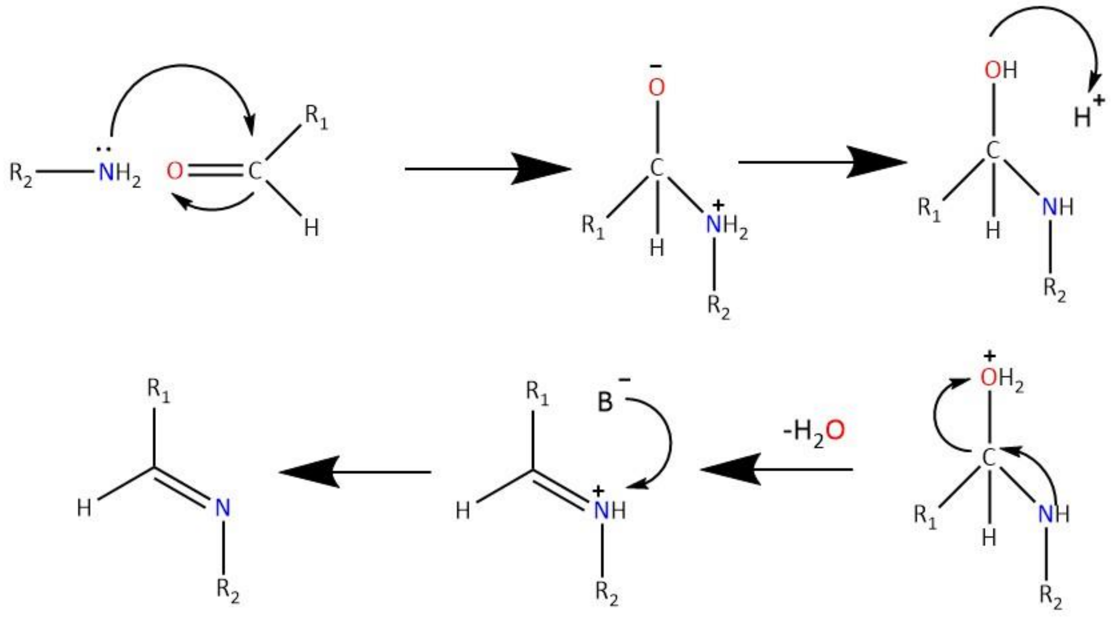

Scheme 2.1. General mechanism for Schiff-base formation.

2.2 Tetrazine-Based Schiff-Base ligand

Tetrazine, specifically 1,2,4,5 tetrazines have attracted significant attention in coordination chemistry because of their ability to bind to multiple metals as a result of possessing four N-donor (σ-donor, π-acceptor) moieties within their structures. The four nitrogen atoms have low-lying π^*orbitals which make them an appropriate π acceptor component with low one electron reduction potential (E > -1.3 V *vs.* ferrocene) to make radical anions. One electron redox process of a tetrazine ring is shown in scheme 2.2. This allows for the increase in total spin of the system and promotes strong magnetic exchange interactions.[38,39] Recently, the Dunbar group indicated that the existence of the tetrazine moiety within the Co^{II} complex increases the magnetic properties with large exchange coupling constant between a Co^{II} ion and the anion radical of a tetrazine, indicating that tetrazine can be used to promote strong magnetic exchange interactions.[40] Not to mention that tetrazine radicals have high degree of stability. Additionally, tetrazines are used in an inverse electron demand Diels- Alder (IEDDA) reaction which is playing a pivotal role in click chemistry.[41] In addition, they have unique emission properties that are highly dependent on the substitution pattern of the compound.[42] Tetrazines are also considered as an efficient receptor with several anions in anion-pi system reactions.[43] The parent tetrazine has rarely been used in coordination chemistry due to the difficulties during the synthesis and handling and usually 3,6 disubstituted or 3 monosubstituted forms of tetrazine, are used.39 These substituents can give some additional properties to the tetrazine such as enhancing the emission properties. Regarding these unique properties, tetrazines provide scientists with the ability to synthesize different forms of tetrazine-based ligands for various applications such as energetic materials[44], single-molecule magnets (SMMs), luminescence and recently photocatalytic activity[45].

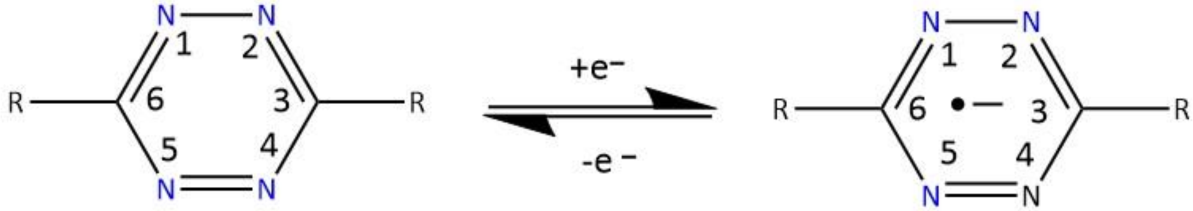

Scheme 2.2. One electron redox process of tetrazine.

In order to incorporate tetrazine ring into a new ligand structure, the Schiff-base motif was used. Therefore, combining the high magnetic anisotropy of lanthanide ions, the properties of tetrazine and application of Schiff-base reactions into consideration, the rational design for the ligand synthesis was targeted for this thesis. Figure 2.1 indicates the ligand structure which was used in this study. The ligand (2-pyridinylmethylidene)-3-hydrazinyl-1,2,4,5-tetrazine (Htzpy) is constituted of three moieties, the pyridine ring, the hydrazone linker and a tetrazine ring. Together these groups may form a tridendate coordination pocket with three N atoms, one from the pyridyl group, one from the hydrazone linker and the third one form the tetrazine ring.

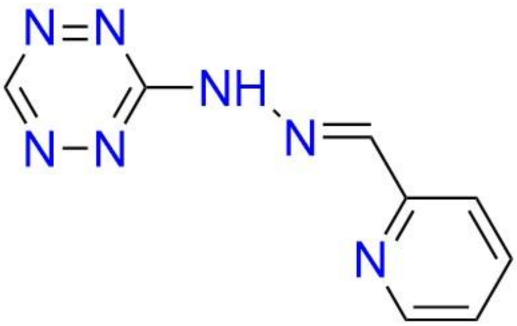

Figure 2.1. Chemical structure of (2-pyridinylmethylidene)-3-hydrazinyl-1,2,4,5-tetrazine (Htzpy).

In this chapter of the thesis, the synthesis and characterizations including X-ray crystallography, magnetic measurements and luminescence measurement for mononuclear lanthanide complexes with the ligand are presented and discussed.

2.3 Experimental

2.3.1 Chemicals:

All manipulations were performed under aerobic conditions. All chemicals were used as received from Acros, Strem chemicals and Sigma-Aldrich without further purification.

2.3.2 Instrumentations:

IR Spectroscopy

Infrared data were collected in solid state on a Varian 640 FT-IR spectrometer equipped with an ATR in the 600-4000 cm^{-1} range.

NMR Measurements

NMR data were collected using a Bruker Avance 400 spectrometer equipped with an automated sample holder and 5 mm autotuning broadband probe with Z gradient.

Elemental Analysis

Elemental analysis was performed using an Isotope Cube elemental analyser by G.G Hatch Stable Isotope Laboratory, University of Ottawa.

X-Ray Crystallography

Single crystals suitable for X-ray diffraction measurements were mounted on the glass fibre using paraffin oil. Unit cell measurement and intensity data collections were done on a Bruker AXS smart single crystal diffractometer equipped with a sealed Mo tube source (λ = 0.71073 Å) APEX II CCD detector. The data collection included a correction for Lorentz and polarization effect, with an applied multi scan absorption corrections (SADABS). The crystal structures were solved and refined using the SHELXTL program suite. Direct methods yielded all non-hydrogen atoms which were refined with anisotropic thermal parameters. All hydrogen atoms positions were calculated geometrically and were riding on their respective atoms.

Magnetic Measurements

The magnetic susceptibility measurements were obtained using SQUID magnetometer MPMS-XL7 operating between 1.8-300 K for DC applied field between -7 to +7 T. Measurement were performed on ground polycrystalline samples and each sample was wrapped in a polyethylene membrane. The magnetic data were corrected for the sample holder and the diamagnetic contributions. Altering current (AC) susceptibility measurements were performed under an oscillating AC field of 3.78 Oe and AC frequencies ranging from 0.1 to 1500 Hz. The samples were checked for the presence of ferromagnetic impurities by measuring the magnetization as a function of the magnetic field at 100 K and all samples were determined to be free of such impurities.

Diffuse Reflectance Spectroscopy

Diffuse reflectance measurements were performed using an Agilent Cary 5000 UV-Vis-NIR spectrometer in the range of 200-2000 nm. The data were collected with the use of Praying Mantis$^{\text{TM}}$ accessory by Harrick scientific. Baseline corrections were completed with Spectralon® reference.

Luminescence Measurement

Spectra were obtained on crystalline sample dispersed on glass slides with a custom-built hyperspectral microscope (IMA Upconversion$^{\text{TM}}$ by PhotonEtc, Montreal, Canada), UV excitation source (Nikon Halogen

Lamp (IntensiLight 100 W) with a single band DAPI filter cube for 390nm UV excitation. an inverted optical microscope (Nikon Eclipse Ti-U), a set of galvanometer mirrors and a Princeton Instruments SP-2360 monochromator/spectrograph. A 400 nm long-pass filter (Thorlabs) was inserted at the emission side of the DAPI cube in order to cut off the excitation wavelength. Emission in the NIR region was detected using a deep cooled InGaAs camera (BaySpec). Data analysis and plotting were performed with the instrument's PHySpecV2 software as well as OriginPro®

2.3.3 Synthesis

2.3.3.1 Synthesis of (2-pyridinylmethylidene)-3-hydrazinyl-1,2,4,5-tetrazine (Htzpy):

3-(3,5-dimethyl-1H-pyrazol-1-yl)-1,2,4,5-tetrazine (**5**) was synthesized according a previously reported procedure with slight modifications[46]:

Triaminoguanidine hydrochloride (1): Guanidine hydrochloride (40 g, 0.418 mol) was suspended in 1,4-dioxane (240 mL). Hydrazine monohydrate solution (60 mL, 1.254 mol) was added under stirring and refluxed for two hours. White precipitate in solution was cooled in room temperature, filtered and washed with 1,4-dioxane and dried under vacuum overnight to yield (**1**) as a white solid (58 g, 0.412 mol, 99%).

1,2-Dihydro-3,6-bis(3,5-dimethyl-1H-pyrazol-1-yl)-1,2,4,5-tetrazine (2): To a slurry of (**1**) (30 g, 0.215 mol) in water (200 mL), 2,4-pentadione (44 mL, 0.43 mol) was added under stirring for 30 minutes. The mixture was refluxed for 2 hours. A yellow precipitate formed over time. The product was filtered, washed with cold water and dried under vacuum to yield (**2**) as a yellow solid (10.68 g, 0.039 mol, 36.5%).

3,6-Bis(3,5-dimethyl-1H-pyrazol-1-yl)-1,2,4,5-tetrazine (**3**): Compound (**2**) (10.68 g, 0.039 mol) was suspended in 50 mL dichloromethane at 0 °C in ice bath. A $NaNO_2$ solution (8.28 g, 0.12 mol) in distilled water (175 mL) was added to the suspension, followed by dropwise addition of 2.86 mL HCl (0.1 mol) to generate a bright red mixture with gas evolution. The red organic layer was collected, and the aqueous layer extracted with 150 mL dichloromethane (x2). The Organic layers were combined, washed with 5% aqueous K_2CO_3, dried thorough $MgSO_4$, filtered and evaporated to yield (**3**) (6 g, 0.022 mol, 56.60%).

3-(3,5-Dimethylpyrazol-1-yl)-6 hydrazino-1,2,4,5-tetrazine (**4**). To a suspension of (**3**) (6 g, 0.022 mol) in acetonitrile (65 mL) was added hydrazine-monohydrate (2.73 ml, 0.05 mol) dropwise. Orange precipitate formed immediately, the slurry was stirred for 30 minutes, filtered, washed with toluene and dried under vacuum to yield 2.5 g of pure product (**4**). The mother liquor was concentrated and dissolved in toluene, filtered and dried to yield additional 0.3 g of the product (**4**). (3.8 g, 0.018 mol, 83.15%).

3-(3,5-Dimethylpyrazol-1-yl)-1,2,4,5-tetrazine (5). Activated manganese oxide (9.56, 0.11

mol) was suspended in tetrahydrofuran (90 mL) and (**4**) (3.8 g, 0.018 mol) was added during the stirring in portion at 0°. The reaction was allowed to stir for 30 minutes, filtered through a bed of Celite and the solvent was evaporated under reduced pressure. The product was dissolved in methylene chloride, filtered through silica gel column and concentrated to yield (**5**) (1.6 g, 0.009 mol, 50%).

(2-pyridinylmethylidene)-3-hydrazinyl-1,2,4,5-tetrazine (Htzpy) (6). To a stirred suspension of (**5**) (1.60 g, 0.009 mol) in EtOH (20 mL, 99%) was added hydrazine monohydrate (0.438 mL, 0.009 mol). Upon addition the reaction takes on a dark red colour. The reaction was allowed to stir for 30 minutes at room temperature and then 2-pyridinecarboxaldehyde (0.855 mL, 0.009 mol) was added. The reaction mixture continued to stir at room temperature for an additional 16 hours, while a bright orange precipitate slowly began to form. The mixture was then filtered, the solid was washed with EtOH, and dried under vacuum for 1 hour. Yield (80%, 1.61 g). ^1H NMR (DMSO-d_6, 400 MHz): δ = 7.39(m, 1H, Py), 7.86 (m, 1H, Py), 7.97 (m, 1H, Py), 8.34 (s, 1H, N=CH), 8.59 (m, 1H, Py), 10.02(s, 1H, Tz), 12.60 (s, 1H, NH). Elemental analysis: calculated (found)%: C: 47.76 (48.05), N: 48.73 (48.52), H: 3.51 (3.20). IR data (ATR, cm^{-1}) : 3219 (w), 3014 (w), 2903(w), 1597 (m), 1575 (s), 1559 (w), 1486 (m), 1464 (s), 1431 (s), 1362 (m), 1329 (w), 1287 (w), 1230 (w), 1190 (w), 1163 (w), 1093 (m), 1082 (m), 1048 (m), 989 (m), 936 (s), 841 (w), 790 (m), 706 (m), 644 (w), 527 (m).

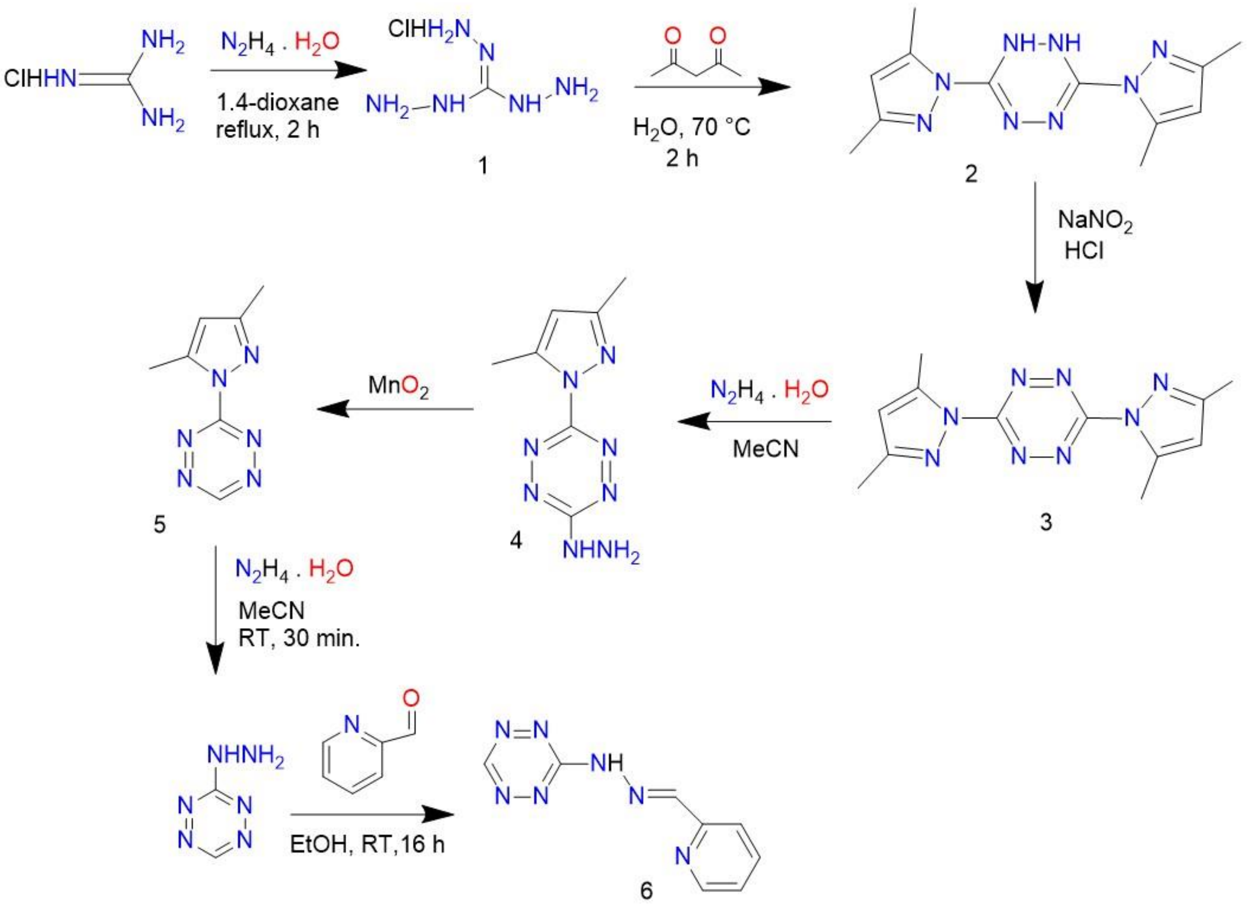

Scheme 2.3. Synthetic procedure for (2-pyridinylmethylidene)-3-hydrazinyl-1,2,4,5-tetrazine (Htzpy).

2.3.3.2 Synthesis of [La^{III}Cl$_3$(Htzpy)$_2$].1.2MeOH (**i**): A solution of Htzpy (**6**) (50.29 mg, 0.25 mmol) in MeCN (5mL) and MeOH (3 mL) was added to a solution of LaCl$_3$.6H$_2$O (44.16 mg, 0.125 mmol). The reaction mixture was allowed to stir for 5 minutes and filtered. X-ray quality orange crystals were obtained via diethyl ether diffusion method after two days. Crystals were collected by vacuum filtration and washed with MeCN and then diethyl ether. Yield = 37.10 %, IR data (ATR, cm^{-1}): 3332 (br), 2963 (w), 1574 (s), 1561 (w), 1498 (w), 1564 (m), 1436 (w), 1372 (m), 1334 (m), 1310 (w), 1232 (m), 1196 (w), 1171 (w), 1149 (w), 1110 (m), 1058 (m), 109 (m), 953 (m), 918 (s), 848 (w), 772 (m), 745 (w), 672 (br), 634 (m). Elemental Analysis calculated (found)%: N: 22.57 (26.15), C: 28.08 (28.09), H: 3.09 (2.98).

2.3.3.3 Synthesis of [Ln^{III}Cl$_2$(Htzpy)$_2$(MeOH)]Cl.aMeOH (Ln^{III} = Tb(ii), Dy(iii), Ho(iv), Er(v), a(**ii**) = **4.61,** a(**iii**) **= 2.11,** a(**iv**) = **4.61 ,** a(**v**) = **4.61):** A solution of Htzpy (**6**) (50.29 mg, 0.25 mmol) in MeCN (5mL) and MeOH (3 mL) was added to a solution of LnCl$_3$.6H$_2$O for (**ii**) (46.67 mg ,0.125 mmol), for (**iii**) (47.11 mg , 0.125 mmol), for (**iv**) (47.47 mg, 0.125 mmol), and for (**v)** (47.71 mg, 0.125 mmol) in MeOH (5 mL). The reaction mixture was allowed to stir for 5 min and filtered. X-ray quality orange crystals were obtained via diethyl ether diffusion method after two days. Crystals were collected by vacuum filtration and washed with MeCN and then diethyl ether. Yield = 29.07 % for (**ii**), 35.25% for (**iii**), 33.98 % for (**iv**) and 35.48 % for (**v**). IR data (ATR, cm^{-1}) for (**ii**): 3323 (br), 1614 (w), 1579 (m), 1562 (w), 1504 (m), 1467 (s), 1439 (w), 1377 (m), 1336 (w), 1312 (w), 1233 (m), 1179 (m), 1151 (m), 1110 (m), 1093 (s), 1060 (s), 1009 (s), 964 (m), 920 (s), 852 (w), 774 (s), 748 (w), 676 (br), 633 (m). For (**iii**): 3192(br), 2274 (w), 1578 (s), 1505 (m), 1472 (s), 1440 (w), 1377 (m), 1336 (w), 1312 (w),1234 (w), 1203 (w), 1180 (w), 1150 (w), 1111 (m), 1094 (m), 1061 (m), 1011 (w), 965 (w),920 (s), 852 (w), 775 (m), 748 (w), 671 (w), 634 (w), 541 (w), for (**iv**): 3277 (br), 1619 (m), 1579 (s),1504 (m),1464 (s),1373 (s), 1345 (w), 1312 (w),1230 (m), 1199 (w), 1150 (m), 1108 (m), 1090 (s),1057 (m), 1004 (m), 916 (s), 847 (w), 774 (s),748 (w), 631 (w), 631 (w), for (**v**): 3100(br), 2775 (w), 1580 (s), 1505 (w), 1465 (s), 1440 (w), 1378 (m), 1336 (w), 1151 (w), 1111(w), 1094 (m), 1061 (m), 1011 (w), 965 (w), 921 (s), 854 (w), 774 (m), 747 (w), 671 (m), 634 (w), 537 (w). Elemental Analysis calculated (found)% for (**ii**): N: 21.26 (25.34), C: 25.73 (25.43), H: 2.86 (2.92), for (**iii**): N: 21.04 (24.93), C: 26.27 (26.04), H: 2.87 (2.70), for (**iv**): N: 21.13 (25.38), C: 25.7 (25.64), H: 2.79 (2.79) and for (**v**): N: 21.04 (24.70), C: 25.59 (25.95), H: 2.78 (2.99).

2.3.3.4 Synthesis of [Yb^{III}Cl$_2$(Htzpy)$_2$]Cl.2.46MeOH (vi): A solution of Htzpy (**6**) (50.29 mg, 0.25 mmol) in MeCN (5mL) and MeOH (3 mL) was added to a solution of YbCl$_3$.6H$_2$O (48.43 mg, 0.125 mmol) in MeOH (5 mL). The reaction mixture was allowed to stir for 5 min and filtered. X-ray quality orange crystals were obtained via diethyl ether diffusion method after two days. Crystals were collected by vacuum filtration and washed with MeCN and then diethyl ether. Yield = 45.86%. IR data (ATR, cm^{-1}): 3015 (br), 1576 (s), 1564 (w), 1505 (w), 1475 (m), 1440 (w), 1376 (m), 1335 (w), 1311 (w), 1234 (m), 1199 (w), 1178 (w), 1113 (w), 1098 (w), 1062 (w), 1009 (w), 914 (m), 914 (s), 850 (w), 7077 (m), 635 (m). Elemental Analysis calculated (found) %: N: 22.04 (25.90), C: 27.64 (27.34), H: 3.05 (2.75).

Table 2.1 Crystallographic data for Htzpy and complexes (i), (ii), (iii), (iv), (v), (vi). Fractional numbers displays the fraction of solvents in the structure.

Empirical formula	**$C_8H_7N_7$**	**C_{18} $H_{17.77}$ Cl_3 La $N_{14.62}$ $O_{0.19}$ (i)**	**C_{41} H_{64} Cl_6 N_{28} O_9 Tb_2 (ii)**	**C_{18} H_{22} Cl_3 Dy N_{14} O_2 (iii)**	**C_{41} H_{64} Cl_6 Ho_2 N_{28} O_9 (iv)**	**C_{41} H_{64} Cl_6 Er_2 N_{28} O_9 (v)**	**$C_{19.67}$ $H_{20.33}$ Cl_3 $N_{15.67}$ $O_{0.33}$ Yb (vi)**
Formula weight	201.88	687.22	1623.74	735.34	1635.76	1640.42	760.93
Temperature (K)	200(2)	200(2)	200(2)	201(2)	200(2)	200(2)	200(2)
Wavelength (Å)	0.71073	0.71073	0.71073	0.71073	0.71073	0.71073	0.71073
Crystal system	Monoclinic	Monoclinic	Triclinic	Triclinic	Triclinic	Triclinic	Monoclinic
Space group	P 2_1/c	P 2_1/n	P -1	P -1	P -1	P -1	P 2_1/n
a (Å)	6.863(9)	13.155(1)	9.302(7)	9.280(4)	9.251(2)	9.282(10)	12.728(3)
α°)	90	90	110.112 (10)	110.01 (10)	109.9010 (10)	109.882 (2)	90
b (Å)	19.77(3)	15.9424 (15)	13.1398 (9)	13.1752 (6)	13.140 (3)	13.146 (15)	12.807 (3)
β°)	109.804 (15)	108.6150 (10)	91.9930 (10)	92.0320 (10)	91.966(1)	91.856(2)	98.701 (3)
c (Å)	7.125 (10)	13.1772 (13)	15.3669 (11)	15.3273 (7)	15.268(3)	15.303(1)	18.112 (4)
γ (°)	90	90	109.9530 (10)	110.08	110.1930 (10)	110.26(2)	90
Volume (Å^3)	910(2)	2619.1(4)	1633.2 (2)	1628.78 (13)	1613.6(6)	1623.5(3)	2918.4 (11)
Z	4	4	1	2	1	1	4
Density g/cm^{-3}	1.469	1.743	1.651	1.499	1.683	1.678	1.732
Absorption coefficient mm^{-1}	0.103	1.977	2.463	2.578	2.753	2.884	3.521
F(000)	416	1351	810	722	814	816	1487
Reflections collected	14910	32078	49170	19779	12465	19298	36056

Independent reflections	14910	6459	8888	7802	7951	8052	7508
Completeness to theta = 25.242° (%)	99.9	100.0	100.0	99.9	99.2	100.0	100.0
Goodness-of-fit on F^2	0.974	1.006	1.178	1.042	1.028	1.002	1.011
R_1, wR_2 [I>2sigma(I)]	0.0578, 0.1359	0.0475, 0.0835	0.0320, 0.0733	0.0173, 0.0434	0.0302, 0.0636	0.0462, 0.0936	0.0384, 0.0862
R_1, wR_2 (all data)	0.1302, 0.1700	0.0851, 0.0967	0.0514, 0.0837	0.0189, 0.0442	0.0377, 0.0667	0.1004, 0.1158	0.0580, 0.0939

$^aR = R_1 = \Sigma||F_o| - |F_c||/\Sigma|F_o|$; $wR_2 = \{\Sigma[w(F_o^2 - F_c^2)2]/\Sigma[w(F_o^2)^2]]\}^{1/2}$; $w = 1/[\sigma^2 (F_o^2)+(ap)^2 + bp]$, where $p = [\max(F_o^2 ,0) + 2F_c^2]/3$.

2.4 Crystal Structures

2.4.1 Crystal Structure of Htzpy

To have information about the ligand structure and coordination sites, single crystal X-ray diffraction was performed on the ligand Htzpy (**6**). The crystals suitable for X-ray diffraction were obtained by crystallization from acetone. The ligand crystallizes in the monoclinic $P2_1/c$ space group and it is comprised of three specific moieties: the pyridine ring, the hydrazone linker and terminal tetrazine ring. It is expected that these three key components make three different coordination pockets with donor atoms including one N from the pyridyl group (N1), one N from the hydrazone linker (N2) and one N atom from tetrazine ring (either N4 or N6). The C-N bond distances in tetrazine are 1.351(4), 1.38(4), 1.361(4) and 1.409(4) Å which indicates distorted tetrazine structure. However, the N-N bond distances 1.322(3) and 1.32(3)Å are in agreement with the previously reported tetrazine ring.[47] As a measure of the planarity, the angle between the plane of C atoms in pyridine ring and the central hydrozone C6, N2, N3, C7 plane was measured as 0.66° which basically shows that they are co-planar. The ^{1}H NMR of Htzpy consisted of three singlets and four multiplets peaks; the latter are attributed to pyridine ring. The singlet peak at 8.34 ppm is characteristic of the imine proton within the ligand structure. The proton of the tetrazine ring appeared as a singlet peak at 10.02 ppm. The remaining N-H proton appeared as a singlet peak at 12.60 ppm.[48]

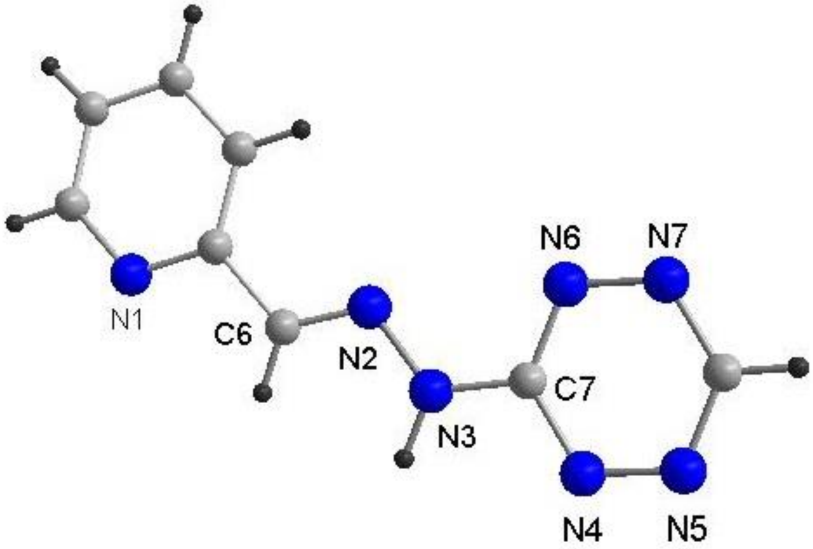

Figure 2.2. Crystal Structure of (2-pyridinylmethylidene)-3-hydrazinyl-1,2,4,5-tetrazine (Htzpy). Color code: blue (N), dark grey (H), light grey (C).

2.4.2 Crystal Structure of [La^{III}Cl$_3$(Htzpy)$_2$] (i)

Single crystal X-ray diffraction analysis revealed that the Htzpy ligands coordinate to the La^{III} ion to yield a mononuclear neutral complex with three chloride ions as depicted in figure 2.3. This complex crystallized in a monoclinic P2$_1$/n space group. The Ln^{III} ion is coordinated to six nitrogens from two different Htzpy ligands and three chloride ions as counter ion that originated from the starting material. As mentioned above, the coordination pockets from the ligand consists of two nitrogens (N$_7$ and N$_{14}$) from pyridyl groups, two nitrogens (N$_6$ and N$_{13}$) from imine groups and two nitrogens (N$_1$ and N$_8$) from tetrazine rings. The bond length between La^{III}-N7 (pyridine) 2.686(4) Å and Ln^{III}-N1 (tetrazine) 2.744(4) Å is higher than previously reported complexes with Yb^{III} and Gd^{III} where tetrazine ring is acting as a bridging ligand.[49] In order to formally evaluate the coordination geometry of the La^{III} complex, a comparative technique was

used by the application of SHAPE program. SHAPE calculates continuous shape measurements (CShMs) of a set of points for example atomic positions relative to the vertices of ideal reference polygons or polyhedral either centered or non-centered.[50] Lanthanides commonly have high coordination numbers and one way to describe their structure is using SHAPE. The comparison of the thirteen reference structures with the La^{III} complex reveals that, the mononuclear La^{III} complex possesses a distorted Muffin (C_s) structure (MFF-9). SHAPE constants are depicted in table 2.3 and the lowest SHAPE constant for the La^{III} complex has been highlighted.

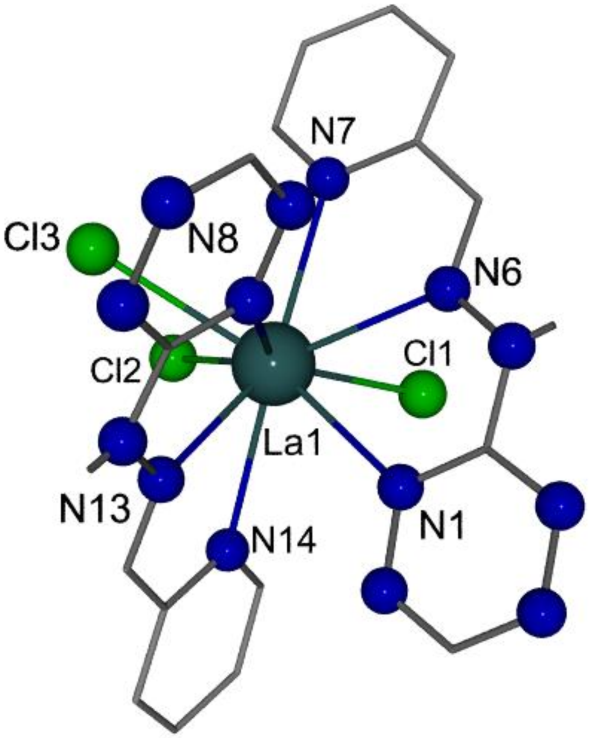

Figure 2.3. Crystal structure of [$La^{III}Cl_3(Htzpy)_2$]. Color code: dark blue: (N), green: (Cl), light blue: (La), all unfilled vertices are carbon atom. Hydorgen atoms are not shown for clarity.

2.4.3 Crystal Structure of [$Dy^{III}Cl_2(Htzpy)_2(MeOH)$]$^+$ (**iii**)

Single crystal X-ray crystallography was used to analyze the structure of complexes (**ii**) to (**v**) and revealed that these species were isostructural and crystallized in the P -1 triclinic space group. Given the isostructural nature of these species and in order to be concise, the structure of the Dy^{III} complex will be discussed as an example. The crystal structure of cationic nine coordinate mononuclear Dy^{III} complex is depicted in figure 2.4 and is composed of two Htzpy (**6**) tridendate ligands including two Ns from pyridine rings (N14 and N7), two Ns from imine groups (13 and N6) and two Ns from tetrazine rings (N8 and N1) as well as two chloride ions and one MeOH molecule. In contrast to complex (**i**), one chloride ion was substituted by a MeOH group, which is consistent with the lanthanide contraction and the smaller size of oxygen atom compared to chloride ion. The structure possessed a chloride anion outside of the cationic sphere of Dy^{III} complex. The Dy-N bond distances in Dy^{III}-pyridine and Dy^{III}-tetrazine is compatible with the previous results with Yb^{III} and Gd^{III} complexes.49 However, the Dy^{III}-Cl bond distances (2.7405)(4) and 2.7052(5) Å) were longer than previously reported Ln^{III}- Cl complexes (2.6152(9) Å).[51] This can be due to more steric hinderance around the Dy^{III} ion in complex (**ii**). SHAPE calculations revealed that the mononuclear Dy^{III} complex was best described as a distorted spherical capped square antiprism C_{4V} (CSAPR-9) geometry. SHAPE constants are depicted in table 2.3 and the lowest SHAPE constant for the Dy^{III} complex has been highlighted. The shortest distance between metals in adjacent cations Tb^{III}...Tb^{III}, Dy^{III}…Dy^{III}, Ho^{III}…Ho^{III} and Er^{III}…Er^{III} in the molecule pack are 6.684, 6.684, 6.664 and 6.679 Å respectively.

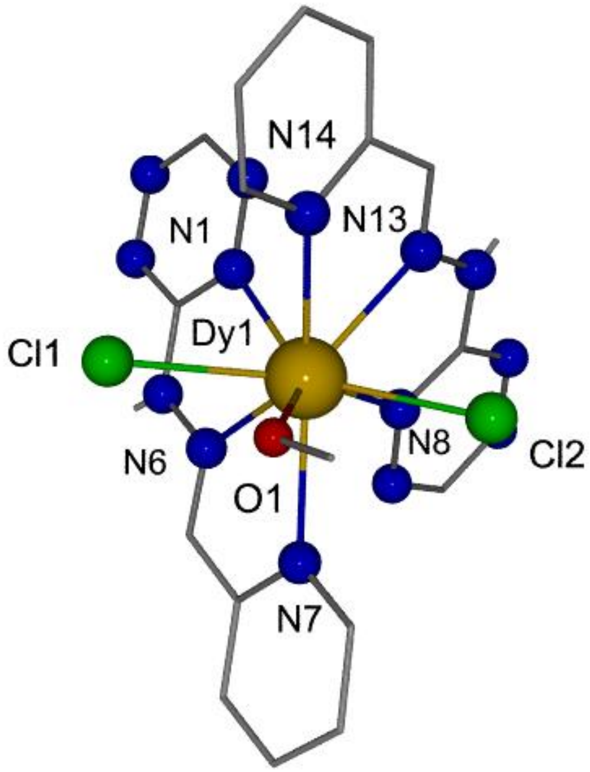

Figure 2.4. Crystal structure of complex [Dy^{III}Cl$_2$(Htzpy)$_2$(MeOH)]$^+$ Color code: blue: (N), green: (Cl), red: (O), yellow: (Dy) all unfilled vertices are carbon atoms. Hydrogen atoms are not shown for clarity.

2.4.4 Crystal Structure of [Yb^{III}Cl$_2$(Htzpy)$_2$]$^+$(vi)

A single crystal X-ray crystallography study also provided the structure of complex (**vi**). The complex (**vi**) crystallized in P2$_1$/n monoclinic space group. The molecular structure is shown in figure 2.5 and consisted of eight coordinate cationic Yb^{III} complex that was composed of two Htzpy (**6**) ligands. The ligands coordinated through two Ns from pyridine rings (N14 and N7), two Ns from imine groups (N13 and N6) and two Ns from tetrazine rings (N8 and N1). The coordination sphere was completed by two chloride ions giving an overall cationic complex. An outer sphere chloride anion functions as the counterion to this complex. Compared to complexes (**i**) and (**iii**), Yb^{III} complex displayed one less coordination which can be rationalized as due to the lanthanide contraction. The Yb^{III}-N bond distances in Yb^{III}-pyridine and Yb^{III}-

tetrazine as well as the Yb^{III}-Cl are in agreement with previously reported lanthanide complexes.49,51 The angle N_1-Yb^{III}-N_6 (63.32(12)°) is slightly higher than the angle N_1-Dy^{III}-N_6 (61.42(5)°) and N_1-La^{III}-N_6 (58.70(12°), this difference is more in N_1-Yb^{III}-Cl_1 (88.78(8)°) than N_1-Dy^{III}-Cl_1 (72.64(3)°) and N_1-La^{III}-Cl_1 (79.11(9)°) which is due to the lower coordination numbers of Yb^{III} ion and consequently lower steric hindrance around the Yb^{III} ion. According to the SHAPE calculations the Yb^{III} complex is best described as a distorted triangular dodecahedron D_2d. SHAPE constants are depicted in table 2.3 and the lowest SHAPE constant for the Yb^{III} complex has been highlighted.

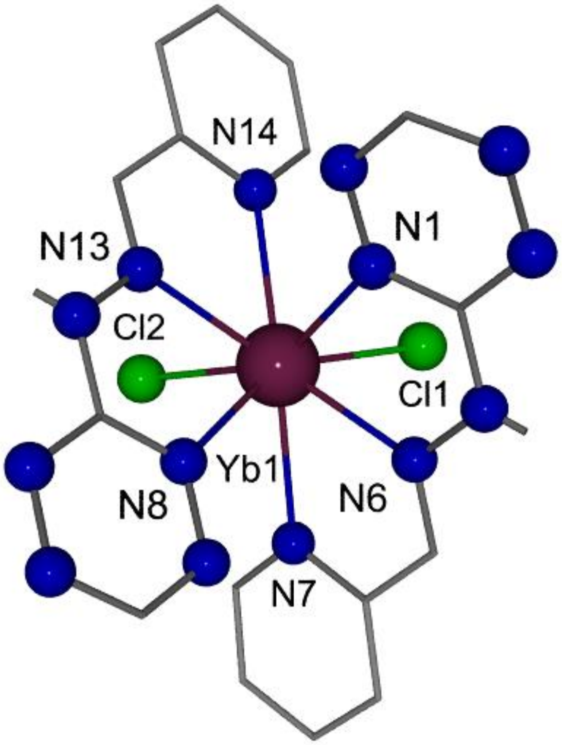

Figure 2.5. Crystal structure of $[Yb^{III}Cl_2(Htzpy)_2]^+$, Color code: blue: (N), green: (Cl), purple: (Yb), all unfilled vertices are carbon atom. Hydorgen atoms are not shown for clarity.

Table 2.2. Selected bond distances and angles for (i), (iii) and (vi)

Bond and angles/complex code	(i)	(iii)	(vi)
Ln(1)-N(7) (Å)	2.686(4)	2.5472(15)	2.524(4)
Ln(1)-N(13) (Å)	2.688(4)	2.5415(15)	2.489(3)
Ln(1)-N(6) (Å)	2.707(4)	2.5510(15)	2.474(3)
Ln(1)-N(14) (Å)	2.713(4)	2.5477(15)	2.547(4)
Ln(1)-N(8) (Å)	2.736(4)	2.5873(15)	2.505(4)
Ln(1)-N(1) (Å)	2.744(4)	2.6046(15)	2.485(3)
Ln(1)-Cl(1) (Å)	2.8093(13)	2.7052(5)	2.5514(13)
Ln(1)-Cl(2) (Å)	2.8262(12)	2.7405(4)	2.5607(12)
Ln(1)-Cl(3) (Å)	2.8976(13)	-	-
N(1)-Ln(1)-Cl(1) (◦)	79.11(9)	72.65(3)	88.78(8)
N(7)-Ln(1)-N(1) (◦)	118.54(12)	124.38(5)	127.25(11)
N(6)-Ln(1)-N(1) (◦)	58.58(12)	61.42(5)	63.32(12)

In general, comparing tetrazine ring bond lengths in the ligand and in the complexes (**i**)-(**vi**) indicates shorter bond lengths for N-N and N-C in the complexes. This compression within the ligand structure is likely due to the coordination to Ln^{III} ions, however, the ligand almost keeps its planarity in all the complexes upon complexation. The average Ln^{III}-N distances for complexes (**i**) to (**vi**) is 2.70, 2.566, 2.563, 2.54, 2.53, 2.44 Å and the coordination number of the complexes as well as groups coordinated to the Ln^{III} from (**i**) to (**vi**) are changed in a way to provide less steric hindrance in the crystal structure which is the evidence of the lanthanide contraction.

Table 2.3 SHAPE constants for La^{III}, Dy^{III}, and Yb^{III} centers in complexes (i), (iii), (vi). The lowest SHAPE constants are highlighted.

SHAPE code	Point group	Description	(i)	(iii)	Shape code	Point group	Description	(vi)
EP-9	D_{9h}	Enneagon	36.71967	34.86324	OP-8	D_{8h}	Octagon	30.853
OPY-9	C_{8v}	Octagonal pyramid	23.32975	23.78910	HPY-8	C_{7v}	Heptagonal pyramid	25.162
HBPY-9	D_{7h}	Heptagonal bipyramid	17.78785	19.65844	HBPY-8	D_{6h}	Hexagonal bipyramid	14.995

JTC-9	C_{3v}	Johnson triangular cupola J3	15.70604	15.33527	CU-8	O_h	Cube	13.822
JCCU-9	C_{4v}	Capped cube J8	10.92437	11.12899	SAPR-8	D_{4d}	Square antiprism	3.996
CCU-9	C_{4v}	Spherical-relaxed capped cube	9.80204	9.14037	TDD-8	D_{2d}	Triangular dodecahedron	1.585
JCSAPR-9	C_{4v}	Capped square antiprism J10	2.49181	2.16222	JGBF-8	D_{2d}	Johnson gyrobifastigium J26	12.089
CSAPR-9	C_{4v}	Spherical capped square antiprism	1.68023	1.02998	JETBPY-8	D_{3h}	Johnson elongated triangular bipyramid J14	29.217
JTCTPR-9	D_{3h}	Tricapped trigonal prism J51	4.05991	2.92522	JBTPR-8	C_{2v}	Biaugmented trigonal prism J50	3.788
TCTPR-9	D_{3h}	Spherical tricapped trigonal prism	2.36319	1.23298	BTPR-8	C_{2v}	Biaugmented trigonal prism	2.541
JTDIC-9	C_{3v}	Tridiminished icosahedron J6	12.11189	12.96008	JSD-8	D_{2d}	Snub diphenoid J84	3.447
HH-9	C_{2v}	Hula-hoop	11.53952	11.00337	-	-		-
MFF-9	C_s	Muffin	1.57875	1.47215	-	-		-

2.5 Magnetic Measurements

2.5.1 Static Magnetic Susceptibility for complex (ii)

Direct current (DC) magnetic measurements were performed on crystalline Tb^{III} sample to investigate the static magnetic performance of the compound between 1.8-300 K with an applied filed of 1000 Oe. As shown in Figure 2.6 temperature-dependent magnetic susceptibility character is observed in complex (**ii**). The room temperature χT value in 1000 Oe is 12.79 cm^3 K mol^{-1} which is in agreement with he theoretical value of 11.80 cm^3 K mol^{-1} for non-interacting Tb^{III} ion ($^7F_{6,}$ S = 3, L = 3, g = 3/2). With decreasing the temperature, the χT value increases up to 14.82 cm^3 K mol^{-1} at 16.03 K which can be ascribed to a weak intermolecular ferromagnetic interaction between two Tb^{III} centers. The observed distance between two Tb^{III} ions of 6.68 Å is small enough for coupling.[52] The χT value then decreases more sharply down to the minimum value of 10.69 cm^3 K mol^{-1} which can be attributed to the thermal depopulation of the crystal field splitting energy levels.[53] Furthermore, the field dependence of the magnetization measured is shown in Figure 2.7 (left), and reveals the rapid increase in magnetization at low fields which eventually reaches the value of 7.60, 7.62, 7.61 and 7.59 μ_B at 1.9, 3, 5, 7 K respectively without any sign of saturation. The value of the magnetization is lower than the expected saturation value of 9 μ_B for an isolated Tb^{III} ion. This can be attributed to the magnetic anisotropy and/or low-lying excited state. This conclusion is supported by non-superposition of the M versus HT^{-1} plots shown in Figure 2.7 (right).[54] Investigation into this did not show frequency-dependent slow magnetic relaxation.

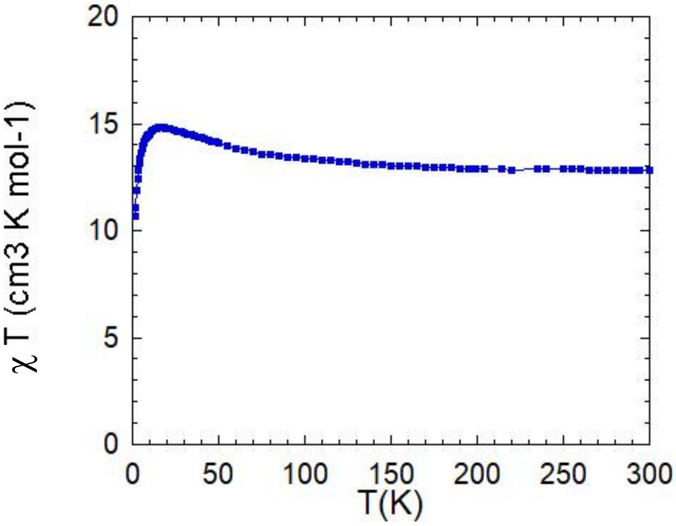

Figure 2.6. χT *vs.* T for (ii) under applied DC field of 1000 Oe.

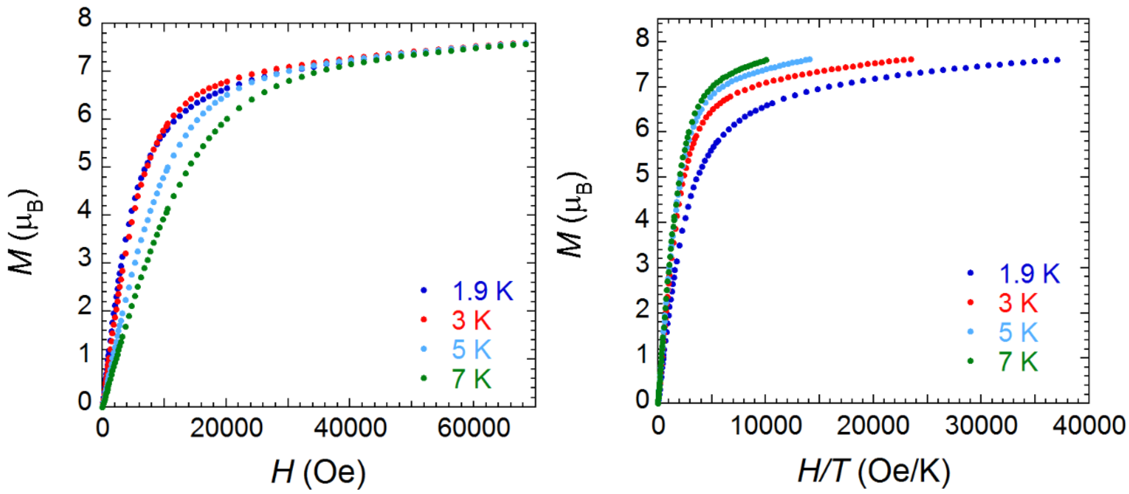

Figure 2.7. Magnetization *vs*. field (left) and reduced magnetization plot (right) for (ii) between 1.9 and 7 K.

2.5.2 Static Magnetic Susceptibility for complex (iii)

Direct current (DC) magnetic susceptibility was studied for the Dy^{III} complex in an applied field of 1000 Oe over a temperature range of 1.8-300 K. As shown in Figure 2.8, The observed χT value at 300 K is 13.54 cm^3 K mol^{-1} which is in agreement with the expected value for an isolated Dy^{III} ion 14.17 cm^3 K mol^{-1} ($^6H_{15/2}$, S = 5/2, L = 5, J = 15/2, g_J = 4/3) and may be attributed to the splitting of the $^6H_{15/2}$ ground state.[55] The χT value gradually decreases with reducing the temperature to 11.40 cm^3 K mol^{-1} at 18.9 K and then further decreases in a slightly sharper manner to reach a minimum value of 8.57 cm^3 K mol^{-1} at 1.8 K which is evidence of depopulation of the Dy^{III} m_J levels. Another possibility is that as the distance between the two Dy^{III} atoms is 6.68 Å, there may be weak antiferromagnetic interactions between Dy^{III}…Dy^{III} cores of adjacent molecules in the structure. In addition, the M versus H and M versus HT^{-1} at 1.9, 3, 5, 7 K as shown in Figure 2.9 left and right respectively, exhibited a rapid increase at low fields and eventually reached maximum values of 5.92, 5.92, 5.89 and 5.84 μ_B at the highest field of 70 kOe respectively. These values are considerably lower than the expected saturation value of 10 μ_B for an isolated Dy^{III} ion. Furthermore, the M versus HT^{-1} shows lack of superimposition. Both of these observations indicate the presence of magnetic anisotropy and/or low-lying excited states. Dynamic magnetic properties will be discussed below.[56]

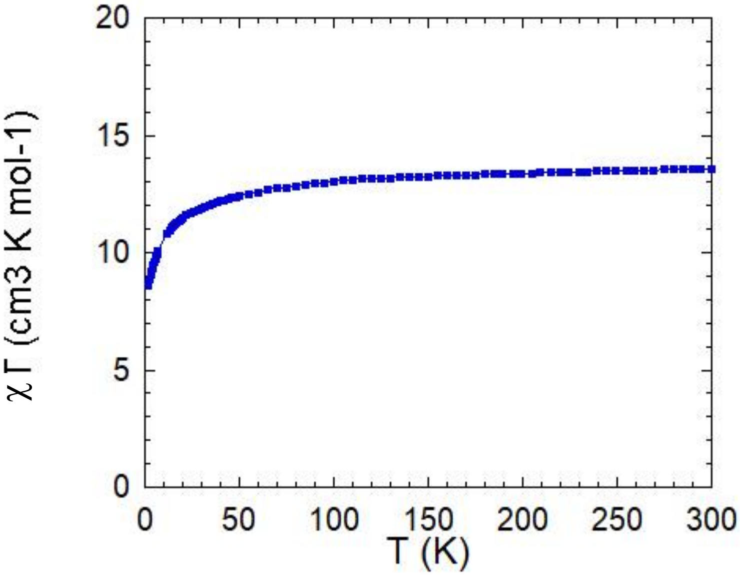

Figure 2.8. χT *vs.* T for (iii) under applied DC field of 1000 Oe.

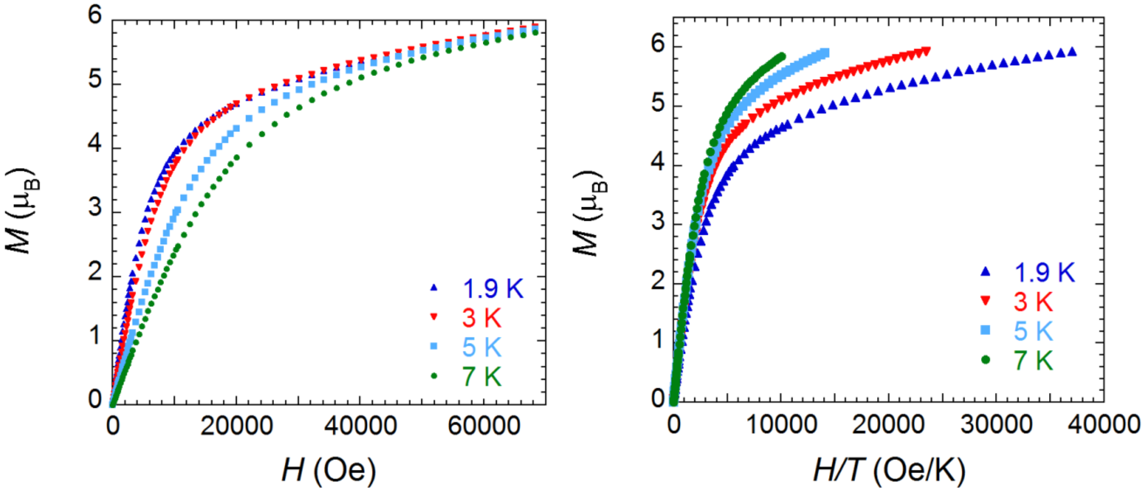

Figure 2.9. Magnetization *vs.* field (left) and reduced magnetization plot (right) for (iii) between 1.9 and 7 K.

2.5.3 Dynamic Magnetic Susceptibility for complex (iii)

In order to study the potential slow magnetization relaxation, altering current (AC) measurements were performed on the Dy^{III} complex. Both in-phase (χ') and out-of-phase (χ'') magnetic susceptibilities were obtained in the temperature range of 1.8-8 K. There is no frequency dependent relationship in zero-applied DC field. However, in the presence of 2400 Oe optimum DC applied field, a minimal frequency dependence AC susceptibility was observed. The presence of peaks shifting to lower frequencies upon decreasing the temperature is indicative of slow magnetic relaxation and SMM behaviour.56 However, mostly, overlapping peaks were observed in out-of-phase AC susceptibility plot which indicated quantum tunnelling of magnetization. The out-of-phase magnetic susceptibility (χ'') versus frequency between 2.4 and 8 K is depicted in figure 2.11 at the left.

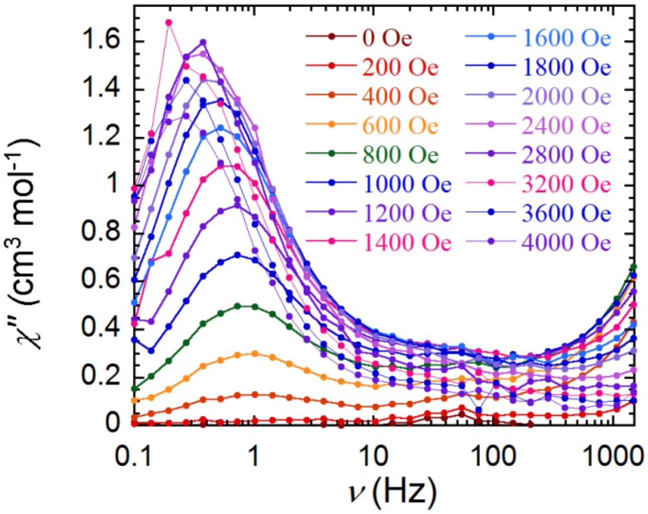

Figure 2.10. Out of phase magnetic susceptibility (χ'') *vs.* frequency in different DC applied field between 0 and 4000 Oe for (iii).

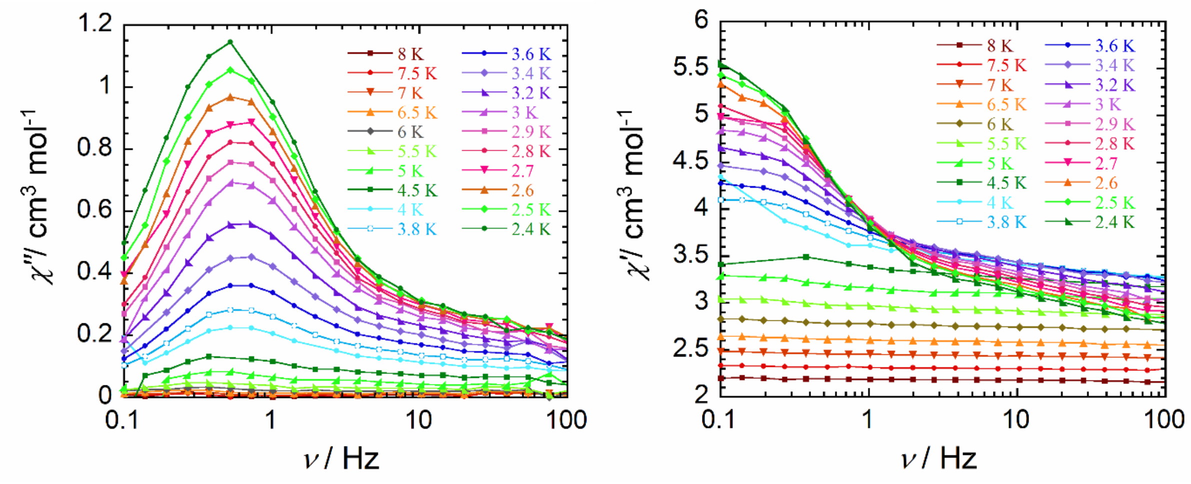

Figure 2.11. Out-of-phase magnetic susceptibility (χ'') *vs*. frequency between 2.4 and 8 K (left) and In-phase magnetic susceptibility (χ') *vs*. frequency between 2.4 and 8 K (right) for (iii).

The magnetization relaxation time in the form of lnτ derived from the frequency dependent measurements was plotted as function of 1/T. Above 1.8 K the relaxation follows thermal relaxation process allowing for the calculation of the energy barrier of 3.024 K with the pre-exponential factor of $\tau_0 = 7.22\times 10^{-4}$ s based on Arrhenius equation.

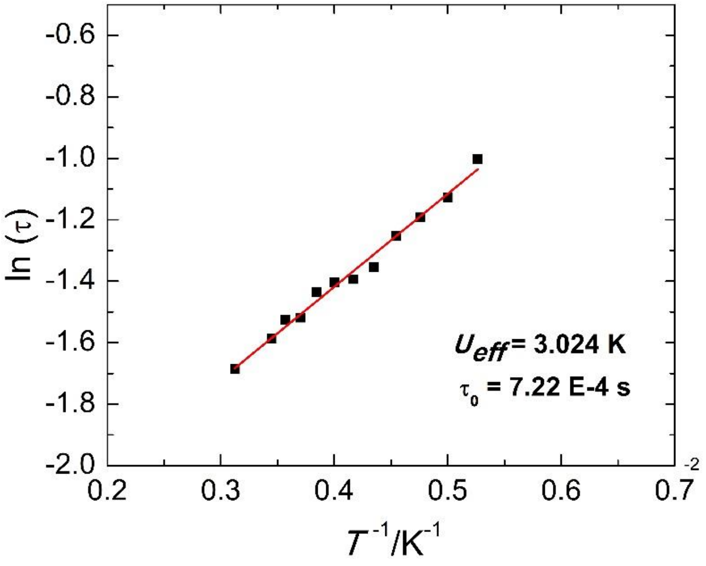

Figure 2.12. lnτ *vs*. 1/T Arrhenius plot for (iii).

2.5.4 Static Magnetic Susceptibility for Complex (iv)

DC magnetic susceptibility studies were conducted on compound (**iv**) in an applied field of 1000 Oe and temperature range of 1.8-300 K. The observed χT value at 300 K is 14.35 cm^3 K mol^{-1} which is consistent with the expected value of 14.07 cm^3 K mol^{-1} for the isolated Ho^{III} ion ($^5I_8$, S = 2, L = 6, J = 8, g_J = 5/4). As seen in Figure 2.13, upon decreasing the temperature, the χT value decreases gradually down to 12.16 cm^3 K mol^{-1} at 28.0 K and further decreases sharply to the minimum value of 4.3 cm^3 K mol^{-1} at 1.8 K. The decrease at low temperatures can be attributed to the thermal depopulation of the m_J sublevels. Meanwhile, again, as the distance between two Ho^{III} nuclei is 6.66 Å, antiferromagnetic interactions are possible. The magnetization shown in Figure 2.14 (left), increases rapidly at low field and then slowly reaches the maximum magnitude of 7.69, 7.70, 7.67 and 7.61 μ_B at 1.9, 3, 5 and 7K which are much lower than the expected value for free Ho^{III}. M versus HT^{-1} plots depicted in Figure 2.14 (right), are not superimposed even at the highest possible field which can be attributed to the existence of magnetic anisotropy and/or strong crystal field effects.53 Investigation into this possibility did not show frequency-dependent slow magnetic relaxation.

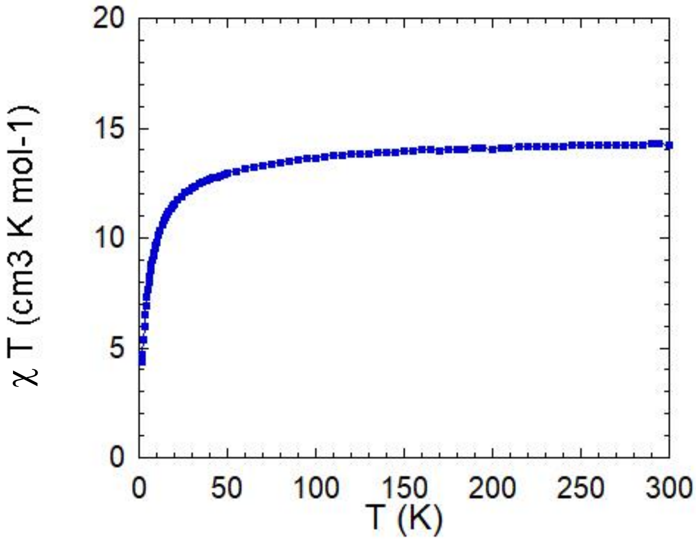

Figure 2.13. χT *vs*. T for (iv) under applied DC field of 1000 Oe.

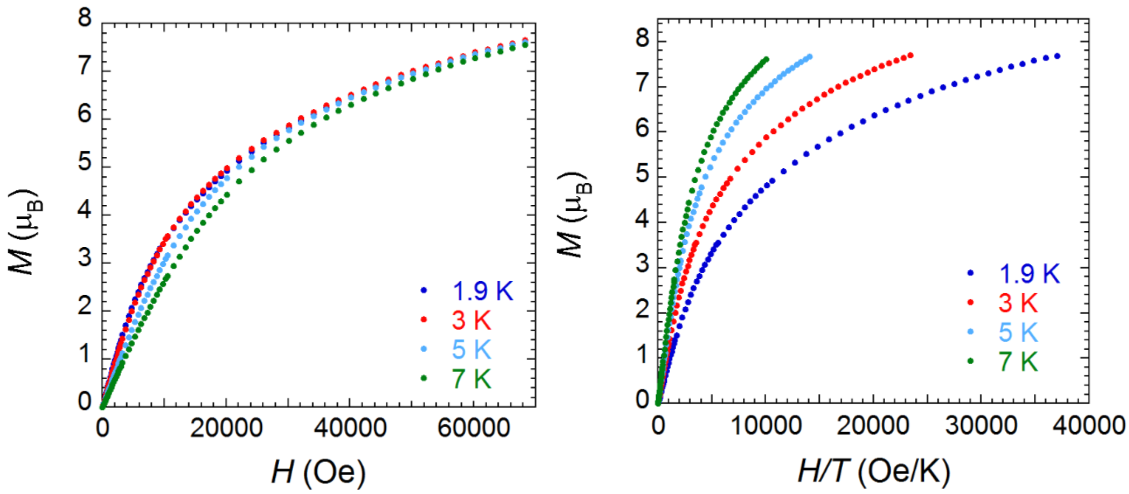

Figure 2.14. Magnetization *vs.* field (left) and reduced magnetization plot (right) for (iv) between 1.9 and 7 K.

2.5.5 Static Magnetic Susceptibility for complex (v)

The static magnetic properties of Er^{III} complex were measured in 1000 Oe over a temperature range of 1.8-300 K as shown in figure 2.16. The temperature dependence of the DC magnetic susceptibility is very similar to Er complexes previously reported.[57] The observed χT value at 300 K is 11.84 cm^3 K mol^{-1} which is consistent with the value for the isolated Er^{III} ion 11.48 cm^3 K mol^{-1} ($^4I_{15/2}$, S = 3/2, L = 6, J = 15/2, g_J = 6/5). As shown in Figure 2.15, the χT gradually starts decreasing at lower temperatures from 139.66 K up to 7.32 cm^3 K mol^{-1} which can be attributed to the depopulation of excited m_J sublevels split by the crystal field effect and magnetic anisotropy. The field dependent magnetization of Er^{III} complex at 1.9, 3, 5 and 7 K is presented in Figure 2.16 (left) and showed a sharp increase at low field and finally reaches 5.90, 5.90, 5.88 and 5.84 μ_B at the maximum applied field of 70 kOe. This highest magnetization value is much lower than theoretical saturation value of 9 μ_B which is attributed to the single-ion anisotropy of the Er^{III}. In addition, the M versus HT^{-1} plots shown in Figure 2.16 (right) are not superimposed which again supports the existence of magnetic anisotropy.[58] Dynamic magnetic properties will be discussed below.

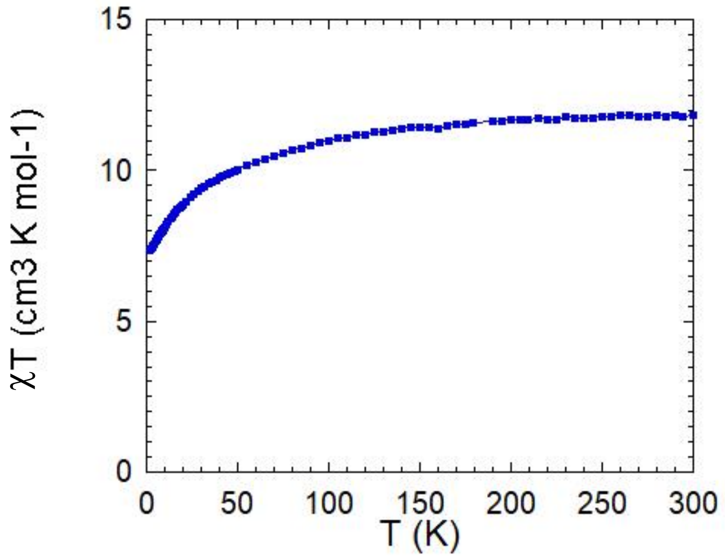

Figure 2.15. χT *vs*. T for (v) under applied DC field of 1000 Oe.

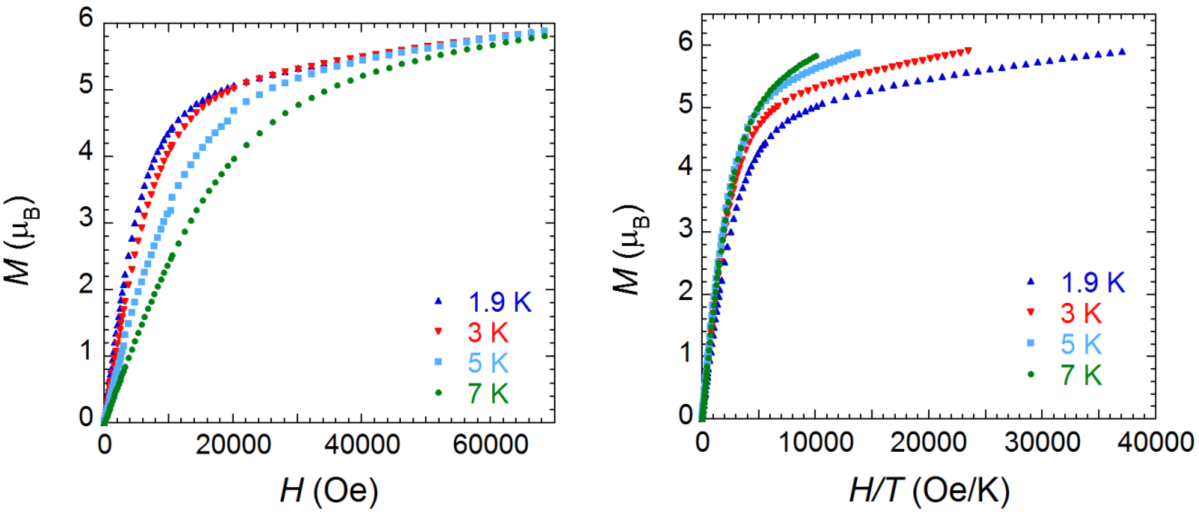

Figure 2.16. Magnetization *vs*. field (left) and reduced magnetization plot (right) for (v) between 1.9 and 7 K.

2.5.6 Dynamic Magnetic Susceptibility for Complex (v)

In order to investigate the SMM behaviour of complex (**v**) AC magnetic susceptibility measurements were performed in the temperature range of 2 to 5.5 K and in order to reduce the quantum tunnelling effect the measurements have been done in the optimal DC field of 800 Oe. As seen in Figure 2.18 (left), the shifting of the peaks to lower frequencies upon decreasing the temperature indicates the single-molecule magnet behaviour of the Er^{III} complex. The thermally activated relaxation follows Arrhenius-like behaviour (see Figure 2.19) $\tau = \tau_0 \exp(U_{eff}/KT)$ where the anisotropic energy barrier is calculated to be $U_{eff} = 67.5$ K and $\tau_0 = 6.67 \times 10^{-4}$ s in temperatures above 2.5 K.

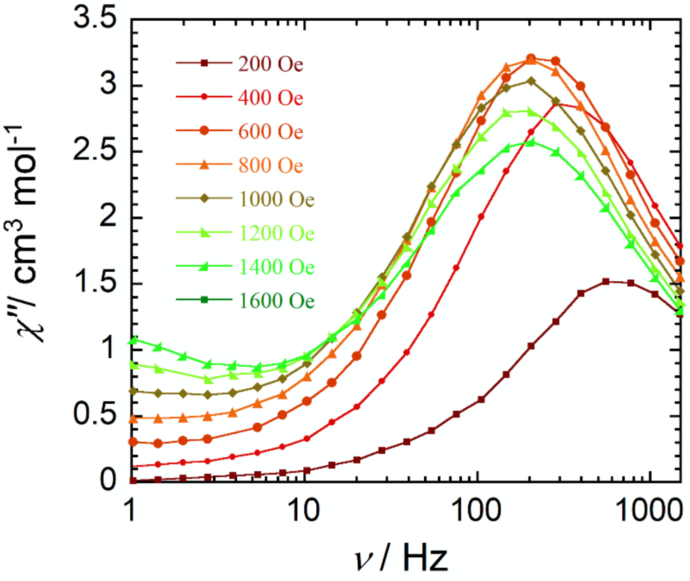

Figure 2.17. Out-of-phase magnetic susceptibility (χ'') *vs.* frequency in different DC applied field between 200 and 1600 Oe.

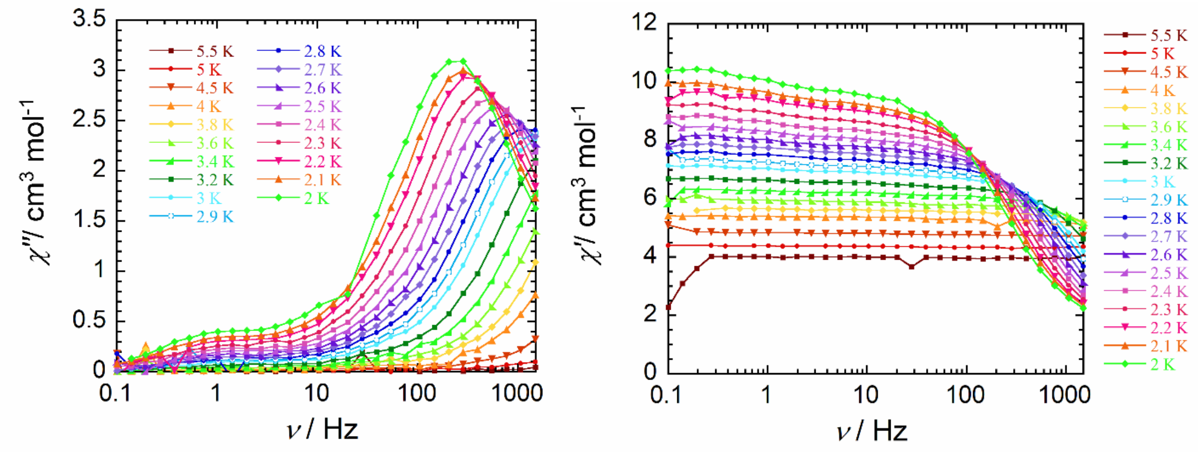

Figure 2.18. Out-of-phase magnetic susceptibility (χ'') *vs*. frequency between 2.4 and 8 K (left) and In-phase magnetic susceptibility (χ') *vs*. frequency between 2 and 5.5 K (right) for (v).

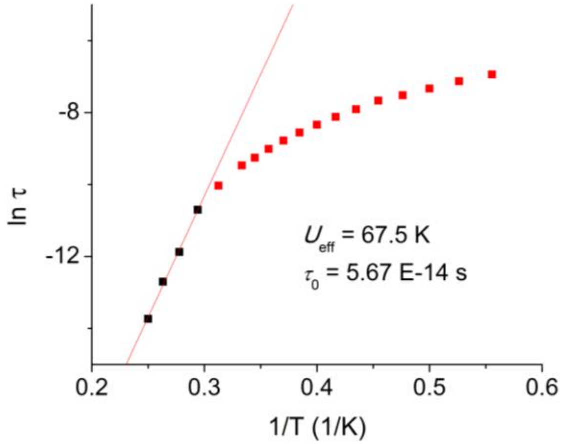

Figure 2.19. lnτ *vs*. 1/T Arrhenius plot for (v).

2.6 Optical Measurements

2.6.1 UV-Vis Spectroscopy of compound (vi)

In order to investigate the solid-state electronic structure and further luminescence measurements of complex (**vi**), the solid crystalline material was analyzed by diffuse reflectance spectroscopy at room temperature. As shown in Figure 2.20 over the range of 200-550 nm, two sharp and one broad absorption maxima exist. The absorption maxima at 256 and 306 were assigned to the ligand centered transition and may be attributed to the intra-ligand charge transfer ($\pi \rightarrow \pi^*$) transitions. The existence of the broad peak from 404 to 510 corresponds to the overlapping of ($\pi \rightarrow \pi^*$) and ($n \rightarrow \pi^*$) transitions which essentially originate from the tetrazine moiety.[59] Existence of slight shoulder at 416 nm may be due to the metal to ligand charge transfer (MLCT) according to the previously reported literature with transition metal complexes and tetrazine based ligands.[60,61] At 974 nm a very weak absorption band is detected that is attributed to the f-f transition in Yb^{III} ion ($^2F_{7/2} \rightarrow {}^2F_{5/2}$), this weak absorption can be explained by Laporte forbidden f-f transition law.

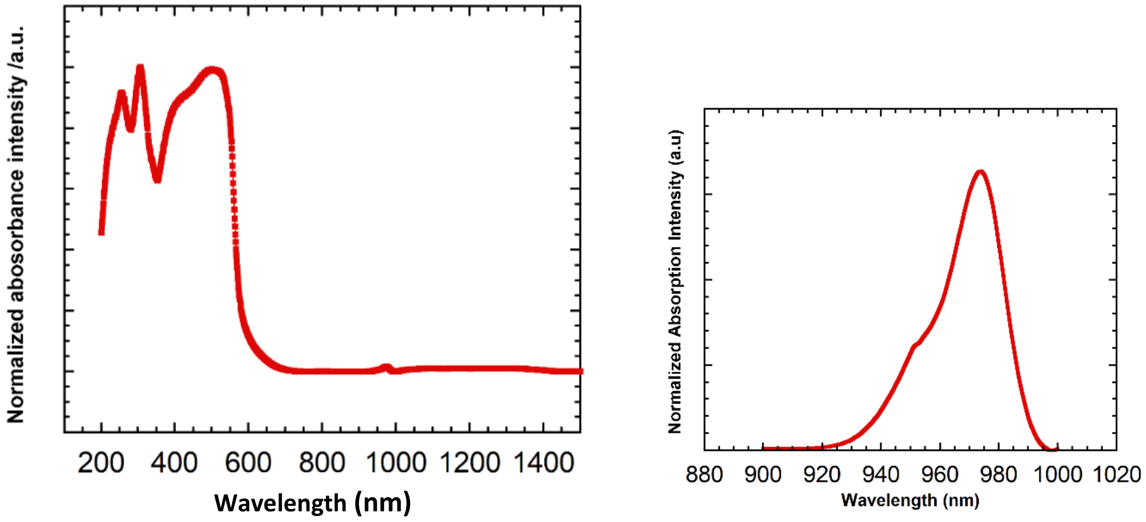

Figure 2.20. Normalized solid state absorption of (vi) (left) and the expansion of f-f transition of (vi) at 974 nm (right).

2.6.2 Luminescence Spectroscopy of (vi)

Luminescence spectra of (**vi**) were obtained on solid crystalline sample dispersed on glass slides with a custom-built hyperspectral microscope equipped with a UV excitation source in the range of 990-1200 nm and yielded a typical near-IR emission centered at 1025.87 nm which is assigned to the $^2F_{5/2} \rightarrow {}^2F_{7/2}$ transition.[62] Monitoring the lanthanide emission peak, ligand absorption is dominant compared to the weak f-f transition thus indicating an efficient sensitization of lanthanide emission through ligand triplet levels. It is noteworthy to mention that the optical activity of the Yb^{III} complex (absorption and emission) is affected by changing the symmetry around the Ln^{III} ion due to the ligand field effect and lanthanide emission may originate from the f orbitals directly as well but sensitization is still dominant.

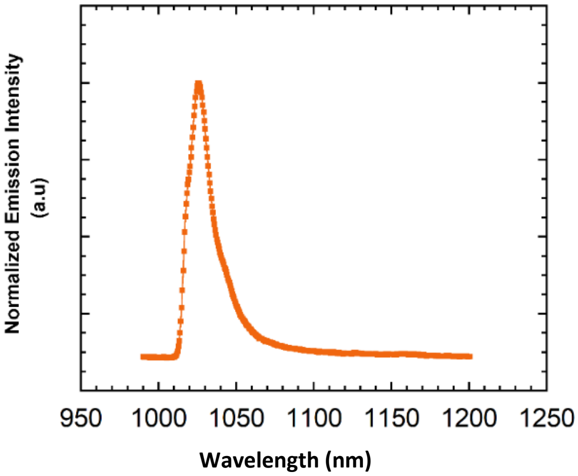

Figure 2.21. Normalized solid state emission of (vi).

2.7 Conclusion

Six lanthanide complexes (La^{III}, Tb^{III}, Dy^{III}, Ho^{III}, Er^{III}, Yb^{III}) were synthesized using a new design of Schiff-base ligand including tetrazine ring within its structure. All of these complexes have been structurally characterized and compared to each other. SHAPE measurements as well as the correlation between the structure of the complexes and lanthanide contraction was made. Magnetic properties of Tb^{III}, Dy^{III}, Ho^{III} and Er^{III} complexes were measured and indicated the existence of strong magnetic anisotropy in all samples. The Tb^{III} complex displayed magnetic measurements suggesting intermolecular ferromagnetic interactions at low temperatures and the decrease in χT value with decreasing temperature can be ascribed to both antiferromagnetic intermolecular interactions and thermal depopulation of their excited state sublevels for Dy^{III}, Ho^{III} and Er^{III} complexes. Dy^{III} and Er^{III} complexes showed single-molecule magnet behaviour with effective energy barriers of 3.02 and 67.5 K respectively. UV-Vis absorption and luminescence measurements were performed on the Yb^{III} complex and the intense emission band at 1025 nm indicates the way to overcome the Laporte forbidden law rule for f-f transitions which is most likely due to the sensitization from the ligand.

2.8 Outlook

Further efforts will be focused on the reduction of the complexes synthesized to achieve the stable radical anion species and enhance the coupling exchange between the lanthanide ion and radical ion to exhibit substantial magnetic properties in the form of ferromagnetic or antiferromagnetic interactions with higher energy barriers at higher blocking temperatures. Examination of the emission properties of the rest of the lanthanide complexes will be performed in future work. The excitation of the reduced form of the complexes may affect their optical activity and their sensitization ability which should be taken into consideration.

Chapter 3 Luminescence Properties of Metal Complexes

3.1 Naphthalimide Based Ligands

As discussed in chapter 1, metal complexes including both transition and lanthanide metal complexes have attracted great interest due to their potential applications as luminescent materials. In this chapter, the photochemical features of two previously reported naphthalimide compounds were explored. In addition a new ligand comprised of naphthalimide ring and dipicolinic acid has been targeted for exploration of photophysical properties. The complexation of these ligands and examination of their absorption and emission properties were attempted.

Cyclic imides and their derivatives have received considerable attention due to their medical[63], polymeric[64], photonics[65] and electronic properties[66]. These cyclic imides are mostly stable to oxidation[67], heat retardant, solvent resistant[68] and possess superior mechanical properties[69]. The reactivity of these compounds is the result of the relative acidity of their NH group which is a direct consequence of having two carbonyl groups.[70] Generally aromatic or aliphatic cyclic imides and their derivatives are obtained by the reaction of dicarboxylic acids and or their corresponding anhydrides with reagents contained a reactive amino group within their structures. Reaction is via a nucleophilic attack of amino group to the anhydride moiety. The General mechanism, of this reaction is shown in Scheme 3.1.

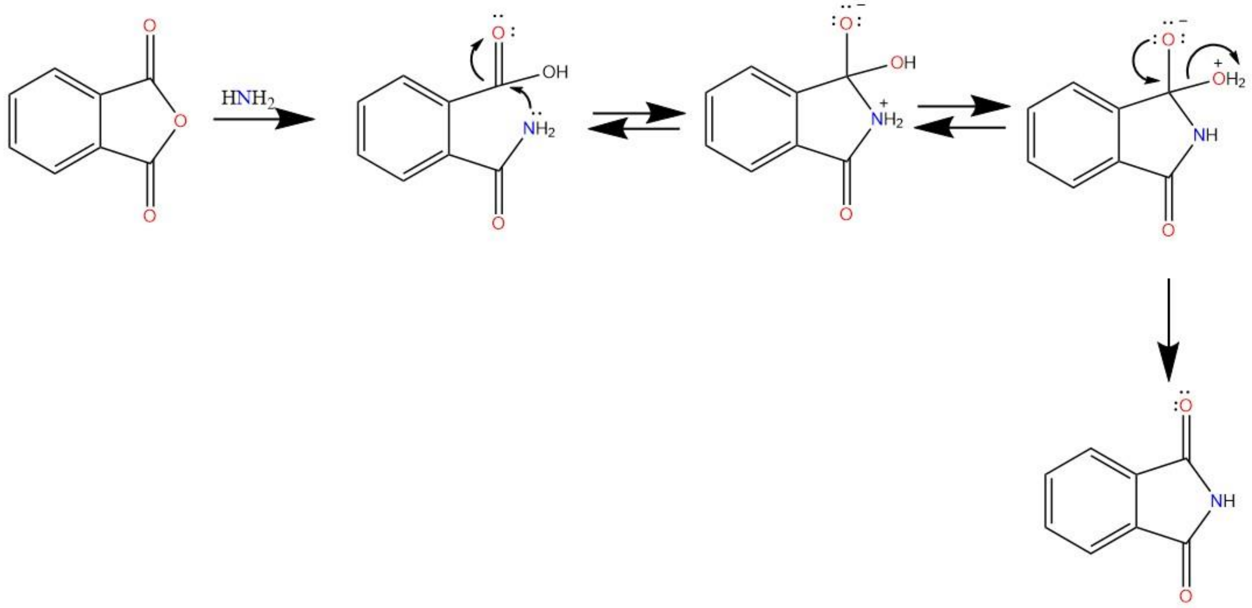

Scheme 3.1. General mechanism of imide formation by direct condensation.

Among the cyclic imides, naphthalimides, constituted of fused aromatic cycles with side carbonyl groups (see Figure 3.1), commonly display large quantum yields and sizeable Stokes shifts. Furthermore, a variety of auxochromic groups can be grafted within their structure to tune their absorption and emission properties.[71] For instance, the Heagy group indicated that pyridine derivatives increase the quantum yield significantly, hence, they are obviously of interest for practical applications.[72] N-Aryl naphthalimides specifically 1,2, 2,3 and 1,8 naphthalimides are among the most common fluorescent dyes and among these three, the 1,8 substitution pattern has the most promising structure to build fluorescence probes or brighteners. Two emissive state (S_1 and S_2) capable of emitting both short wavelength and long wavelength fluorescence exist in the excited stated of these N-Aryl naphthalamides. The long wavelength emission results from a co-planar configuration and short wavelength emission results from an orthogonal orientation. According to this conformational dependence for long wavelength emission, the electronic and steric properties of the N-arene play important roles in their fluorescence properties. Additionally, electron-withdrawing or electron-releasing groups on the N-aryl group have an important impact on short wavelength and long wavelength emission. The Heagy group found that the existence of an electron-withdrawing groups on either the naphthalimide ring or the arene ring decreases the energy of charge transfer effecting the short wavelength emission. On the other hand, electron-donating groups on either moiety were responsible for long wavelength emission. In the case of the naphthalimide ring possessing an electron-donating group and the N-arene ring has an electron-withdrawing group, the dye displays long wavelength emission. Reversing this substitution pattern by having an electron-withdrawing groups on the naphthalene ring and an electron-releasing group on the N-arene ring, both short wavelength and long wavelength emission appeared.[73] N-Aryl naphthalimides are inherently more polar than polycyclic aromatic hydrocarbons such as pyrene and a variety of them have been used as probes for carbohydrates, protein, and bio-thiols such as GSH in aqueous conditions. Therefore, these compounds can potentially display appropriate fluorescence properties in either protic or aprotic solvents.[72] Phthalimide analogues such as naphthalimide derivatives are electron-active and there is scope for their study in a supramolecular environment. 1,8 naphthalimides also show reversible redox properties. Thus, understanding of the redox properties of N-Aryl 1,8 naphthalimides provide information about supramolecular bonding and information on their possibility as electrochemical probes beside or in combination with their photophysical activity (sometimes the photophysical properties of the radical ion excited state are different from those of neutral parent molecule).[74] In spite of these unique properties of N-Aryl naphthalimides and specifically N-Aryl 1,8 naphthalimides, not many transition and lanthanide metal complexes have been reported. In this project, we focused on designing organometallic complexes of 1,8 naphthalimide derived ligands and measuring their optical and electrical activities for sensing applications. Two previously reported naphthalimide based ligands are shown in figure 3.1. These two species are promising candidates for study. For example, 4-(1,8-naphthalimido) benzoic acid displays both a naphthalimide moiety and a carboxylic group[75] and N-(2'-pyridyl)-1,8-naphthalimide72 possesses both naphthalimide and pyridine properties and is expected to increase the fluorescence efficiency and quantum yield.

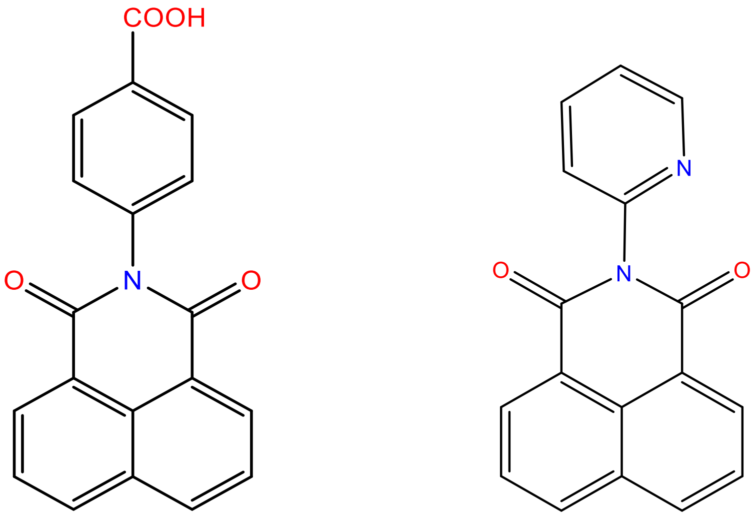

Figure 3.1. Chemical structure of 4-(1,8-Naphthalimido) benzoic acid (benzonap) (left) and N-(2’-pyridyl)-1,8-naphthalimide (pynap) (right).

Additionally, a new ligand constructed with both naphthalimide moiety and dipicolinic acid was proposed for investigation (see Figure 3.2). Dipicolinato based ligands are well-known to form water soluble metal complexes with high emission efficiencies along with their long emission life time.[76] They are also functionalized easily at their para position. Additionally, in lower concentrations cytotoxicity of their lanthanide complexes has been observed.[77] Generally, dicarboxamide pyridine ligand are well known to complex lanthanide ions effectively and they perform well in sensitization.[78,79] Therefore, the combination of 1,8 naphthalimide and dipicolinic acid was proposed to provide higher sensitization and emission efficiencies as well as higher coordination pockets to bond to metal ions which is completely compatible with our final goal to get more qualified sensors.

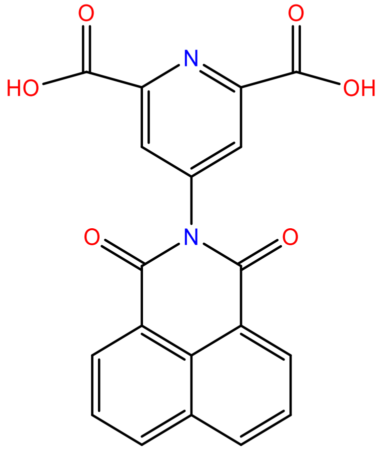

Figure 3.2. Chemical structure of 4-(1,8-Naphthalimido) dipicolinic acid (dipicnap).

3.2 Experimental

3.2.1 Chemicals:

All manipulations were performed under aerobic conditions. All chemicals were used as received from Aldrich and Fisher chemical company without further purifications.

3.2.2 Instrumentations:

IR Spectroscopy

Infrared data were collected in solid state on a Varian 640 FT-IR spectrometer equipped with an ATR in the 600-4000 cm^{-1} range.

NMR Measurements

NMR data were collected using a Bruker Avance 400 spectrometer equipped with an automated sample holder and 4 mm autotuning broadband probe with Z gradient.

Elemental Analysis

Elemental analysis were performed using an Isotope Cube elemental analyser by G.G Hatch Stable Isotope Laboratory, University of Ottawa.

X-Ray Crystallography

Single crystals suitable for X-ray diffraction measurements mounted on the glass fibre using paraffin oil. Unit cell measurement and intensity data collections were done on a Bruker AXS smart single crystal diffractometer equipped with a sealed Mo tube source (λ = 0.71073 Å) APEX II CCD detector. The data collection included a correction for Lorentz and polarization effect, with an applied multi scan absorption corrections (SADABS). The crystal structures were solved and refined using the SHELXTL program suite. Direct method yielded all non-hydrogen atoms which were refined with anisotropic thermal parameters. All hydrogen atoms positions were calculated geometrically and were riding on their respective atoms.

UV-Vis absorption

Samples were measured on Agilent Cary 500 UV-Vis spectrometer in the region of 200-700 nm.

Luminescence Measurement

All emission data for solid state crystalline sample were obtained using a hyperspectral microscope equipped with an inverted optical microscope (Nikon Eclipse Ti-U), a Nikon halogen lamp (100 W) with a single band DAPI filter cube for 390 nm excitation, a broadband camera for colour imaging, a set of galvanometer mirrors, a Princeton Instruments SP-2360 monochromator/spectrograph, and a Princeton Instruments ProEM EMCCD camera for detection of the visible emission. A 400 nm long-pass filter (Thorlabs) was inserted at the emission side of the DAPI cube in order to allow for the detection of the visible emission, while cutting off the excitation wavelength. Quantum yield measurements were calculated at room temperature relative to 9,10 diphenylanthracene (DPA) in cyclohexane with the quantum yield of 0.9 using Cary Eclipse Fluorescence Spectrometer (Agilent technologies). The graph of integrated emission intensity *vs* absorption at the excitation wavelength ($\lambda_{excitation}$ = 340 nm) in different concentrations of 23.25×10^{-5}, 1.09×10^{-5}, $1.86\times 10^{-5}$and 1.16×10^{-5} M in cyclohexane for DPA, 11.2×10^{-6}, 10×10^{-6}, 7.5×10^{-6} and 6.25×10^{-6} M in acetonitrile for the Co^{II} complex and 0.018×10^{-6}, 0.012×10^{-6}, 0.0093×10^{-6} and 0.0062×10^{-6} M in acetonitrile for the Cu^{II} complex was plotted separately. The slope of each graph was used in equation 1.16 to calculate the quantum yield of the two complexes relative to the DPA.

Electrochemical Measurements

All cyclic voltammetry experiments were carried out in a three neck round bottom flask sealed with parafilm. Samples were prepared in the glove box and sealed before removing for measurement. Cyclic voltammetry was performed using a VersaSTAT 3 (Princeton Applied Research) potentiostat. A conventional three electrode system was employed. A glassy carbon electrode (diameter = 0.2 cm) was used as the working electrode, a Pt wire as the auxiliary electrode, and an Ag wire was used as pseudo-reference electrode. Tetrabutylammonium hexafluorophosphate was used as the supporting electrolyte (100 mM) and the concentration of each sample was 1 mM (in 10 mL acetonitrile). Ferrocene was used as the reference.

3.2.3 Synthesis

3.2.3.1 Synthesis of 4-(1,8-naphthalimido) benzoic acid (benzonap): The product was synthesized according to the previously reported procedure and the synthetic route is depicted in Scheme 3.2.75 A mixture of 1,8 -naphtalic anhydride (1.98 g, 10 mmol) and 2-aminobenzoic acid (1.65 g, 10 mmol) was refluxed in DMF (100 mL) overnight. The hot solution was poured into ice and cold water and the resulting precipitate was filtered, washed with ether and air-dried. Yield (98.42%, 3.12 g). ^{1}H NMR (DMSO, 400 MHz): δ (ppm) = 13.50 (s, 1H, acid), 8.54 (d, 2H, napht), 8.52 (d, 2H, napht), 8.09 (d, 2H, phen), 7.92 (t, 2H, napht), 7.55 (d, 2H, phen). IR data (ATR, cm^{-1}): 1772 (w), 1739 (w), 1701 (w), 1662 (w), 1624 (w), 1587 (w), 1511 (w), 1432 (w), 1372 (m), 1348 (m), 1305 (w), 1280 (w), 1232 (s), 1153 (w), 1100 (w), 1013 (w), 902 (w), 855 (m), 843 (m), 773 (s), 708 (m), 676 (m)

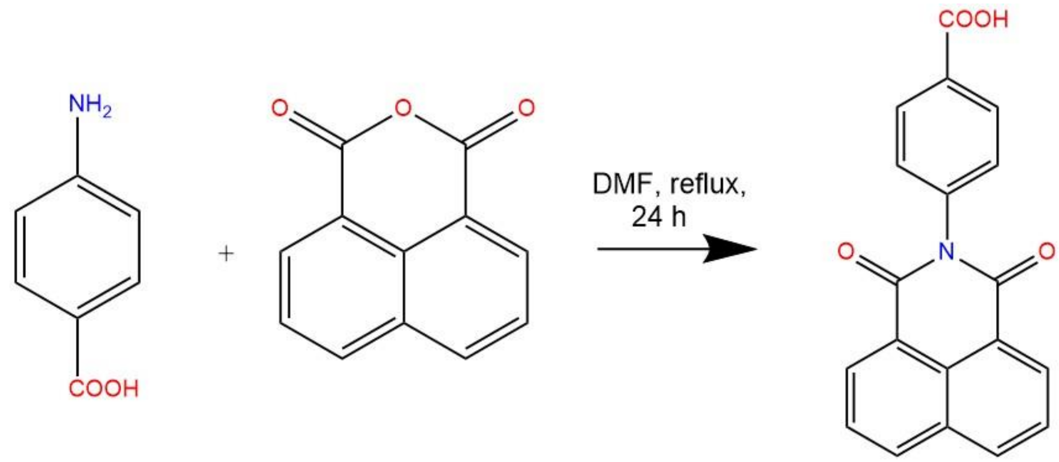

Scheme 3.2. Synthetic route for of 4-(1,8-Naphthalimido) benzoic acid (benzonap).

3.2.3.2 Synthesis of N-(2'-pyridyl)-1,8-naphthalimide (pynap): The product was synthesized according to the previously reported literature and the synthetic route is depicted in Scheme 3.3.72 In 25 mL of pyridine, (0.217 g, 1.1 mmol) of 1,8-naphthalenedicarboxylic anhydride, (0.094 g, 1.0 mmol) of 2-aminopyridine, 4 Å molecular sieves, and 120 mg of $Zn(OAc)_2$ were added. The round bottom flask was equipped with a Dean-Stark apparatus and a condenser. The reaction mixture was allowed to reflux overnight. The pyridine was removed under reduced pressure to give a white solid. The solid was then dissolved in acetone and stirred for 30 min. The solution was then filtered using standard vacuum filtration, and the solution was removed under reduced pressure to give white powder as product. Yield: (61.3%, 0.168g), ^1H NMR ($CDCl_3$, 400 MHz): δ 8.73 (d, 1H, Py), 8.64 (d, 2H, napht), 8.28 (d, 2H, napht), 7.92 (t, 1H, py), 7.79 (t, 2H, py), 7.41 (m, 2H, napht) IR data (ATR, cm^{-1}): 1735 (w), 1702 (m), 1661 (m),1624 (w), 1585 (w),1513 (w),1465 (m),1437 (m), 1375 (m), 1354 (m), 1273 (m),1190 (w), 1117 (w), 999 (w), 902 (m),846 (m), 774 (s),743 (m), 691 (w), 673 (m).

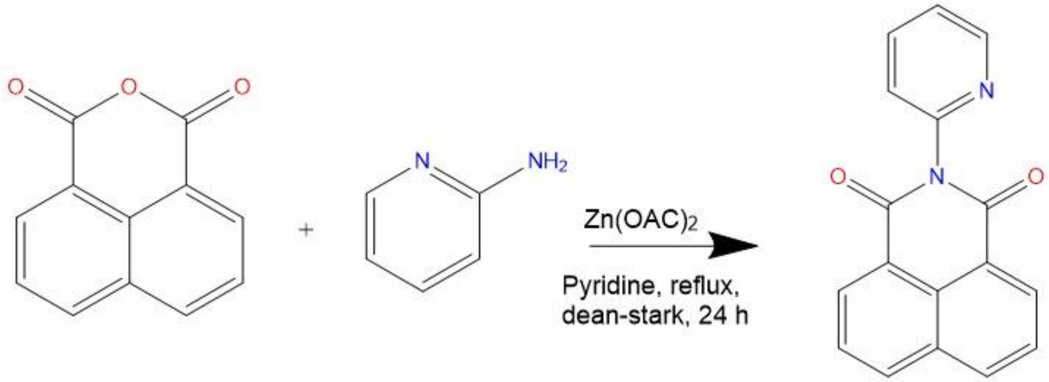

Scheme 3.3. Synthetic Route for N-(2’-pyridyl)-1,8-naphthalimide (pynap).

3.2.3.3 Synthesis of 4-(1,8-naphthalimido) dipicolinic acid (dipicnap): The precursor, 4-aminopyridine-2,6-dicarboxylic acid (H_2dipicNH$_2$) (**4**), was synthesized according to the previously reported procedure with slight modifications.77

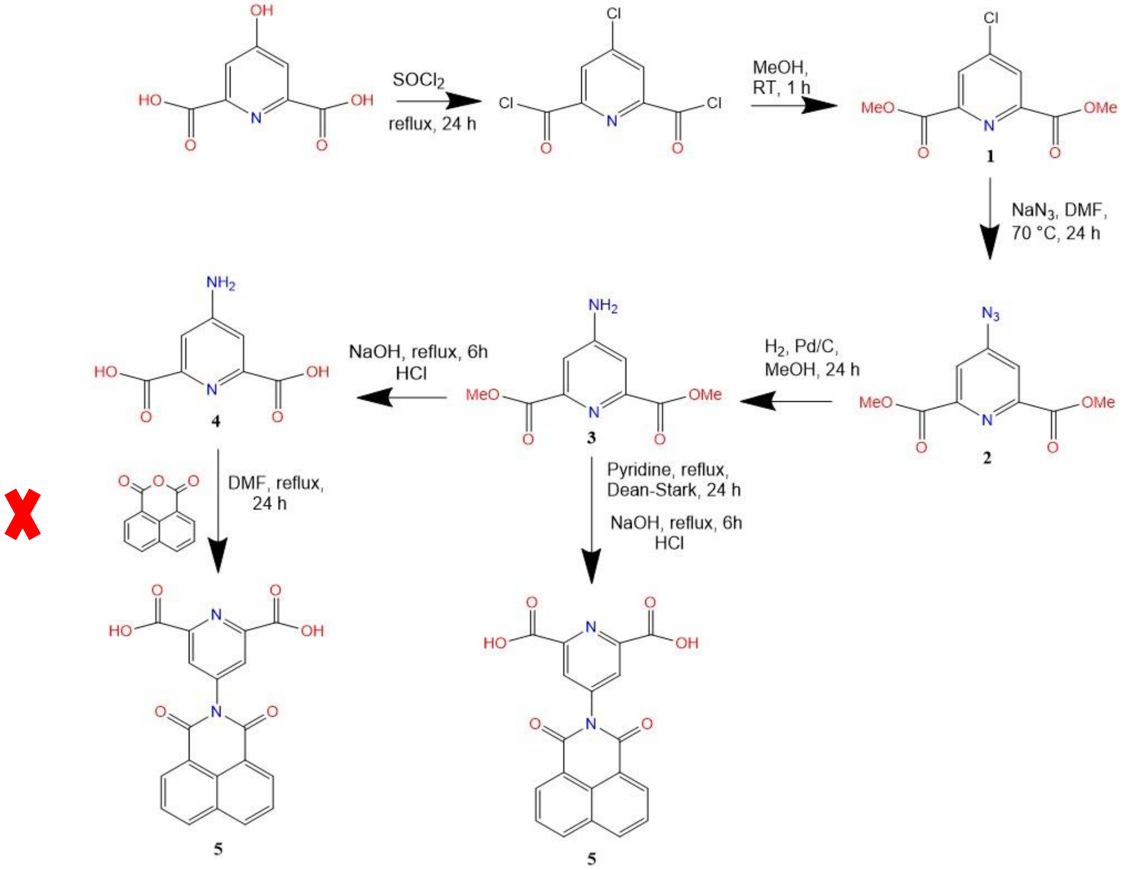

Scheme 3.4. Synthetic Route for 4-(1,8-Naphthalimido) dipicolinic acid (dipicnap).

Dimethyl-4-chloropyridine-2,6-dicarboxylate (1). A suspension of chelidamic acid monohydrate (3 g, 16.38 mmol), $SOCl_2$ (10 mL) and 1 drop of DMF was refluxed for 24 h to yield green-yellow solution. The $SOCl_2$ was removed under reduced pressure, 10 mL methanol was added, and the system was stirred for 1h at room temperature. The excess methanol was removed under reduced pressure. The residue was dissolved in chloroform, washed with water (2x) and brine (2x). The organic phases were dried over Na_2SO_4, filtered and the solvent removed under reduced pressure to give the white solid as the product. Yield: (72% 2.70 g).

Dimethyl-4-azidopyridine-2,6-dicarboxylate (2). Dimethyl-4-chloropyridine-2,6-dicarboxylate (**1**) (2 g, 8.71 mmol) was dissolved in DMF and NaN_3 (5.6 g, 87.1 mmol) was added. The resulting yellow solution was stirred at 70 °C for 24 h. A 2:1 solution of ethylacetate:hexane was added to the solution and it was washed with water (5x). The aqueous phase was re-extracted with 2:1 solution of ethylacetate:hexane (20 mL), the organic phases were dried over Na_2SO_4 and the solvent removed under reduced pressure to give a light yellow solid. Yield: (55.24%, 1g).

Dimethyl-4-aminopyridine-2,6-dicarboxylate (3). Dimethyl-4-azidopyridine-2,6-dicarboxylate (**2**) (1 g, 4.80 mmol) and 150 mg Pd/C (5%) were suspended in methanol to yield a black solution. The suspension was degassed by sparging with argon for 10 min and hydrogenated at 50 psi at room temperature overnight in a Parr reactor. The intermediate was used for the next step without further purification.

4-aminopyridine-2,6-dicarboxylic acid - H_2dipicNH$_2$ (4). 2.5 M (4 mL) NaOH was added to a suspension of (**3**) and the mixture was refluxed for 6 h and allowed to cool to room temperature**.** The suspension was filtered, and the pH was adjusted to 2 via HCl (10%). The solid was filtered and washed with cold water to yield white solid. Yield: (11.49%, 0.1 g).

4-(1,8-Naphthalimido) dipicolinic acid (dipicnap): Two different methods were designed to synthesize the final product (dipicnap) as described below.

1. A mixture of 1,8 -naphthalic anhydride (107.62 mg, 0.54 mmol) and (**4**) (100 mg, 0.54 mmol) was refluxed in DMF (30 mL) overnight. The hot solution was poured into ice and cold water and the resulting precipitate was filtered and air-dried. NMR spectroscopy indicated the starting material peaks: ^{1}H NMR (DMSO, 400 MHz): δ (ppm) = 8.45 (d, 4H, napht), 7.92 (t, 2H, napht), 7.34 (s, 2H, Py), 7.06 (br, 2H, NH_2) which indicates the reaction does not occur using this method.

2.**Synthesis of 4-(1,8-naphthalimido) dimethoxydipicolinato:** In 25 mL of pyridine, (118.90 mg, 0.6 mmol) of 1,8-naphthalenedicarboxylic anhydride, (126.11, 0.6 mmol) of (**3**), 4 Å molecular sieves, and 60 mg of $Zn(OAc)_2$ were added. The round bottom flask was equipped with a Dean-Stark apparatus and a condenser. The reaction mixture was allowed to reflux overnight. The pyridine was removed under reduced pressure and the solid was then dissolved in acetone and stirred for 30 min. The solution was then filtered and evaporated under reduced pressure. The product was purified by column chromatography to give 10 mg of white powder. Yield: 4.26%, ^{1}H NMR (DMSO, 400 MHz): δ (ppm) = 8.50 (m, 4H, napht), 8.08 (d, 2H, napht), 7.94 (s, 6H, CH_3), 7.54 (d, 2H, Py).

4-(1,8-Naphthalimido) dipicolinic acid (dipicnap): Because of the low yield of the previous steps, this step has not been performed and the final ligand has not been synthesized. Generally this step should contain the addition of NaOH and then control the pH up to 2 by HCl 2% to get the final product.

3.2.3.4 Efforts to Synthesize metal complexes with (Benzonap) ligand: A solution of Benzonap (79.32, 0.25 mmol) in MeCN (10 mL) with triethylamine (TEA) (34.83 µL, 0.25 mmol) was added to a solution of $Eu(NO_3)_3.6H_2O$ (115.51 mg, 0.25 mmol in MeOH (5 mL). The reaction mixture was allowed to stir for 5 minutes and filtered. The filtrate was placed in diethyl ether and hexane baths separately to assist crystallization at room temperature. Aggregated microcrystals formed after few days which was not suitable for X-ray crystallography. A set of analogous reactions were carried out using, $Yb(NO_3)_3.5H_2O$ (112.25 mg, 0.25 mmol), $DyCl_3$ anhydrous (67.21 mg, 0.25 mmol), $LaCl_3$ anhydrous (61.31 mg, 0.25 mmol),

$LuCl_3$ anhydrous (70.33 mg, 0.25 mmol), $Eu(OAC)_3$.hydrate (82.27 mg, 0.25 mmol) and $Tm(NO_3)$.$6H_2O$ (115.76 mg, 0,25 mmol) as well as two transition metal salts anhydrous $CuBr_2$ (55.84 mg, 0.25 mmol) and anhydrous $Zn(OAC)_2$ (45.87 mg, 0.25 mmol) as starting materials and the result was similar to the first reaction. Additionally, similar reactions in different ratios (ligand:metal): (0.5:0.5, 0.5:0.25, 0.75:0.25) with different solvents for the ligand including dichloromethane (DCM), tetrahydrofuran (THF), MeOH and EtOH in controlled pH with NaOH or TEA has been done overnight with or without reflux and put in the hexane, pentane and ether diffusion separately to assist crystallization, however they all gave the aggregated microcrystalline material which was not suitable for X-ray diffraction.

Solvothermal reactions using two ratios of $Eu(NO_3)_3$.$6H_2O$, benzonap ligand and base (TEA) (1:1:1) and (1:2:2) in water and MeOH were performed. After overnight reaction, the solution was filtered and divided into two portions. One portion was used in diethyl ether diffusion system to assist crystallization and the second portion was put to evaporate slowly to give crystals. No crystal suitable for X-ray diffraction was obtained after several days. A set of analogous reactions were carried out using, $Yb(NO_3)_3$.$5H_2O$ (112.25 mg, 0.25 mmol), $DyCl_3$ anhydrous (67.21 mg, 0.25 mmol), $LaCl_3$ anhydrous (61.31 mg, 0.25 mmol), $LuCl_3$ anhydrous (70.33 mg, 0.25 mmol), $Eu(OAC)_3$.hydrate (82.27 mg, 0.25 mmol) and $Tm(NO_3)$.$6H_2O$ (115.76 mg, 0.25 mmol) as well as two transition metal salts anhydrous $CuBr_2$ (55.84 mg, 0.25 mmol) and anhydrous $Zn(OAC)_2$ (45.87 mg, 0.25 mmol) as starting materials and the results were similar.

Liquid-Liquid Diffusion method[80]: Benzonap (79.32 mg, 0.25 mmol) was added to 2 mL dimethylsulfoxide (DMSO) and then 10 mL of dichloromethane (DCM) were added. $Eu(NO_3)_3$.$6H_2O$ (111.5 mg, 0.25 mmol) was dissolved in MeOH (10 mL). Each solution was divided into three test tubes (DCM solution added first) with a buffer layer of pure MeOH between two solutions. The test tubes were stored undisturbed at room temperature. After few days aggregated microcrystals that were not suitable for X-ray diffraction formed. Again, analogous reactions were carried out using, $Yb(NO_3)_3$.$5H_2O$ (112.25 mg, 0.25 mmol), $DyCl_3$ anhydrous (67.21 mg, 0.25 mmol), $LaCl_3$ anhydrous (61.31 mg, 0.25 mmol), $LuCl_3$ anhydrous (70.33 mg, 0.25 mmol), Eu(OAC)$_3$.hydrate (82.27 mg, 0.25 mmol) and Tm(NO$_3$).6H$_2$O (115.76 mg, 0,25 mmol) as starting materials and the results did not change.

A solution of Benzonap (118.98 mg, 0.375 mmol) and Sm_2O_3 (43.59 mg, 0.125 mmol) was suspended in water and the suspension was heated up to 100 ˚C for 1 hour, then the pH was adjusted to 6 with Na_2CO_3. The solution was stirred for an hour again, filtered and put for slow evaporation.77 No crystal was obtained using this method.

3.2.3.5 Synthesis of [Co^{II}Cl$_2$(Pynap)$_2$] (i): A solution of Pynap (68.6 mg, 0.25 mmol) in MeCN (10 mL) was added to a solution of anhydrous $CoCl_2$ (16.2 mg, 0.125 mmol) in MeCN (10 mL) the resulting blue solution was stirred for 5 minutes, filtered and put in ether bath to assist crystallization. X-ray quality blue crystals were recovered after two days. Crystals were collected by vacuum filtration and washed with ether. Yield: (23.58%, 20 mg), IR data (ATR, cm^{-1}): 3049 (w), 1702 (m), 1647 (m), 1585 (m), 1477 (m), 1437 (m), 1374 (m), 1347 (m), 1311 (w), 1235 (m), 1180 (m), 1154 (w), 1100 (m), 1019 (w), 984.(w), 848 (m), 836 (m), 776 (s), 748 (w), 737 (m), 694 (m), 627 (m). Elemental Analysis calculated (found)%: N: 8.05 (8.18), C: 58.64 (58.87), H: 3.18 (2.86).

3.2.3.6 Synthesis of [Cu^{II}Br$_2$(Pynap)$_2$] (ii): A solution of Pynap (68.6 mg, 0.25 mmol) in MeCN (10 mL) was added to a solution of anhydrous $CuBr_2$ (27.91 mg, 0.125 mmol) in MeCN (10 mL) the resulting green solution was stirred for 5 minutes, filtered and put in ether bath to assist crystallization. X-ray quality green crystals were recovered after few days. Crystals were collected by vacuum filtration and washed with ether. Yield: (19.27%, 18.64 mg) IR data (ATR, cm^{-1}): 3074 (w), 1700 (s), 1654 (s), 1625 (w), 1584 (m), 1476 (w), 1372 (m), 1345 (m), 1305 (w), 1270 (w), 1234 (s), 1197 (w), 1179 (w), 1153 (w), 1101 (m), 1028 (m), 994 (w), 901 (s), 886 (m),846.102 (s), 835 (s), 775 (s), 749 (w), 692 (m), 672 (m). Elemental Analysis calculated (found)%: N: 5.95 (6.35), 43.35 (43.46), 3.21 (2.61).

Table 3.1 Crystallographic data for complexes (i) and (ii).

Empirical formula	$C_{34}H_{20}Cl_2CoN_4O_4$ **(i)**	$C_{34}H_{20}Br_2CuN_4O_4$ **(ii)**
Formula weight	678.37	771.90
Temperature	200(2) K	200(2) K
Wavelength (Å)	0.71073	0.71073
Crystal system	Orthorhombic	Monoclinic
Space group	P b c n	$P\ 2_1/c$
a (Å)	14.563(2)	12.7178(4)
α (◦)	90	90
b (Å)	7.6989(11)	13.6319(4)
β (◦)	90	102.662(2
C (Å)	24.560(4)	7.9745(3)
γ (◦)	90	90
Volume ($Å^3$)	2753.6(7)	1348.90(8)
Z	4	2
Density (Mg/m^3)	1.636	1.900
Absorption coefficient (mm^{-1})	0.868	3.824
F(000)	1380	766
Theta range for data collection (°)	1.658 to 28.435	1.641 to 27.565
Reflections collected	27352	13590
Independent reflections	3461 [R(int) = 0.0655]	3118 [R(int) = 0.0500]
Completeness to theta = 25.242° (%)	100.0	100.0
Refinement method	Full-matrix least-squares on F^2	Full-matrix least-squares on F^2
Goodness-of-fit on F^2	1.044	1.019
Final R indices [I>2sigma(I)] R_1, wR_2	0.0500, 0.1060	0.0352, 0.0622
R indices (all data) R_1, wR_2	0.0713, 0.1157	0.0566, 0.0676

3.3 Crystal Structures

3.3.1 Efforts to prepare lanthanide complexes of benzonap: As described in the experimental section, efforts to make both transition and lanthanide metal complexes have been unsuccessful. Although some materials were obtained that appeared to be crystalline, these solids were too small to provide adequate diffraction for analysis. In the experiments that were done with nitrate salts, the nitrate starting materials were crystallized. In other samples, crystal structures obtained from the reaction mixtures were the dissociated form of the ligand in the reactions where NaOH was used as base to deprotonate the benzoic acid. In the case of $DyCl_3$ the preliminary structure obtained was a cluster of Dy atoms. This benzonap compound has been previously exploited for synthesizing supramolecular structures due to its π-π stacking capabilities of the strongly π-deficient naphthalimide moiety as well as the ability of carboxylic acid to deprotonate and form complexes and through their self-assembly via hydrogen bonding interactions. Hydrogen bonding is described as the masterkey interactions in supramolecular chemistry.80[,81] According to these strong interactions (strong on the intermolecular interaction scale), it is expected that the possibility of π-π stacking and hydrogen bonding within the ligand structures dominated to give polymer structures rather than metal complexes.

3.3.2 Crystal structure of $[Co^{II}Cl_2(Pynap)_2]$ (i): Complex (**i**) crystallized in the orthorhombic P b c n space group. The asymmetric unit is half a molecule and there is a two-fold rotation axis bisecting the Cl-Co-Cl angle and passing through the metal center. A representation of the crystal structure is shown in figure 3.3. The complex is neutral and the octahedral coordination geometry around the metal is distorted. The metal is coordinated by two cis positioned oxygens, two trans positioned nitrogens and two cis positioned chlorine atoms. Distortion from octahedral geometry can be seen from the values of the N2-Co-N2 and O1-Co-Cl1 angles 157.54(12)°and 164.37(5)°(ideally 180°) respectively. Additionally, the bite angle N2-Co-O1 is 76.30(7)°(ideally 90°) shows the distortion. The bond distances N2-Co 2.116(2), O1-Co 2.304(2) and Cl1-Co 2.367(2) are in agreement with the previously reported octahedral Co complex with same coordination atoms.[82] Selected bond distances and angles are indicated in table 3.2 As a measure of planarity of the ligand the angle between the plane of the pyridine and the plane of the naphthalimide group (C11, N1, C1) was measured. The angle was 51.79° showing not complete orthogonality and not complete co-planarity and there could be some π conjugation.

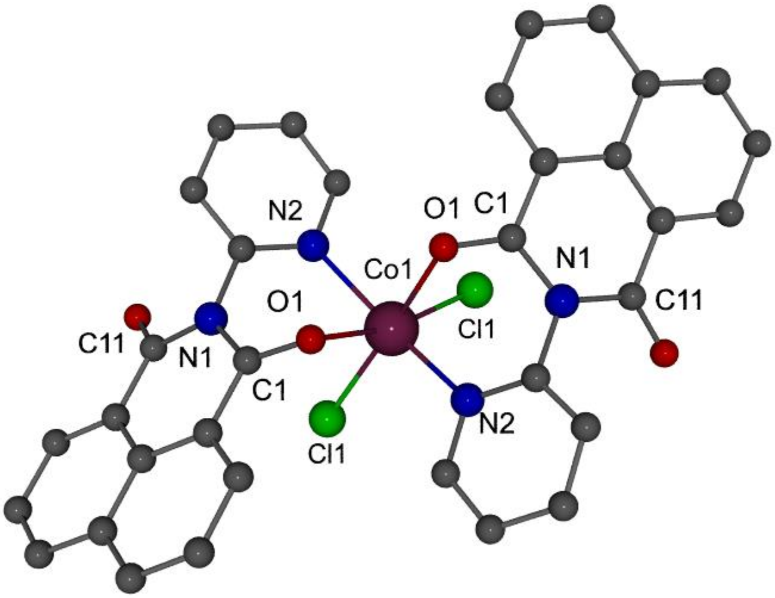

Figure 3.3. Representation of the crystal structure of [Co^{II}Cl$_2$(Pynap)$_2$] (i). Color code: grey: (C), blue: (N), green: (Cl), red: (O), Purple: (Co), hydrogen atoms are removed for clarity.

3.3.3 Crystal structure of [Cu^{II}Br$_2$(Pynap)$_2$] (ii): Complex (**ii**) crystallized in the monoclinic P2$_1$/c space group and the crystal structure representation is shown in Figure 3.4. In this symmetric complex, the Cu^{II} coordination environment consists of two nitrogen atoms from pyridine (N2), two oxygen atoms from naphthalimide moiety (O2) and two bromides (Br1) are coordinated to the Cu^{II} ion in trans positions and the coordination geometry is an axially elongated distorted octahedral environment. The two pyridyl nitrogen atoms and two carbonyl groups from naphthalimide are in the equatorial plane and two bromide anions at the axial positions (Cu^{II}-Br = 2.4739(3)Å). According to the d^9 electronic configuration in octahedral geometry and the negligible Jahn-teller effect this distortion can be well explained. Additionally, the distortion of the axially elongated octahedron is due to the small bite angle N2-Cu-O1 of the O, N chelating ligand which is 78.61(7)°. Selected bond distances and angles are shown in table 3.2. The bond distances N2-Cu 2.002(2), O1-Cu 2.5393(2) and Br-Cu 2.4739(3) are larger than the previously reported octahedral geometry in Cu^{II} complex with O-Cu 1.956(2), N-Cu 1.984(4) and F-Cu 2.468(4) bond distances.[83] In this species the angle between the plane of pyridine ring and the plane of the naphthalimide group (C12, N1 and C2) was measured to be 62.42°which depicts not complete co-planarity and non-complete orthogonality of the structure.

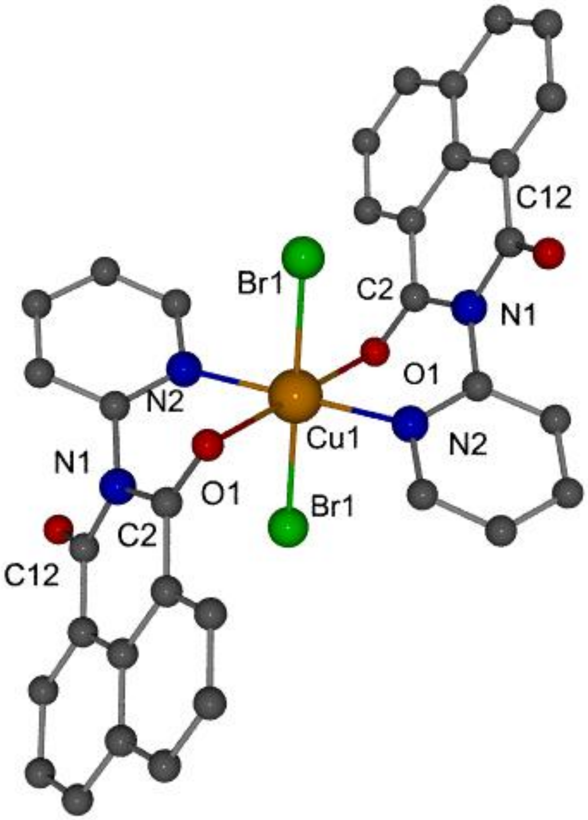

Figure 3.4. A representation of the crystal structure of [$Cu^{II}Br_2(Pynap)_2$] (ii). Color code: grey: (C), blue: (N), green: (Cl), red: (O), orange:(Cu), hydrogen atoms are removed for clarity.

Table 3.2. Selected bond distances and angles for complexes (i) and (ii). X indicates halides (Cl and Br).

O(1)-M(1) (Å)	2.304(2)	2.5293(2)
X(1)-M(1) (Å)	2.3674(2)	2.4739(3)
M(1)-N(2) (Å)	2.116(2)	2.002(2)

O(1)-M(1)-X(1) (◦)	164.37(5)	93.20(47)
N(2)1-M(1)-X(1) (◦)	97.94(6)	91.18(7)
N(2)-M(1)-N(2) (◦)	157.55(12)	180
X(1)-M(1)-X(1) (◦)	104.22(4)	180
N(2)-M(1)-O(1) (◦)	76.30 (7)	78.61(7)
O(1)-M(1)-O(1) (◦)	74.32(10)	179.992

3.4 Optical Measurements

3.4.1 Absorption spectra of Pynap, (i) and (ii): The absorption spectra of the Pynap ligand, and the metal complexes (**i**) and (**ii**) were recorded in acetonitrile in the range of 200-800 nm and are depicted in figure 3.5. The spectrum of the ligand showed several bands at higher energies (lower wavelengths) at 214, 232, 335 and 350 nm which were in agreement with the previously reported N-Aryl substituted 1,8 naphthalimide compounds. The absorption at 214 to 335 nm was assigned to the n→π* transition from HOMO-1 to LUMO which is localized on the pyridine ring to naphthalene moiety, respectively. The absorption at 350 nm was assigned to the π→π* transition from HOMO to LUMO which is localized on the carbonyl groups of the naphthaimide moiety.73 The electronic spectra of the Co^{II} and Cu^{II} complexes displayed two additional absorptions in addition of the transitions associated with the ligand. The appearance of the ligand centered transitions suggests that little structural alteration of the ligand occurred during complexation. The peak at 270 nm was attributed to the ligand to metal charge transfer in Cu^{II} complex and a shoulder at 296 and 319 nm is attributed to the ligand to metal charge transfer (LMCT) in Co^{II} complex. The weak absorption band at 600-700 for both complexes is attributed to the d-d transitions. In the case of Co^{II} complex (**i**), a broad peak appears at 686 nm while for the Cu^{II} complex (**ii**) this absorption is centered at 634 nm. The low intensity for these absorptions is consistent with Laporte forbidden d-d transitions as discussed below. The molar absorption coefficient increased from ligand (851.64 $cm^{-1}mol^{-1}L$) to 155,000 $cm^{-1}mol^{-1}L$ and 29,200 $cm^{-1}mol^{-1}L$ for the Co^{II} and Cu^{II} respectively.

Complex (**i**) is high-spin (μ_{eff}= 4.8). In a high-spin octahedral crystal field of Co^{II} ion, the ^4F lowest free ion state splits into two triplet states ($^4T_{1g}$ and $^4T_{2g}$) and one singlet state ($^4A_{2g}$) while ^4P does not split ($^4T_{1g}$). The transitions from $^4T_{1g}$ to $^4T_{2g}$, $^4T_{1g}$(F) to $^4T_{1g}$(P) and $^4T_{1g}$ to $^4A_{2g}$ lead to the formation of the broad absorption peak in the visible and near-IR regions.[84] Observing the Co^{II} complex absorption spectra indicates similar behaviour. Therefore, the peaks at 570-685 nm originate from $^4T_{1g}(F) \rightarrow {}^4T_{1g}(P)$ and $^4T_{1g} \rightarrow {}^4A_{2g}$ in the visible region. A number of weak bands observed in this area may be attributed to the spin-forbidden quartet to doublet transitions.

According to Lever[85], since the ground state in the octahedral geometry is distorted for example due to the Jahn-Teller effect, spin-orbit coupling and vibrational coupling, regular octahedral Cu^{II} complex cannot exist. For instance, the t_{2g}-e_g separation in a regular octahedral Cu^{II} varies from 770 to 550 nm for CuO_6 and CuN_6 respectively. Therefore, in the case of distorted octahedral geometry several absorption bands may be expected which correspond to transition of components of t_{2g} to $d_{x^2-y^2}$. The d-d transitions for Cu^{II} complex can be assigned to the $^2T_{2g} \rightarrow {}^2E_g$ octahedral geometry. However, in the cases where the ^2E_g and $^2T_{2g}$ of the octahedral Cu^{II} split, three transitions $^2B_{1g} \rightarrow {}^2E_g$, $^2B_{1g} \rightarrow {}^2B_{2g}$ and $^2B_{1g} \rightarrow {}^2A_{1g}$ for Cu^{II} are expected. Their very close energies could have made them appear as one broad band.

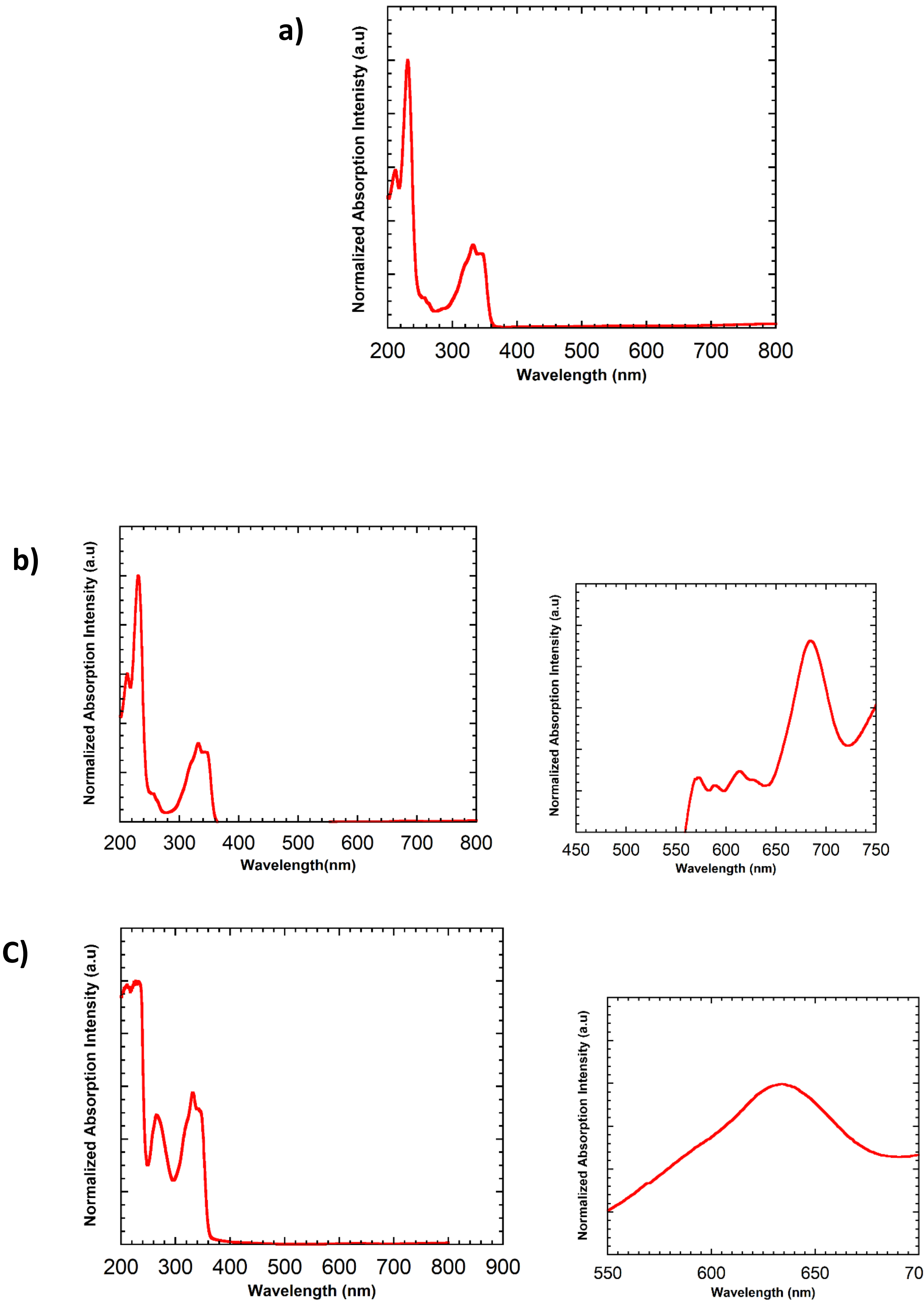

Figure 3.5. Normalized absorption spectra of Pynap (3.64×10^{-4} M) (a), complex (i) (2×10^{-6} M) (b) and complex (ii) (19.4×10^{-6} M) (c) all in MeCN, d-d transitions in both b and c are shown separately.

3.4.2 Emission Spectra of (i) and (ii): The emission spectra for complexes (**i**) and (**ii**) were monitored in solid form at room temperature between 350-850 nm using the hyperepectral microscope. The microscope was fitted with a single band DAPI filter cube for 390 nm excitation. The spectra are depicted in figure 3.6. Both the Co^{II} and Cu^{II} complexes displayed emission in the visible region at 498.95 and 443.37 nm which corresponds to the greenish blue and blue color with the quantum yield of 0.05 and 0.08 for Co^{II} and Cu^{II} complexes respectively. The ligand emission is at 378 nm with quantum yield of 0.004.72 Hence, the complexation of the ligand with Co^{II} and Cu^{II} ions causes a red shift in emission spectra and enhances the emission efficiency (based on quantum yield comparison) which is in agreement with our goal to synthesize metal complexes indicating emission in the visible region for different purposes.

As the absorption maximum (excitation wavelength) is 340 nm for Co^{II} and Cu^{II} complexes and the emission maxima lie at 498 and 443 nm for Co^{II} and Cu^{II} complexes respectively, there are relatively large Stokes shifts of approximately 158 nm for Co^{II} and 103 nm for Cu^{II} complexes. Displaying a large Stoke shift is one of the desirable photophysical properties of transition metal complexes as it minimizes self-quenching and homo-fluorescence resonance energy transfer. It is most likely that the visible emission which is observed in both complexes is phosphorescence and it is produced from triplet excited state. This can be due to the spin-orbit coupling in d^7 and d^9 electronic configurations which facilities the fast conversion of singlet to triplet excited state via intersystem crossing mechanism.[86]

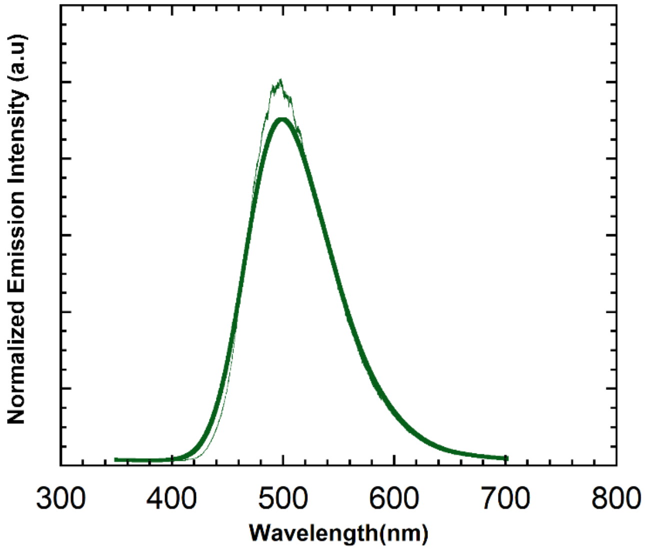

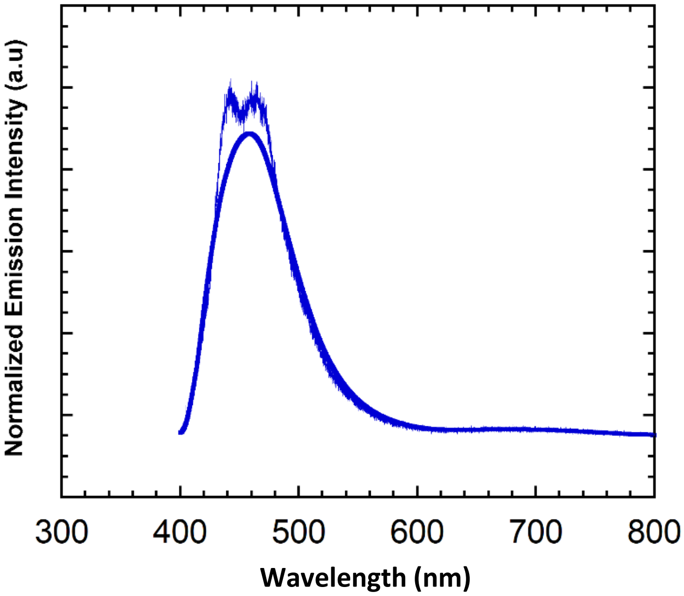

Figure 3.6. Normalized solid state photoluminescence emission of complex (i) (top) and complex (ii) bottom. The smooth line is shown for clarity.

3.5 Electrochemical properties of Pynap, (i) and (ii):

As the radical anions of most aromatic imides and diimides are proper chromophores with intense and characteristic visible and near-IR absorption bands74, the electrochemical properties of Pynap ligand and complexes (**i**) and (**ii**) were monitored by cyclic voltammetry technique**.** Cyclic voltammogram (CV) of compounds Pynap, (**i**) and (**ii**) were examined in dry acetonitrile (1 mM of Pynap, (**i**), (**ii**) and 100 mM (n-Bu)$_4$NPF$_6$ as electrolyte) using a glassy carbon working electrode, Pt counter electrode and Ag wire pseudo-reference electrode. Cyclic voltammetry was carried out under nitrogen and referenced to the ferrocene/ferrocenium (Fc/Fc$^+$) couple. The cyclic voltammograms obtained under these conditions are shown in Figure 3.7 and 3.8. The CV scans for all three compounds showed one quasi-reversible and one reversible well separated one electron reduction wave. As shown in Figure 3.7 the half-wave reduction potential for radical anion and dianion of Pynap are -1.73 and -2.44 V which is in agreement with the previously reported literature.[87,88,89] TD-DFT calculations approved the naphthalimide based redox activity with no contribution of the pyridine ring which is in agreement with the Baruah group's research on different substituents of N-Aryl 1,8 naphthalimide compounds.[90]

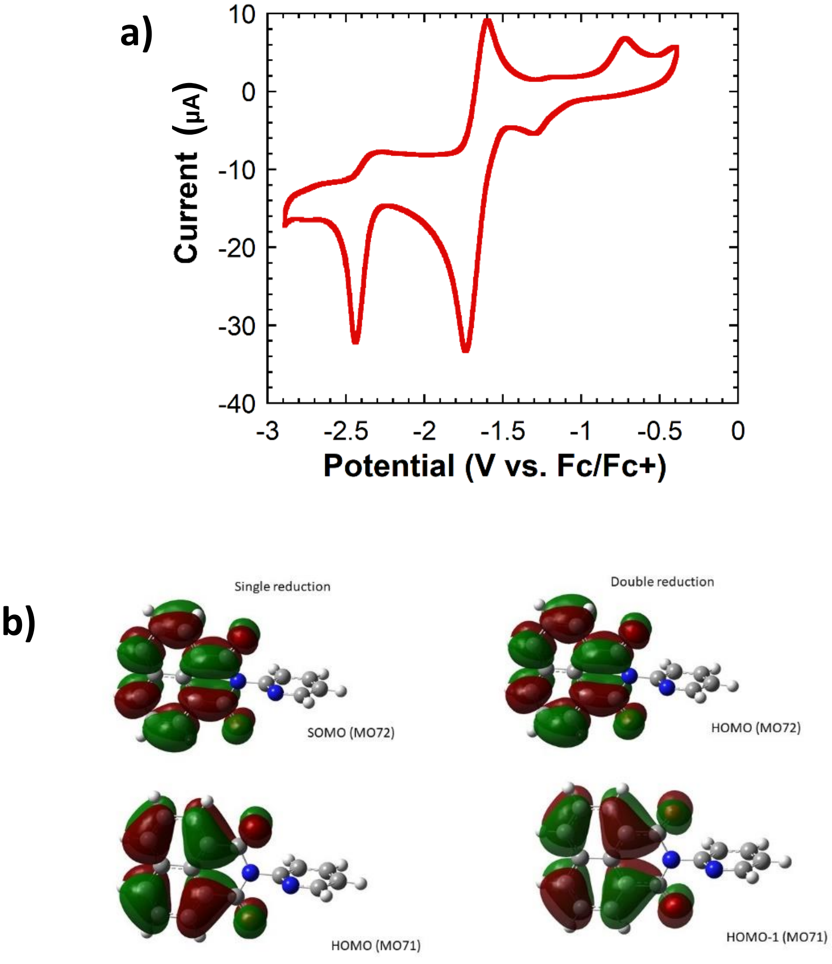

Figure 3.7. Cyclic voltagram of Pynap ($E^{-}_{1/2}$ = -1.73 and $E^{2-}_{1/2}$ = -2.44 V *vs.* Fc/Fc$^+$) in dry MeCN (1 Mm) using NBu$_4$PF$_6$ as a supporting electrolyte (100 mM) (a) and Frontier molecular orbitals from DFT calculations (B3LYP/def2TZVP)(b).

The coordination of Pynap to the Co^{II} and Cu^{II} metal centers results in an anodic shift for both reduction events and increases the value of half-wave reduction potential for radical anion and dianion for complex (**i**) to -1.51, -2.26 V and for complex (**ii**) to -1.56, -2.31 V. Clearly, these two new metal complexes are redox-active. The redox activity of these complexes will throw light on the implications on supramolecular properties and their further applications in electrochemical probes.

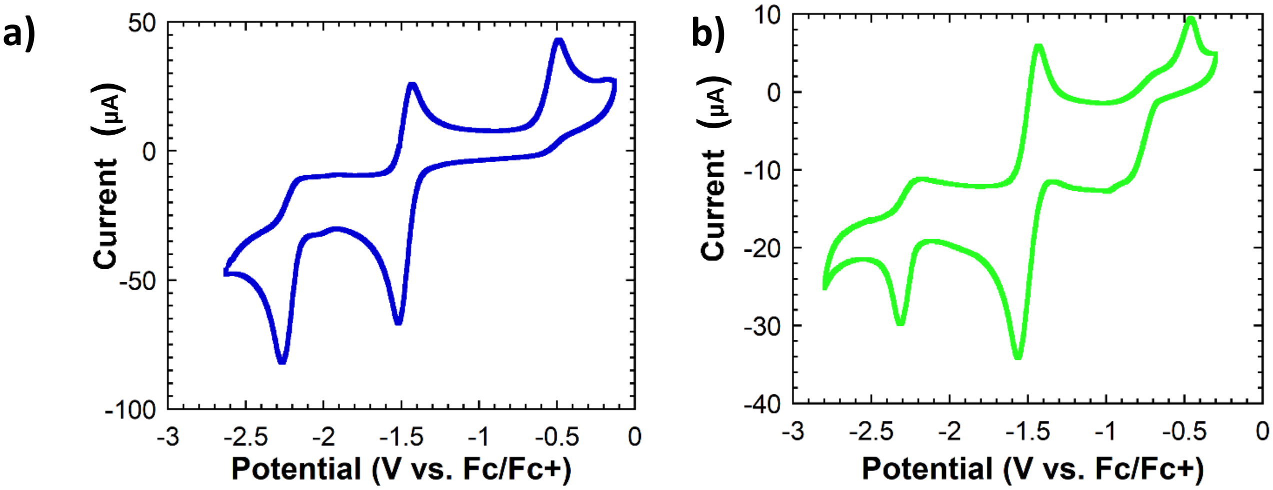

Figure 3.8. Cyclic voltagram of (i) ($E^{-}_{1/2}$ = -1.51 and $E^{2-}_{1/2}$ = -2.26 V vs. Fc/Fc^{+}) (a) and (ii) ($E^{-}_{1/2}$ = -1.56 and $E^{2-}_{1/2}$ = -2.31 V vs. Fc/Fc^{+}) (b) in dry MeCN (1 Mm) using NBu_4PF_6 as a supporting electrolyte (100 mM).

3.6 Conclusion

Two naphthalimide based ligands, one incorporating a benzoic acid group and the other a pyridine ring within their structure were synthesized and one new ligand comprised of naphtahlimide and dipicolinic acid has been proposed. Many efforts on getting crystal structures with lanthanide and transition metals with the benzonap ligand as well as some efforts to get lanthanide complexes with the pynap ligand were explored which were not successful. This may be due to the domination of π-π stacking interactions of naphthalimide moiety or self-assembly of the rings thorough hydrogen bonding via carboxylic acid group.

Two novel Co^{II} and Cu^{II} complexes with pynap ligand have been synthesized and structurally characterized. Both of these complexes provided visible light emission with higher quantum yield than their corresponding ligand and both of them showed similar redox activity to their ligand which might show higher emission intensities and extinction coefficients and or additional bands in visible or NIR region.

3.7 Outlook

The future work will be mainly focused on an improved synthesis of the proposed ligand dipicnap which was a combination of both optically active components naphthalimide and dipicolinic acid and complexation of the ligand with different lanthanide and transition metal ions to observe their emission and even their cytotoxicity properties. Additionally, the redox behaviour of the pynap ligand leads us to reduce the (**i**) and (**ii**) complexes and explore their absorption and emission properties in order to achieve higher quantum yield and or new band in the visible and NIR window. Meanwhile, there is a scope for Cu^{II} complex (**ii**) to consider as an efficient fluorescence sensor in living cells via its reduction properties and for Co^{II} complex (**i**) to detect chemical targets in living cells by magnetic resonance.[91,92] Hence, in order to take advantages of these properties, the toxicity and solubility of the complexes in biological solvents and pH should be taken into consideration.

4. Contributions to Knowledge

- The ligand design both tetrazine and naphthalimide based as well as the investigations into luminescence properties of $[\mathrm{Yb^{III}Cl_2(Htzpy)_2}]\mathrm{Cl}$, $[\mathrm{Co^{II}Cl_2(Pynap)_2}]$ and $[\mathrm{Cu^{II}Br_2(Pynap)_2}]$ complexes was presented in poster format at 101st Canadian Chemistry Conference and Exhibition (CSC 2018) in Edmonton, AB.
- The rational design for the tetrazine based ligand (Htzpy), its contributions into magnetic and luminescent properties of trivalent lanthanide ions and investigations into crystal structures, magnetic and luminescent properties of $[\mathrm{Tb^{III}Cl_2(Htzpy)_2(MeOH)}]\mathrm{Cl}$, $[\mathrm{Dy^{III}Cl_2(Htzpy)_2(MeOH)}]\mathrm{Cl}$, $[\mathrm{Ho^{III}Cl_2(Htzpy)_2(MeOH)}]\mathrm{Cl}$, $[\mathrm{Er^{III}Cl_2(Htzpy)_2(MeOH)}]\mathrm{Cl}$ and $[\mathrm{Yb^{III}Cl_2(Htzpy)_2}]\mathrm{Cl}$ complexes are currently being organized for publication.
- The crystal structures and photophysical properties of $[\mathrm{Co^{II}Cl_2(Pynap)_2}]$ and $[\mathrm{Cu^{II}Br_2(Pynap)_2}]$ are being organized for future publication.

5. References

(1) Wang, W. M.; Shi, X. H.; Zhang, H. X.; Wu, M. M.; He, Y. L.; Fang, M.; Shi, Y.; Fang, M. *Polyhedron* **2018**, *141*, 304.

(2) Ma, D. L.; Ma, V. P. Y.; Chan, D. S. H.; Leung, K. H.; He, H. Z.; Leung, C. H. *Coord. Chem. Rev.* **2012**, *256* (23–24), 3087.

(3) Ahmadi, R. A.; Hasanvand, F.; Bruno, G.; Rudbari, H. A.; Amani, S. *Russ. J. Coord. Chem.* **2013**, *39* (12), 867.

(4) Song, F.; Zhang, Y.; Chen, J.; Han, T.; Cheng, P. *J. Rare Earths* **2017**, *35* (1), 24.

(5) Ishikawa, N.; Sugita, M.; Ishikawa, T.; Koshihara, S. Y.; Kaizu, Y. *J. Am. Chem. Soc.* **2003**, *125* (29), 8694.

(6) D'Aléo, A.; Picot, A.; Beeby, A.; Williams, J. A. G.; Leguennic, B.; Andraud, C.; Maury, O. *Inorg. Chem.* **2008**, *47* (22), 10258.

(7) Kahn, O. *Molecular Magnetism*; *Journal of Chemical Education*, 1995; Vol. 72.

(8) Boˇ, R. *Coord. Chem. Rev.* **2004**, *248*, 757.

(9) Woodruff, D. N.; Winpenny, R. E. P.; Lay, R. A. *Am. Chem. Soc.* **2013**.

(10) S.; Gatteschi, D.; Sessoli, R. *Angew. Chem. Int. Ed.* **2003**, 43(3), 268.

(11) Ritter, S, K. *Chem. Eng. News* **2004**, 29.

(12) Sessoli, R.; Tsai, H. L,; Schake, A. R.; Wang, S.; Vincent, J B.; Folting, K.; gGatteschi, D.; Christou, G.; Hendrickson, D, N. *J. Am. Chem. Soc.,* **1993**, *115*, 1804.

(13) R. Sessoli. D. Gatteschi, A. Caneschi, M, A, N. *Lett. To Nat.* **1992**, *365*, 141.

(14) Huang, C.; Bian, Z. *Rare Earth Coordination Chemistry: Fundamentals and Applications Edited*; 2010.

(15) Ishikawa, N.; Sugita, M.; Wernsdorfer, W. *Angew. Chem. Int. Ed.* **2005**, *44* (19), 2931.

(16) Pointillart, F.; Jung, J.; Berraud-pache, R.; Guennic, B. Le; Dorcet, V.; Cador, O.; Maury, O.; Guyot, Y.; Decurtins, S.; Liu, S. *Inorg. Chem.* **2015**, *54* (Scheme 1), 5384.

(17) Baldovi, J. J.; Cardona-serra, S.; Clemente-juan, J. M.; Coronado, E.; Gaita-arino, A.; Palii, A. *Inorg. Chem.* **2012**, *51*, 12565.

(18) Lakowicz, J. R. *Principles of Fluorescence Spectroscopy Principles of Fluorescence Spectroscopy*; Springer: New York, 2010.

(19) Binnemans, K. *Am. Chem. Soc.* **2009**, *209*, 4283.

(20) Williams, A. T. R.; Winfield, S. A.; Miller, J. N. *Analyst* **1983**, *108*, 1067.

(21) S. Dhami, A. J. De Mello, G. Rumbles, S. M. Bishop, D. P. and A. B. J. *Am. Chem. Soc.* **1995**, *61* (4), 341.

(22) A Guide to Recording Fluorescence Quantum Yields – Horiba, http://www.horiba.com.fileadmin/uploads/Scientifics/Documents/Flourescence/ quantumyieldstrad.pdf).

(23) Reber, K. P.; Tilley, S. D.; Sorensen, E. J. *ChemInform*, **2010**, 41 (7).

(24) Weissman, S. I. *J. Chem. Phys.* **1969**, *214* (1942).

(25) Whan, R. E.; Crossby, G. A. *J. Mol. Spectrosc.* **1962**, 8, 315.

(26) Crosby, G. A.; Whan, R. E.; Alire, R. M. *J. Chem. Phys.* **1969**, *34* (1961), 743.

(27) Filipescu, N.; Sager, W. F.; Serafín, F. A. *J. Phys. Chem.* **1964**, 3324.

(28) Petoud, S.; Bünzli, J. C. G.; Glanzman, T.; Piguet, C.; Xiang, Q.; Thummel, R. P. *J. Lumin.* **1999**, *82* (1), 69.

(29) Ward, M. D. *Coord. Chem. Rev.* **2007**, *251* (13–14 SPEC. ISS.), 1663.

(30) Lazarides, T.; Sykes, D.; Faulkner, S.; Barbieri, A.; Ward, M. D. *Chem. - Eur. J.* **2008**, *14* (30), 9389.

(31) Werts, M. H. V; Verhoeven, J. W. *Phys. Chem. Chem. Phys.,* **2002**, *4*, 1542.

(32) Gorller-Warland, C.; Binnemans, K. *Handbook on the Physics and Chemistry of Rare Earths,* **1998**, 101.

(33) Zhou, G.; Wong, W.-Y.; Yang, X. *ChemInform*, **2011**, 42 (38).

(34) Yam, V. W.; Wong, K. M.; Wong, K. M.; Wong, K. M. *Chem. Commun.,* **2011**, *47*, 11579.

(35) Zhao, Q.; Li, F.; Huang, C. *Chem. Soc. Rev.* **2010**, *39* (8), 3007.

(36) Abu-dief, A. M.; Mohamed, I. M. A. *J. Basic Appl. Sci.* **2015**, *4* (2), 119.

(37) Xavier, A.; Srividhya, N. *J. Appl. Chem.* **2014**, *7* (11), 6.

(38) Lacelle, T.; Brunet, G.; Pialat, A.; Holmberg, R. J.; Lan, Y.; Gabidullin, B.; Korobkov, I.; Wernsdorfer, W.; Murugesu, Dalton Trans, **2017**, *46* (8), 2471.

(39) Kaim, W. *Coord. Chem. Rev.* **2002**, *230*, 127.

(40) Woods, T. J.; Ballesteros-rivas, M. F.; Ostrovsky, S. M.; Palii, A. V; Reu, O. S.; Klokishner, S. I.; Dunbar, K. R. *Chem. Eur. J.* **2015**, *2028*, 10302.

(41) Knall, A. C.; Slugovc, C. *Chem. Soc. Rev.* **2013**, *42* (12), 5131.

(42) Stetsiuk, O.; El-Ghayoury, A.; Lloret, F.; Julve, M.; Avarvari, N. *Eur. J. Inorg. Chem.* **2018**, *2018* (3), 449.

(43) Safin, D. A.; Pialat, A.; Leitch, A. A.; Tumanov, N. A.; Korobkov, I.; Filinchuk, Y.; Brusso, J. L.; Murugesu, M. *Chem. Commun.* **2015**, *51* (46), 9547.

(44) Chavez, D. E.; Hiskey, M. A. *J. Energ. Mater.* **1999**, *17* (4), 357.

(45) Samanta, S.; Das, S.; Biswas, P. *J. Org. Chem.* **2013**, *78* (22), 11184.

(46) Chavez, D. E.; Hiskey, M. A. *J. Heterocycl. Chem.* **1998**, *35* (6), 1329.

(47) Schwach, M.; Hausen, H.-D.; Kaim, W. *Inorg. Chem.* **1999**, *38* (10), 2242.

(48) Lacelle, T. Design and Synthesis of Lanthanide Single- Molecule Magnets Using the Schiff Base Approach, University of Ottawa, 2017.

(49) Shavaleev, N. M.; Pope, S. J. A.; Bell, Z. R.; Ward, M. D. *Dalton Trans.* **2003**, 808.

(50) Casanova, D.; Llunell, M.; Alemany, P.; Alvarez, S. *Chem. - Eur. J.* **2005**, *11* (5), 1479.

(51) Gao, W.; Cui, D. *J. Am. Chem. Soc.* **2008**, *130* (14), 4984.

(52) Horii, Y.; Horie, Y.; Katoh, K.; Breedlove, B. K.; Yamashita, M. *Inorg. Chem.* **2018**, *57* (2), 565.

(53) Article, E.; Chilton, N. F.; Langley, S. K.; Moubaraki, B.; Soncini, A.; Batten, S. R.; Murray, K. S. *Chem. Sci.* **2013**, *4*, 1719.

(54) Comba, P.; Daumann, L. J.; Koo, C.; Riley, M. J.; Roberts, A. E.; Wadepohl, H.; Werner, J. *Chem. Eur. J.* **2018**, *24*, 5319.

(55) Wen, H.; Liang, F.; Zou, Z.; Liu, S.; Liao, J.; Chen, J. *Inorg. Chem. Commun.* **2017**, *79*, 41.

(56) Yao, B.; Gu, B.; Su, M.; Li, G.; Ma, Y.; Li, L.; Wang, Q.; Cheng, P.; Zhang, X. *RSC Adv.,* **2017**, *7*, 2766.

(57) Brown, A. J.; Pinkowicz, D.; Saber, M. R.; Dunbar, K. R. *Angew. Chem. Int. Ed.* **2015**, *54*.

(58) Chen, L.; Zhou, J.; Yuan, A.; Song, Y. *Dalton Trans.* **2017**, *46*, 15812.

(59) Oleh Stetsiuk, Abdelkarim El-Ghayoury, Frances Lloret, M. J. and N. A. *Eur. J. Inorg. Chem.* **2018**, No. 1, 449.

(60) Benson, C. R.; Hui, A. K.; Parimal, K.; Cook, B. J.; Chen, C.-H.; Lord, R. L.; Flood, A. H.; Caulton, K. G. *Dalton Trans*. **2014**, 43 (17), 6513.

(61) Choi, A. W.; Tso, K. K.; Yim, V. M.; Liu, H.; Lo, K. K. *Chem. Commun.,* **2015**, No. 2, 3442.

(62) Beeby, A.; Dickins, R. S.; Faulkner, S.; Parker, D.; Williams, J. A. G. *Chem. Commun.,* **1997**, 2.

(63) Bauer, J.; Rademann, J. *Tetrahedron Lett.* **2003**, *44* (27), 5019.

(64) Mallakpour, S. E.; Hajipour, A.-R.; Habibi, S. *Eur. Polym. J.* **2001**, *37* (12), 2435.

(65) Faghihi, K.; Zamani, K.; Mallakpour, S. *Polym. J.* **2002**.

(66) Struijk, C. W.; Sieval, A. B.; Dakhorst, J. E. J.; Van Dijk, M.; Kimkes, P.; Koehorst, R. B. M.; Donker, H.; Schaafsma, T. J.; Picken, S. J.; Van de Craats, A. M.; Warman, J. M.; Zuilhof, H.; Sudholter, E. J. R. *J. Am. Chem. Soc.* **2000**, *122* (45), 11057.

(67) Zhou, Q. Z.; Jiang, X. K.; Shao, X. Bin; Chen, G. J.; Jia, M. X.; Li, Z. T. *Org. Lett.* **2003**, *5* (11), 1955.

(68) He, J.; Horie, K.; Yokota, R.; He, F. *Polymer.* **2001**, *42* (9), 4063.

(69) Liaw, D.-J.; Liaw, B.-Y. *Polym. J.* **1999**, *31* (12), 1270.

(70) Chiriac, C. I.; Nechifor, M.; Tanasă, F. *Rev. Roum. Chim.* **2007**, *52* (8–9), 883.

(71) Jacquemin, D.; Perpète, E. A.; Scalmani, G.; Ciofini, I.; Peltier, C.; Adamo, C. *Chem. Phys.* **2010**, *372* (1–3), 61.

(72) Cao, H.; Chang, V.; Hernandez, R.; Heagy, M. D. *J. Org. Chem.* **2005**, *70* (13), 4929.

(73) Nandhikonda, P.; Begaye, M. P.; Cao, Z.; Heagy, M. D. *Org. Biomol. Chem.* **2010**, *8* (14), 3195.

(74) Gosztola, D.; Niemczyk, M. P.; Svec, W.; Lukas, A. S.; Wasielewski, M. R. *J. Phys. Chem. A* **2000**, *104* (28), 6545.

(75) Reger, D. L.; Debreczeni, A.; Horger, J. J.; Smith, M. D. *Cryst. Growth Des.* **2011**, *11* (9), 4068.

(76) Combay, S.; Imbert, D.; Chauvin, A.-S.; Comby, S.; Bünzli, J.-C. G.; Charbonniere, L. J.; Ziesse; R. F. *Inorg. Chem.* **2004**, *43* (23), 7369.

(77) Monteiro, J. H. S. K.; Machado, D.; de Hollanda, L. M.; Lancellotti, M.; Sigoli, F. A.; de Bettencourt-Dias, A. *Chem. Commun.* **2017**, *53* (2), 11818.

(78) Zolin, V.; Puntus, L.; Kudryashova, V.; Tsaryuk, V.; Legendziewicz, J.; Gawryszewska, P.; Szostak, R. *J. Alloys Compd.* **2002**, *341* (1–2), 376.

(79) Kalinovskaya, I. V. *Opt. Spectrosc.* **2016**, *120* (6), 888.

(80) Reger, D. L.; Debreczeni, A.; Smith, M. D. *Inorg. Chim. Acta* **2010**, *364* (1), 10.

(81) Reger, D. L.; Debreczeni, A.; Reinecke, B.; Rassolov, V.; Smith, M. D.; Semeniuc, R. F. *Inorg. Chem.* **2009**, *48* (18), 8911.

(82) March, R.; Clegg, W.; Coxall, R. A.; Cucurull-Sánchez, L.; Lezama, L.; Rojo, T.; González-Duarte, P. *Inorg Chim. Acta* **2003**, *353*, 129.

(83) Vezzosi, I. M.; Zanoli, F. A.; Battaglia, L. Pietro; Corradi, A. B. *Inorg. Chim. Acta* **1985**, *105* (1), 13.

(84) Reimann, C. W. *J. Res. Natl. Bur. Stand. Phys. Chem.* **1966**, *70* (Ii), 417.

(85) Schönherr Thomas; Jørgensen Christian Klixbüll. *Optical spectra and chemical bonding in transition metal complexes: special volume II dedicated to Professor Jørgensen*; Springer: Berlin, 2004.

(86) Niehaus, T. A.; Hofbeck, T.; Yersin, H. *RSC Adv.* **2015**, *5* (78), 63318.

(87) Lee, S. K.; Zu, Y.; Herrmann, A.; Geerts, Y.; Müllen, K.; Bard, A. J. *J. Am. Chem. Soc.* **1999**, *121* (14), 3513.

(88) Wiederrecht, G. P.; Wasielewski, M. R. *J. Am. Chem. Soc.* **1998**, *120* (13), 3231.

(89) Viehbeck, A. *J. Electrochem. Soc.* **1990**, *137* (5), 1460.

(90) Barooah, N.; Tamuly, C.; Baruah, J. *J. Chem. Sci.* **2005**, *117* (2), 117.

(91) Zhou, Y.; Yao, Y.; Li, J.; Yao, C.; Lin, B. *Sensors Actuators B. Chem.* **2012**, *174*, 414.

(92) Kolanowski, J. L.; Bonnitcha, P. D.; New, E. J. *Chem. Commun.* **2017**, *53*, 3571.